P–T–X Conditions of metamorphic systems

Chiara Groppo, Department of Earth Sciences, University of Torino, Torino, Italy

This chapter has been reviewed by the section editor Matthew Kohn.

Abstract

Constraining physical and chemical information from metamorphic rocks is crucial for our understanding of the geochemical and geodynamic processes governing the Earth's evolution through time. This chapter presents an overview of the methods currently available for extracting quantitative information from metamorphic rocks, in terms of their pressure-temperature (*P–T*) evolution, changes in the fluid composition (X_{FLUID}) and dependence of the observed assemblages on the composition

of the system (X_{SYSTEM}). The review discusses two main targets: (1) constraining the *P–T* conditions experienced by metamorphic rocks, and (2) constraining the fluid production processes and how its composition evolves as a function of *P* and *T*. At the end, possible future perspectives are also mentioned.

Keywords

Equilibrium thermodynamics; Fluid evolution; Forward and inverse thermodynamic modeling; Metamorphic petrology; Phase diagrams; Pressure-temperature-composition (*P–T–X*) variables; Thermobarometry

Key points

- Defining the *P–T–X* framework of metamorphism.
- Summarizing the basic principles of inverse and forward thermodynamic modeling.
- Presenting the methods for constraining the *P–T* evolution of metamorphic rocks, with emphasis on their strengths and weaknesses.
- Discussing the strategies for constraining the fluid evolution in metamorphic systems.
- Perspectives.

Introduction

Metamorphic rocks now exposed on the Earth's surface are archives of information about the petrologic and geodynamic processes through which they formed. These processes occurred at variable depths, thermal states, and times through the Earth's history, shaping our Planet from inside as we know it today; the same, or similar, processes still occur nowadays, influencing how the Earth will look like in the future. Our understanding of the Earth's evolution is therefore directly linked to our capacity of interpreting the metamorphic rocks' archives and of quantitatively constraining the main variables that control metamorphic processes in the Earth's crust.

Retrieving physical and chemical information from metamorphic rocks has long been the main target of metamorphic petrology, but the approaches to achieve this goal have changed over the past 50 years, leading to what has been recently called as the "metamorphosis of metamorphic petrology" (Spear et al., 2016). The theoretical basis of these approaches (i.e., principles of equilibrium thermodynamics) are discussed in detail in numerous fundamental volumes (e.g., Spear, 1993; Will, 1998; Wood and Fraser, 1976) and textbooks (e.g., Bucher and Grapes, 2011; Winter, 2010), and are only briefly summarized here. Moreover, several recent reviews have already excellently discussed the strategies commonly used to constrain the physical and chemical conditions recorded by crustal rocks. These review papers variably highlight the progressive improvement of the methods from an historical perspective (e.g., Spear et al., 2016), compare the various strategies and discuss their respective advantages and pitfalls (e.g., Lanari and Duesterhoeft, 2019; Waters, 2019), or focus on a single, specific, approach with examples of petrological applications (e.g., Evans et al., 2013; Powell and Holland, 2008, 2010; Yakymchuk, 2017).

This chapter presents an overview of the methods currently available for extracting quantitative information from metamorphic rocks, in terms of their pressure-temperature (*P–T*) evolution (i.e., thermobarometry), changes in the fluid composition (X_{FLUID}) and dependence of the observed assemblages on the composition of the system (X_{SYSTEM}). The review intends providing a practical guide of which strategy is best to use as a function of the target we would like to achieve. Two main targets are specifically discussed:

(1) constraining the *P–T* conditions experienced by metamorphic rocks: this is the most common application of the majority of thermobarometric methods. All the recent review papers mentioned above discuss this petrologic application from their own perspective; also the first part of this chapter illustrates the different thermobarometric strategies currently available for reconstructing the *P–T* evolution of metamorphic rocks, highlighting their strengths and weaknesses.
(2) constraining the fluid evolution: although fluids play a fundamental role in most metamorphic processes, in many cases they can be approximated to pure H_2O, and fluid saturated conditions can be reasonably assumed, at least during heating. However, the first assumption is not applicable in case of mixed-volatile fluids (e.g., —— COH fluids), and the fluid saturation constrain is not always defensible, especially during cooling (e.g., Connolly and Trommsdorff, 1991; Thompson, 1983). Most of the recent review papers only marginally discuss the strategies for quantitatively constraining mixed-volatile fluid evolution during metamorphism and for understanding the link between *P–T* changes, fluid production, and the resulting assemblages and microstructures in the source rocks. The second part of this review is therefore dedicated to this task.

It is assumed that the reader is moderately familiar with thermobarometry and phase equilibrium modeling, although the basic principles of both approaches are briefly summarized in sections "Basic principles of inverse thermodynamic modeling" and "Basic principles of forward thermodynamic modeling". Software currently available for forward thermodynamic modeling is not explicitly discussed; all the phase diagrams used in this chapter have been calculated using PerpleX (Connolly, 1990, 2005, 2009; Connolly and Kerrick, 1987), but comparable results can be obtained using Thermocalc (Powell and Holland, 1988, 2008; Powell et al., 1998), Theriak-Domino (de Capitani and Brown, 1987; de Capitani and Petrakakis, 2010), GIBBS (Spear et al., 1982; Spear

and Menard, 1989), GeoPS (Xiang and Connolly, 2021) or MAGEMin (Riel et al., 2022), provided that the same dataset and activity-composition models are used. Mineral abbreviations are after Warr, 2021 (with Phg = phengite).

The pressure-temperature-compositional (*P–T–X*) framework of metamorphism

The equilibrium paradigm

The mineral facies concept introduced by Eskola one century ago (Eskola, 1915) inherently implies that peak assemblages in metamorphic rocks reflect thermodynamic equilibrium (i.e., thermal, physical and chemical equilibrium). The concept of equilibrium thermodynamics is therefore commonly used for describing, understanding and predicting most metamorphic processes, and provides the basis for quantifying the physical conditions of metamorphism. Petrographic evidence supports the general idea that during prograde metamorphism (i.e., at increasing temperature), mineral assemblages and compositions continuously evolve along a *P–T* path in a way that maintains a state of minimum total Gibbs free energy, which represents the stable equilibrium condition. The ability of a rock to adjust its mineralogy (i.e., to re-equilibrate) in response to the variation of temperature and pressure depends on: (i) whether the driving forces are sufficient to overcome the kinetic barriers to nucleation and growth, and (ii) whether energy and material are transferred efficiently within (and outside) the system. Whenever some kinetic and/or rate-limiting process impedes the overcoming of the kinetic barriers or the efficient transfer of material and energy, the system fails to reach a stable equilibrium state and remains metastable. Defining whether or not a metamorphic rock has reached the equilibrium state is not always straightforward (e.g., Lanari and Hermann, 2021), and increasing evidence at diverse scales and geodynamic settings suggest that the departure from the equilibrium behavior can be potentially relevant (e.g., Carlson, 2002; Carlson et al., 2015; Foster, 1986, 1999; Pattison and Spear, 2018; Pattison and Tinkham, 2009; Spear et al., 1990, 2014; Spear and Pattison, 2017; Waters and Lovegrove, 2002; Wolfe and Spear, 2018).

Notwithstanding the possible relevant role of sluggish kinetic or diffusional processes, the equilibrium paradigm still provides the indispensable framework for the study of metamorphic systems (Carlson et al., 2015); within this paradigm, it can be assumed that equilibrium is achievable at some scale within the so called "equilibration volume", i.e., the scale on which chemical equilibration among coexisting phases can be reasonably assumed (Lanari and Engi, 2017; Powell and Holland, 2008). For the purpose of this review, the "local equilibrium" view of metamorphism (Thompson Jr., 1959) is therefore applied, which assumes that the nucleation and diffusion rates—at least for some elements over some scale—are faster than the rate of *P–T* variation (i.e., kinetic and diffusion limiting factors are negligible). Ideally, it can be argued that: (i) the phase assemblages ultimately preserved in metamorphic rocks reflect a single state of frozen-in equilibrium recorded at a specific point along the *P–T* path; (ii) as far as fluid (or melt) is present in the system, mineral assemblages converge continuously toward equilibrium as *P* and *T* change; (iii) because fluid– (and melt–) producing reactions mostly occur during prograde metamorphism, the preserved mineral assemblages in metamorphic rocks generally reflect the assemblages formed at the maximum temperature reached along the *P–T* path (i.e., at the metamorphic peak); (iv) little or no change occurs once that fluid (or melt) is completely lost (i.e., during retrograde evolution), unless fluid is introduced from outside (e.g., Guiraud et al., 2001; Powell et al., 2005; Powell and Holland, 2008, 2010; White and Powell, 2002). Indeed, metamorphic rocks often deviate from this ideal behavior, preserving either prograde information (e.g., metastable inclusions which did not re-equilibrate because they were isolated from the reacting matrix; prograde mineral zoning) or retrograde ones (e.g., retrograde minerals replacing peak phases; diffusion zoning), and thus provide information about multiple frozen-in equilibrium states recorded at different points along the *P–T* path (Spear, 1989; Spear et al., 1984; Thompson, 1984).

A good petrographic analysis is the fundamental premise of any petrologic study aimed at reconstructing the *P–T–X* evolution of metamorphic rocks (e.g., Robinson, 1991). Careful microstructural observations, mineral composition analyzes, characterization of compositional zoning, and the possible study of fluid/melt inclusions, all contribute to: (i) recognize different metamorphic stages preserved in a single rock, (ii) select mineral compositions to be combined for thermobarometric purposes (see section "Constraining the P–T conditions experienced by metamorphic rocks"), and (iii) interpret metamorphic processes (e.g., devolatilization reactions, see section "How to constrain fluid evolution"). Basically, we can say that the microstructures alone already tell us the whole story hidden in metamorphic rocks; the methods discussed in this review give a quantitative dimension to this story.

The *P–T–X* variables

In the framework of the equilibrium paradigm, what we ultimately observe in metamorphic rocks (i.e., phase assemblages, amounts and compositions) is controlled by different thermodynamic variables that can be either intensive or extensive. Intensive variables have the same value in all phases that are in equilibrium with each other, and are independent of the amount of material (i.e., the number of moles) involved. Pressure (P), temperature (T) and the chemical potential of a phase i (μ_i) are the most important intensive variables in metamorphic systems. In contrast, extensive variables depend on the amount of material present in the system and do not have the same value in all the phases coexisting at equilibrium. Examples of extensive variables are volume (V), entropy (S), enthalpy (H), Gibbs energy (G) and composition of the system (i.e., number of moles n_i of a phase i). Extensive variables can be normalized by dividing them by the number of moles in the system, Σn_j (e.g., mole fraction $X_i = n_i/\Sigma n_j$). Normalized extensive variables are independent of the amount of material, but they still have different values in different parts of an equilibrium system (unlike μ, P, and T, which are constant throughout); in the literature, they have sometimes been described as intensive (e.g., Will, 1998) but are more logically extensive (e.g., Evans et al., 2013; Powell et al., 2005).

Three of these thermodynamic variables, i.e., pressure P, temperature T and composition X, are especially useful for describing and interpreting metamorphic processes, and for linking these processes to the geodynamic ones. This review deals with the

quantitative determination of these three variables only, with the assumption that most extensive variables (e.g., *V*, *H*, *S*) normally change to accommodate the variations in *P* and *T* (although this is not always the case; Powell et al., 2005). An elegant discussion on how *P*, *T* and *X* are related to the other intensive and extensive thermodynamic variables is reported in Powell et al. (2005) (see also: Evans et al., 2013; Spear, 1988).

For the purposes of this review, the compositional variable, *X*, is alternatively referred to:

(a) the system composition (X_{SYSTEM}), expressed in terms of the chemical components (generally oxides) necessary to describe all the phases of the system, including the fluid phase. The composition of the system can be completely unconstrained (e.g., in *P–T* projections), totally fixed (e.g., in isochemical phase diagrams), or it can vary in a specified compositional range (e.g., in compositional phase diagrams).
(b) the fluid composition (X_{FLUID}), expressed in terms of a composition vector that describes the variation in the amount of a specific component within the fluid phase, e.g., the molar fraction of CO_2, $X(CO_2) = CO_2/(CO_2 + H_2O)$.

Inverse vs. forward modeling strategies

Two main modeling approaches can be used to constrain the equilibrium *P–T* conditions recorded by metamorphic rocks, both relying on the principles of equilibrium thermodynamics: inverse and forward modeling. The term inverse vs. forward is related to the way in which each strategy links the causes (i.e., changes in *P–T* conditions and the bulk composition of the system) to the effects (i.e., the observed assemblages and the measured mineral modes and compositions).

Inverse thermodynamic modeling starts from the results to understand the causes of those results; in other words, it uses the mineral assemblages, modes, and compositions measured in a natural sample (which are assumed to reflect equilibrium) to retrieve the *P–T* conditions at which these minerals equilibrated. Conventional, single phase and multi-equilibrium thermobarometric methods all belong to the inverse thermodynamic modeling group. On the opposite, forward thermodynamic modeling starts from the causes to predict the results, and then compares the modeled results with the observed/measured ones. This second strategy applies Gibbs free energy minimization principles to predict stable assemblages, modes and compositions in a range of equilibrium conditions (*P*, *T*, X_{FLUID}, etc.); the comparison between the modeled results and the natural observations constrains the equilibrium conditions effectively experienced by the natural sample. Forward modeling strategies essentially include the calculation of different types of phase diagrams.

Basic principles of inverse thermodynamic modeling

Inverse modeling methods are based on the observation that element fractionation within solid solution phases systematically varies with changing temperature and/or pressure during metamorphism. Inverse thermobarometric methods thus solve a number of balanced reactions, specifically calibrated from phase equilibrium experiments, which describe element fractionation between coexisting minerals as a function of temperature (i.e., thermometer) or pressure (i.e., barometer). The fundamental equation that defines the equilibrium conditions for each of these reactions is:

$$0 = \Delta G_{P,T} = \Delta G^{\circ}_{P,T} + RT \ln K \quad (1)$$

In which:

- $\Delta G_{P,T}$ is the Gibbs free energy of the reaction between the mineral solutions (i.e., phases of variable composition) at the equilibrium *P* and *T* (J mol^{-1});
- $\Delta G^{\circ}_{P,T}$ is the Gibbs free energy of the reaction between the pure end-members (i.e., phases of fixed composition) at the equilibrium *P* and *T* (J mol^{-1});
- R is the universal gas constant (J mol^{-1} K^{-1})
- *T* is the temperature (K)
- *K* is the equilibrium constant of the reaction.

For a rigorous discussion of how to derive each term of Eq. (1), the reader could refer to a large number of textbooks, volumes and review papers (e.g., Anderson, 2005; Powell, 1978; Spear, 1993; Will, 1998; Wood and Fraser, 1976). Here, it is useful to remember that Eq. (1) consists of two terms: (i) a composition-independent term (ΔG°), which gives the Gibbs free energy difference of the reaction between pure-end members, i.e., the difference between the Gibbs free energy of the end-member products and that of the end-member reactants, each one multiplied for the correspondent stoichiometric coefficient, according to the relation $\Delta G^{\circ}_{P,T} = \sum_{i}^{n} \nu_i (\Delta_a G_i)_{P,T}$, in which ν_i is the stoichiometric coefficient for the end-member component i, and $(\Delta_a G_i)_{P,T}$ is the apparent Gibbs free energy of formation of any end-member component at *P* and *T*; (ii) a composition-dependent term ($RT\ln K$), which describes the difference between equilibrium for a reaction involving pure end-member components and the equilibrium for the same reaction involving mineral solutions.

The composition-independent term ΔG° can be, in turn, defined as the sum of different contributions, each one describing how the fundamental thermodynamic properties (i.e., enthalpy ΔH, entropy ΔS and volume ΔV) of the reaction between end-members change as a function of *P* and *T* (Berman et al., 1986). Specifically:

$$\Delta G^{\circ}_{P,T} = \Delta(\Delta_f H_{P0,T0}) + \int_{T0}^{T} \Delta C_P dT - T\left[\Delta S_{P0,T0} + \int_{T0}^{T} \frac{\Delta C_p}{T} dT\right] + \int_{P0}^{P} \Delta V_T dP \quad (2)$$

in which:

- $\Delta(\Delta_f H_{P0,T0})$ and $\Delta S_{P0,T0}$ are the enthalpy and the entropy of the reaction at the reference state $P0,T0$ (1 bar, 298.15 K), i.e., the difference between enthalpy and entropy of the products and those of the reactants at $P0,T0$;
- ΔC_p and ΔV_T are the heat capacity and volume of the reaction, respectively at the pressure and temperature of interest, i.e., the difference between the heat capacity and the volume of the products and those of the reactants.

The first two terms of Eq. (2) represent the enthalpy contribution to $\Delta G^{\circ}_{P,T}$, expressed as the enthalpy of the reaction at the reference state $P0,T0$, plus a term describing the variation of enthalpy as a function of T at constant P (i.e., $C_p = (\partial H/\partial T)_P$), between the reference temperature $T0$ and the equilibrium temperature T. The third term of Eq. (2) represents the entropy contribution to $\Delta G^{\circ}_{P,T}$, expressed as the entropy of the reaction at the reference state $P0,T0$, plus a term describing the variation of entropy as a function of T at constant P (i.e., $C_p/T = (\partial S/\partial T)_P$), between the reference temperature $T0$ and the equilibrium temperature T. And the fourth term of Eq. (2) represents the volume contribution to $\Delta G^{\circ}_{P,T}$, i.e., the variation of volume as a function of P at constant T, between the reference pressure $P0$ and the equilibrium pressure P.

The composition-dependent term $RT\ln K$ is a function of the composition of the solution phases, being the equilibrium constant K defined as:

$$K = \prod_{i}^{n} \left(a_i^{\alpha}\right)^{\nu_i} \quad (3)$$

with a_i^{α} the activity of the component i in a solution phase α, and ν_i the stoichiometric coefficient of phase α, with ν_i positive if α is a product and negative if α is a reactant. The a_i^{α} reflects the difference between the chemical potential of i in α at the P–T conditions of interest (μ_i^{α}) and the chemical potential of the same component i in the standard state (μ_i^{o}):

$$RT \ln a_i^{\alpha} = \mu_i^{\alpha} - \mu_i^{o} \quad (4)$$

An activity of 1 thus means that the component i is pure (i.e., no solution), whereas an activity of 0 implies that the component i is not present in the solution phase α. The a_i^{α} is directly related to the composition of the solution phase (i.e., to the molar fraction of the component i in the phase α, X_i^{α}), although the definition of the activity-composition (a-X) relationships is not straightforward, except for ideal mixing. The general equation that describes the a-X relationships for a solution α is:

$$a_i^{\alpha} = \left(\gamma_i X_i^{\alpha}\right)^{y} \quad (5)$$

with γ_i the activity coefficient and y the number of site multiplicity over which the mixing takes place. γ_i may vary with X and is equal to 1 in ideal solutions. This expression assumes that mixing occurs on a single site. Mixing on multiple sites requires more complicated expressions.

The equilibrium constant K in Eq. (1) is a function only of temperature and pressure (because $\Delta G^{\circ}_{P,T}$ represents the Gibbs free energy change at a specific P and T of interest). Therefore, for a given system at a given T and P, K is a constant. All the inverse thermodynamic methods use the measured compositions of minerals supposed to be in equilibrium to calculate the equilibrium constant K (Eqs. 3–5), and apply empirically or experimentally calibrated equations that correlate K to T and/or P to retrieve the equilibrium temperature and/or pressure conditions at which the minerals were formed. Suitable thermometers are equilibria that do depend weakly on pressure and therefore have a steep slope in the PT space; in contrast, equilibria characterized by a shallow slope on a PT diagram are potentially good barometers, because they are almost independent of temperature (Fig. 1). Because the slope of a reaction on a PT diagram is given by the Clausius-Clapeyron equation:

$$\frac{dP}{dT} = \frac{\Delta S}{\Delta V} \quad (6)$$

in which ΔS and ΔV are the entropy and volume changes associated to the reaction (i.e., the difference between the entropy and the volume of the products and those of the reactants), a good thermometer is characterized by a large entropy change ΔS and a small volume change ΔV, whereas a good barometer is one with a large volume change ΔV (Fig. 1). Most thermobarometric equilibria are fluid-independent because it is not always possible to determine the composition of a fluid or its pressure, which limits computational accuracy.

Basic principles of forward thermodynamic modeling

Forward modeling methods are based on the calculation of different types of phase diagrams to predict the relative amount and composition of every phase in a system, as a function of different thermodynamic variables. The fundamentals of phase equilibria are discussed in several textbooks (e.g., Spear, 1993; Vernon and Clarke, 2008; Will, 1998) and contributions (e.g., Powell et al., 1998, 2005; Powell and Holland, 2008) and are only briefly summarized here. The basic concept is that the stable assemblage at fixed P–T–X_{SYSTEM} is the mineral assemblage, modes and compositions for which the total Gibbs free energy of the system is

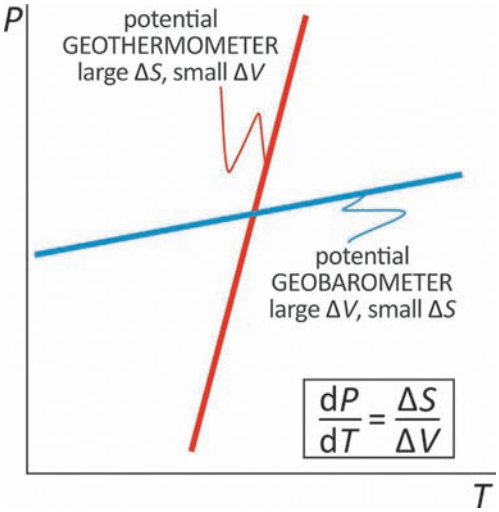

Fig. 1 Sketch of ideal geothermometers and geobarometers in the *PT* space. The slope of the reaction curves is defined by the Clausius-Clapeyron equation reported in the inset.

minimal. Phase diagrams are graphical representations of such a condition, independent of the strategy used for their calculation (i.e., phase equilibrium calculators vs. Gibbs free energy minimizers; see Lanari and Duesterhoeft, 2019 for further details).

Constructing phase diagrams requires understanding of the Gibbs phase rule, which is expressed through the relationship:

$$F = C - \Phi + 2$$

F is the variance (or degrees of freedom) of the system, Φ is the number of coexisting phases (i.e., minerals, fluids, melt) and C is the minimum number of system components required to define the composition of all the phases within the system (generally defined in terms of oxides). The Gibbs phase rule tells us the number of thermodynamic variables that can be independently changed without altering the state of a system. For a n component system, there are n + 1 independent variables, either intensive or extensive, i.e., pressure (P), temperature (T) and n–1 compositional (X) variables. A phase diagram containing all the information of such a system is called total phase diagram and has n + 1 axes; therefore, with the exception of very simple systems characterized by $n \leq 2$, the total phase diagram cannot be easily drawn. Different strategies can be adopted for representing the information of the total phase diagram in two dimensions. Each strategy inevitably involves the loss of some information: the art of phase diagramming resides in choosing the most appropriate diagram(s) for the purpose we have in mind. Three main strategies are commonly adopted to reduce the dimensions of the total phase diagram: projections, sections and isochemical phase diagrams (i.e., mineral assemblage diagrams or "pseudosections") (Powell et al., 1998; Will, 1998).

Projections

In projections, the information of the total phase diagram is projected onto a specified plane (i.e., a two-dimensional diagram). If the *P–T* plane is chosen, the resulting diagram is a *P–T* projection (also known as petrogenetic grid). This type of diagram is dominated by univariant reaction lines and invariant points, these last resulting from the intersection of several univariant reactions (Fig. 2). Projections still contain all the information of the total phase diagram, but not all this information is equally evident. Specifically, in *P–T* projections, the composition of the solution phases changes along univariant equilibria, but this information is not directly visible in the phase diagram (Fig. 2).

Sections

In sections, the two-dimensional diagram corresponds to a "cut" of the total phase diagram with respect to the intensive variables. Opposite to projections, sections are always drawn at constant values of the intensive variables not represented; *T–X* sections are drawn at constant pressure (Fig. 3) and *P–X* sections are drawn at constant temperature. These diagrams consist of fields bounded by lines (Fig. 3): each field represents a stable phase assemblage, whereas the lines are phase-in or phase-out boundaries, i.e., they mark the appearance or disappearance of a phase. In this case, the "lost" information of the total phase diagram is how the properties of the system change as a function of pressure or temperature, respectively; however, *T–X* and *P–X* sections show how the composition of the solution phases changes along univariant equilibria, and are therefore useful for documenting changes in mineral compositions as a function of *P* or *T*. Such diagrams are also common for investigating the effects of mixed fluid compositions on mineral assemblage stabilities.

Compatibility diagrams (or chemographic diagrams) are a special type of section obtained by "cutting" the total phase diagram with respect to both *T* and *P*, i.e., they are isothermal-isobaric sections. Chemographic diagrams are useful to document which phase assemblage is stable for any given bulk composition in the system, and which are the compositions of the coexisting phases, at the specified *P–T* conditions (Fig. 4). However, in order to understand how phase assemblages and compositions evolve as a function of *P* and *T*, several chemographic diagrams must be used, each one drawn at different *P–T* conditions.

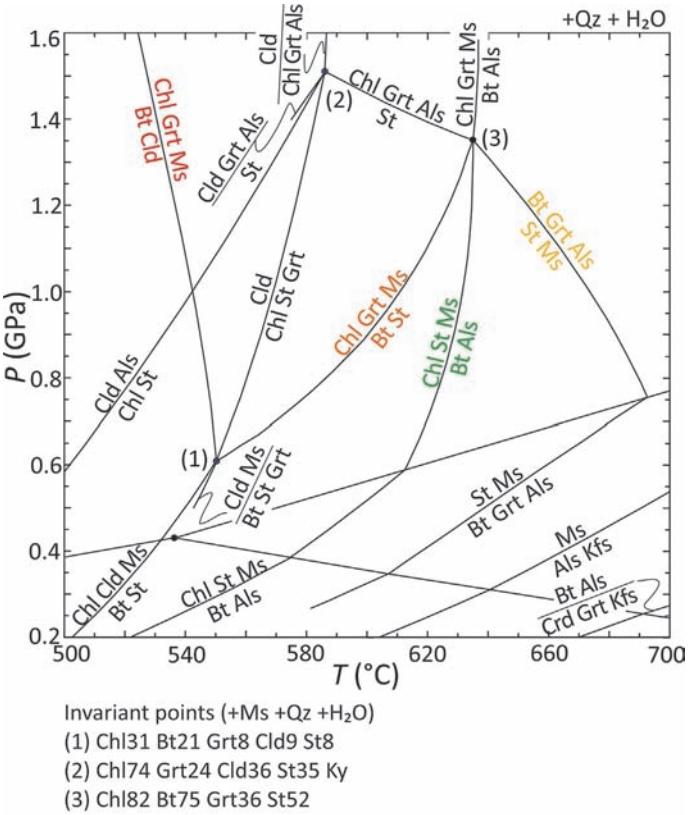

Fig. 2 *P–T* projection in the KFMASH system for a generic metapelite. The petrogenetic grid is calculated using Perple_X (version 6.9.1; Connolly, 1990, 2005, 2009), the Holland and Powell (2011) database (ds62) and the solution models of White et al. (2014a), and it reproduces part of Fig. 1a in White et al. (2014b). The composition of phases at invariant points are reported below the phase diagram (*X*Mg%) and help understanding how the compositions of solution phases change along univariant equilibria (e.g., chlorite, chloritoid and garnet all evolve toward Mg-richer compositions moving from point (1) to point (2)); this information is otherwise not directly evident from the diagram. Colored univariant reactions refer to the same equilibria reported in the *T–X*Mg section of Fig. 3.

Isochemical phase diagrams

Isochemical phase diagrams (i.e., mineral assemblage diagrams, MAD) are phase diagrams drawn for a fixed bulk composition of the system. *P–T* isochemical phase diagrams are by far the most used type of MADs; they contain information about how mineral assemblages, abundances and compositions change with variations of the intensive variables *P* and *T*, for the specified bulk composition. However, any other combinations of variables, either intensive or extensive, can be used, as discussed in detail by Powell et al. (2005).

Similarly to sections, isochemical phase diagrams consist of fields bounded by lines (Fig. 5a), these last representing phase-in or phase-out boundaries. Mineral modes and compositions change continuously as a function of *P* and *T* across each field; as a consequence, these diagrams can be contoured with isopleths of mode and composition (Fig. 5b), that represent lines along which mineral proportions and compositions are constant, respectively. Fixing the bulk composition of the system, isochemical phase diagrams show only those equilibria that are relevant to that specific composition; therefore, these diagrams are useful to constrain the metamorphic evolution of a specific rock, but the obtained results cannot be applied to rocks of different compositions, even if they belong to the same chemical system (e.g., pelitic, mafic, etc.).

Constraining the *P–T* conditions experienced by metamorphic rocks

Conventional thermobarometry

Thermobarometry is the discipline that quantitatively links the *P–T* conditions experienced by a metamorphic rock assuming chemical equilibrium was achieved, with the observed/measured mineral assemblages and compositions. Application of thermobarometry to natural metamorphic systems ultimately allows understanding of tectonic and metamorphic processes in different geodynamic contexts.

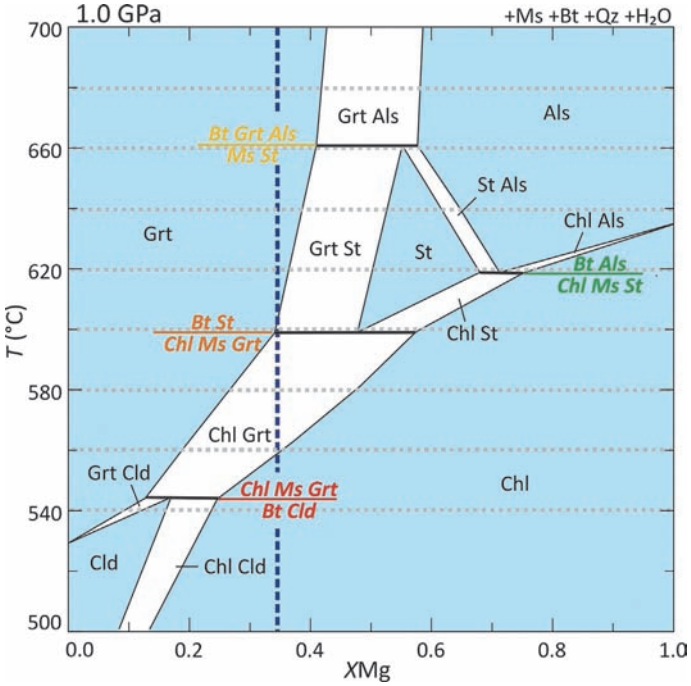

Fig. 3 Isobaric *T*–*X*Mg section in the KFMASH system, calculated at 1.0 GPa using the bulk composition (mol%): SiO_2 68.76, Al_2O_3 9.87, K_2O 3.16, MgO from 0.00 to 11.65, FeO from 11.65 to 0.00 (same bulk composition used by White et al., 2014a for their Fig. 4). The phase diagram is calculated using Perple_X (version 6.9.1; Connolly, 1990, 2005, 2009), the Holland and Powell (2011) database (ds62) and the solution models of White et al. (2014b) . Thick black lines with colored labels correspond to the univariant equilibria reported with the same colors in Fig. 2. White and light blue fields are di- and tri-variant fields, respectively. The grey dotted lines define the temperatures at which the AFM chemographic diagrams of Fig. 4 are calculated; the dashed blue line defines the *X*Mg of the *P*–*T* isochemical phase diagram reported in Fig. 5.

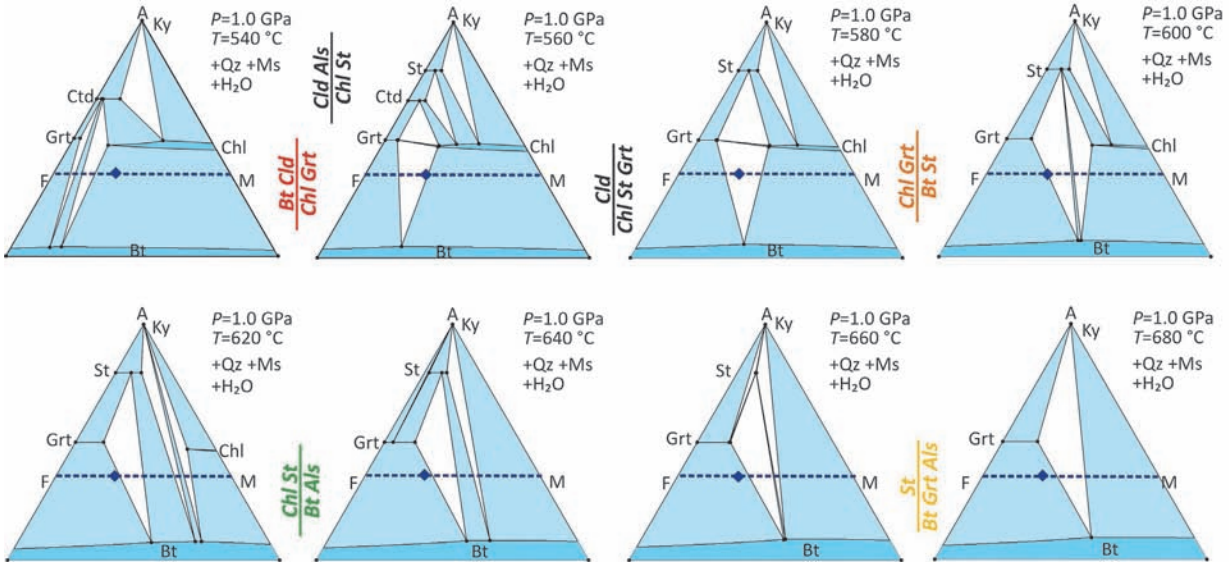

Fig. 4 AFM chemographic diagrams calculated at different *P*–*T* conditions (quartz, muscovite, H_2O in excess) using Perple_X (version 6.9.1; Connolly, 1990, 2005, 2009), the Holland and Powell (2011) database (ds62) and the solution models of White et al. (2014a). Variance of the fields varies from 2 (white) to 4 (dark blue). The blue dashed lines define the A value ($A = Al_2O_3 – 3K_2O$) of the *T*–*X*Mg section of Fig. 3, and the blue diamond corresponds to the bulk composition used for the *P*–*T* isochemical phase diagram of Fig. 5. Univariant reactions are reported in italic; colors are the same as in Figs. 2 and 3.

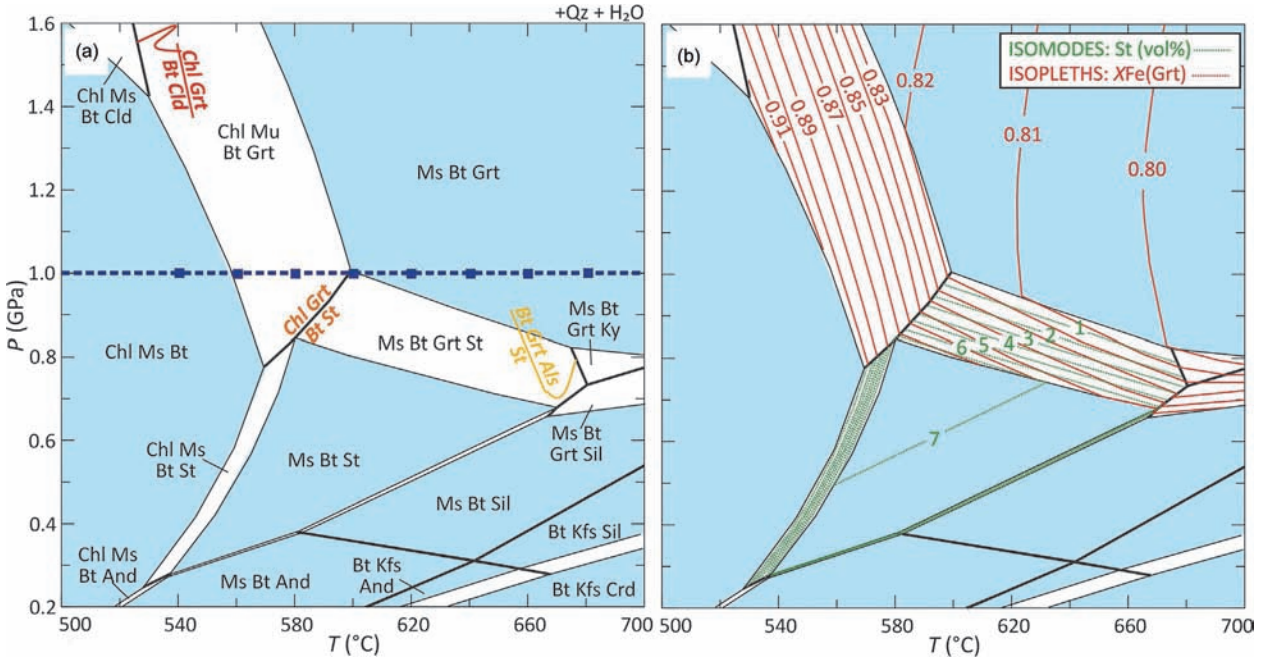

Fig. 5 (a) *P–T* isochemical phase diagram in the KFMASH system (quartz and H_2O in excess), calculated using the bulk composition (mol%): SiO_2 68.76, Al_2O_3 9.87, K_2O 3.16, MgO 4.01, FeO 7.64 (same bulk composition used by White et al., 2014a for their Fig. 4). The phase diagram is calculated using Perple_X (version 6.9.1; Connolly, 1990, 2005, 2009), the Holland and Powell (2011) database (ds62) and the solution models of White et al. (2014a, 2014b). Thick black lines are univariant equilibria (same colors as in Fig. 2). White and light blue fields are di- and tri-variant fields, respectively. The blue dashed line and the blue squares define the *P* and the *P–T* conditions at which the *T–X*Mg section and the AFM chemographic diagrams of Figs. 3 and 4 are calculated, respectively. Note that, compared to the *P–T* projection of Fig. 2, this phase diagram only shows the univariant reactions that are "seen" by this specific bulk composition. (b) Same phase diagram as (a), contoured with staurolite isomodes and garnet compositional isopleths (*X*Fe).

Thermometers based on cation exchange reactions

Cation exchange reactions involve the exchange of cations between coexisting solution phases. Because the exchanged cations commonly have similar size and the same charge, no major change in volume (ΔV) is involved in the exchange and therefore, according to Eq. (6), this type of reactions is very sensitive to temperature but poorly dependent on pressure (Fig. 6). The most widely applied conventional thermometers are cation exchange reactions involving Fe^{2+}-Mg substitution within a pair of Fe-Mg solid solutions. In principle, all Fe-Mg -bearing minerals can be used to this purpose, according to the general reaction:

$$\mathrm{aFe}\alpha^{y} + \mathrm{bMg}\beta^{z} = \mathrm{aMg}\alpha^{y} + \mathrm{bFe}\beta^{z}$$

where Mgα, Feα are the Mg and Fe^{2+} end-members of a solid solution α (e.g., forsterite Mg_2SiO_4 and fayalite Fe_2SiO_4 end-members within the olivine solution), and Mgβ, Feβ are the Mg and Fe^{2+} end-members of the solid solution β (e.g., pyrope $Mg_3Al_2Si_3O_{12}$ and almandine $Fe_3Al_2Si_3O_{12}$ end-members within the garnet solution), a and b are the stoichiometric coefficients of the balanced reaction (e.g., 3Fa + 2Prp = 3Fo + 2Alm), and y and z are the number of sites (the site multiplicity) over which the mixing takes place in the solutions α and β, respectively (e.g., y = 2 for olivine; z = 3 for garnet). According to Eq. (3), the equilibrium constant for this reaction is defined as:

$$\mathrm{K} = \frac{\left(a^{\alpha}_{\mathrm{Mg}\alpha}\right)^{\mathrm{a}} \cdot \left(a^{\beta}_{\mathrm{Fe}\beta}\right)^{\mathrm{b}}}{\left(a^{\alpha}_{\mathrm{Fe}\alpha}\right)^{\mathrm{a}} \cdot \left(a^{\beta}_{\mathrm{Mg}\beta}\right)^{\mathrm{b}}}$$

Because mixing of $Fe^{2+}$and Mg generally occurs on a single site in both α and β solid solutions, the activities of each end-member are defined by Eq. (5) as $a^{\alpha}_{\mathrm{Mg}\alpha} = (\gamma_{\alpha} X^{\alpha}_{\mathrm{Mg}})^{y}$ and $a^{\alpha}_{\mathrm{Fe}\alpha} = (\gamma_{\alpha} X^{\alpha}_{\mathrm{Fe}})^{y}$ for the solid solution α, and $a^{\beta}_{\mathrm{Mg}\beta} = (\gamma_{\beta} X^{\beta}_{\mathrm{Mg}})^{z}$ and $a^{\beta}_{\mathrm{Fe}\beta} = (\gamma_{\beta} X^{\beta}_{\mathrm{Fe}})^{z}$ for the solid solution β. Assuming an ideal behavior of Fe and Mg along the Fe-Mg join (i.e., γ_{α}=1 and γ_{β}=1) the equation becomes:

$$K = \frac{\left[\left(X^{\alpha}_{\mathrm{Mg}}\right)^{y}\right]^{a} \cdot \left[\left(X^{\beta}_{\mathrm{Fe}}\right)^{z}\right]^{b}}{\left[\left(X^{\alpha}_{\mathrm{Fe}}\right)^{y}\right]^{a} \cdot \left[\left(X^{\beta}_{\mathrm{Mg}}\right)^{z}\right]^{b}} \quad \text{and}$$

$$K_{\mathrm{D}} = \frac{\left(X_{\mathrm{Mg}}/X_{\mathrm{Fe}}\right)^{\alpha}}{\left(X_{\mathrm{Mg}}/X_{\mathrm{Fe}}\right)^{\beta}} = \frac{(\mathrm{Mg/Fe})^{\alpha}}{(\mathrm{Mg/Fe})^{\beta}}$$

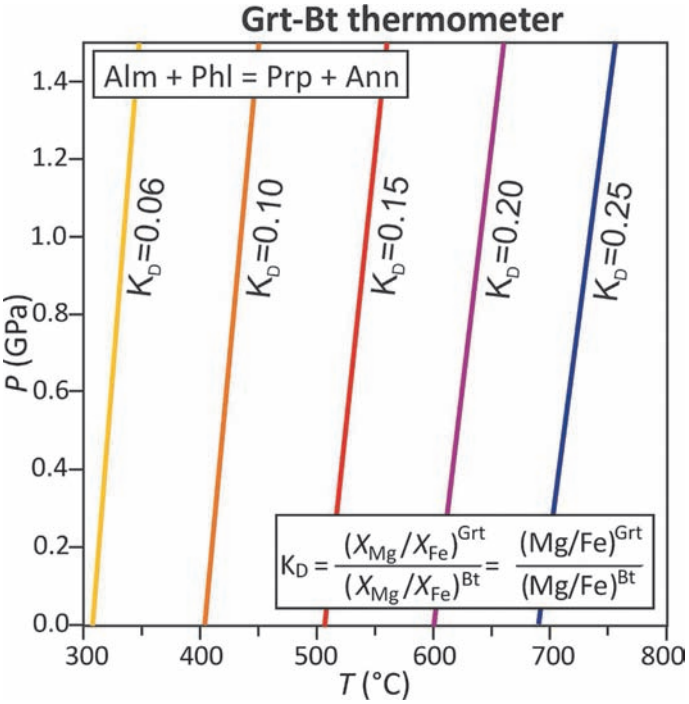

Fig. 6 Lines of constant K_D for the garnet-biotite thermometer plotted in the *PT* space using the equation of Ferry and Spear (1978). This geothermometer is based on the Fe-Mg exchange reaction Alm + Phl = Prp + Ann. Assuming an ideal behavior for both garnet and biotite solutions (i.e., $a_i = X_i$), the K_D of the reaction is defined according to the equation reported in the inset. The common occurrence of the garnet + biotite assemblage in metamorphic rocks makes this thermometer widely applicable on rocks of various compositions and explains its popularity (e.g., Caddick and Thompson, 2008).

with K_D defined as distribution coefficient between the two solution phases (e.g., Thompson, 1984), which is related to the equilibrium constant K by a constant exponent equal to a·y (= b·z).

Lists of the most common Fe-Mg exchange thermometers, with the relevant references, can be found in the majority of textbooks (e.g., Spear, 1993; Bucher and Grapes, 2011; Winter, 2010). Examples of mineral pairs commonly used as exchange thermometers include: olivine-orthopyroxene, olivine-spinel, olivine-garnet, orthopyroxene-clinopyroxene, garnet-orthopyroxene, garnet-clinopyroxene, garnet-hornblende that can be applied on ultramafic and mafic rocks, and garnet-biotite, garnet-chlorite, garnet-cordierite, cordierite-spinel, orthopyroxene-biotite, garnet-phengite that can be applied to pelitic rocks. For most of these pairs, several calibrations are available, mostly derived from experimental works or from thermodynamic calculations. Corrections for the effects of additional components other than Fe^{2+} and Mg in the solid solutions (e.g., Ca in garnet, Al and Ti in biotite, Na and Al in clinopyroxene, Al in orthopyroxene, etc.) are considered in some calibrations as well, but care should be taken in applying Fe-Mg exchange thermometers on minerals whose composition is far from a simple Fe-Mg solution (i.e., effect of other components, as discussed in Bucher and Grapes, 2011).

Thermometers based on isotopic exchange

Similar to cation exchange thermometry, isotopic exchange thermometry involves the exchange of isotopes of the same elements between a mineral pair. Depending on mineral structure and bond strength, the fractionation of light stable isotopes (typically of the elements C, O and S) between two coexisting minerals can depend strongly on temperature, with large isotopic disparities at low temperature, progressively decreasing toward zero at high temperatures (Chacko et al., 2001; Valley, 1986, 2001; Vho et al., 2019) (Fig. 7). The greater the difference in the composition and crystal structure between the two coexisting phases, the higher the isotopic fractionation; therefore, mineral pairs most commonly used are those involving silicate-carbonate (e.g., quartz-calcite at low temperature), orthosilicate-tectosilicate (e.g., quartz-garnet), and silicate-oxide (e.g., quartz-magnetite, quartz-ilmenite, quartz-rutile). The volume changes associated to isotopic exchange are even less pronounced than those related to cation exchange, thus making this kind of thermometer effectively independent of pressure, i.e., a "perfect" thermometer. Diffusional re-equilibration can strongly influence isotopic temperatures, however, and may necessitate care in choosing rocks with unusual mineral modes or appropriate assemblages (Eiler et al., 1992; Giletti, 1986; Jenkin et al., 1994; Valley, 2001).

Solvus thermometers

A third type of conventional thermometry relying on the composition of two coexisting phases is solvus thermometry, which is based on the existence of a miscibility gap (i.e., a solvus) between two phases of a solid solution. The composition of the two coexisting phases that have a solvus relationship can be used for thermometry (Fig. 8). Examples are calcite-dolomite, orthopyroxene-clinopyroxene, muscovite-paragonite and plagioclase-K-feldspar pairs. An independent estimate of pressure is

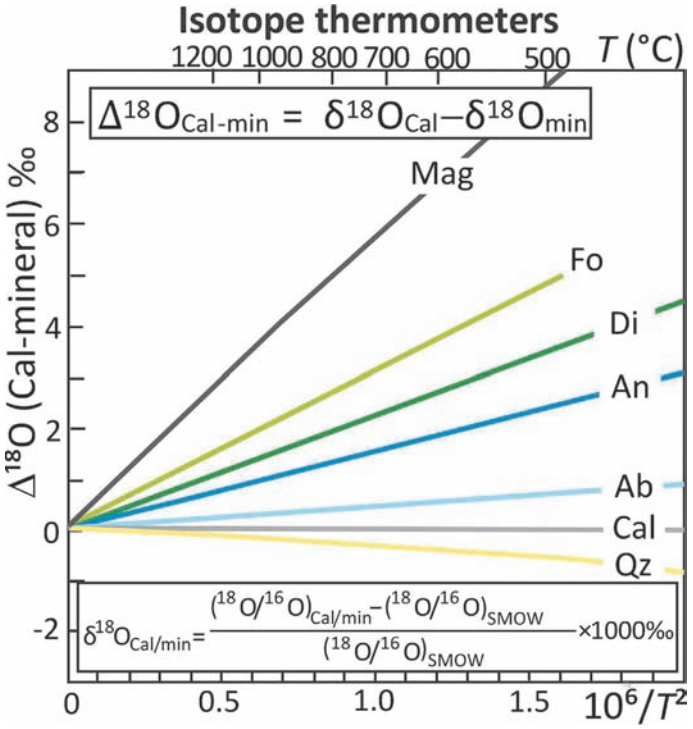

Fig. 7 Experimentally determined oxygen isotope fractionations between calcite and: quartz, albite, anorthite, diopside, forsterite and magnetite (Clayton and Kieffer, 1991). Redrawn from: Valley JW (2001) Stable isotope thermometry at high temperatures. In: Valley JW, Cole DR (eds.), *Stable Isotope Geochemistry, Reviews in Mineralogy and Geochemistry,* vol. 43, pp. 365–414, Mineralogical Society of America: Washington, DC, his Fig. 2. The fractionation of oxygen isotopes between calcite and other minerals ($\Delta^{18}O_{Cal\text{-}min}$) is defined as the difference between the δ value of calcite and the δ value for the mineral, according to the equation reported in the top inset. The δ value of calcite/mineral is defined according to the equation reported in the bottom inset. SMOW: Standard Mean Ocean Water.

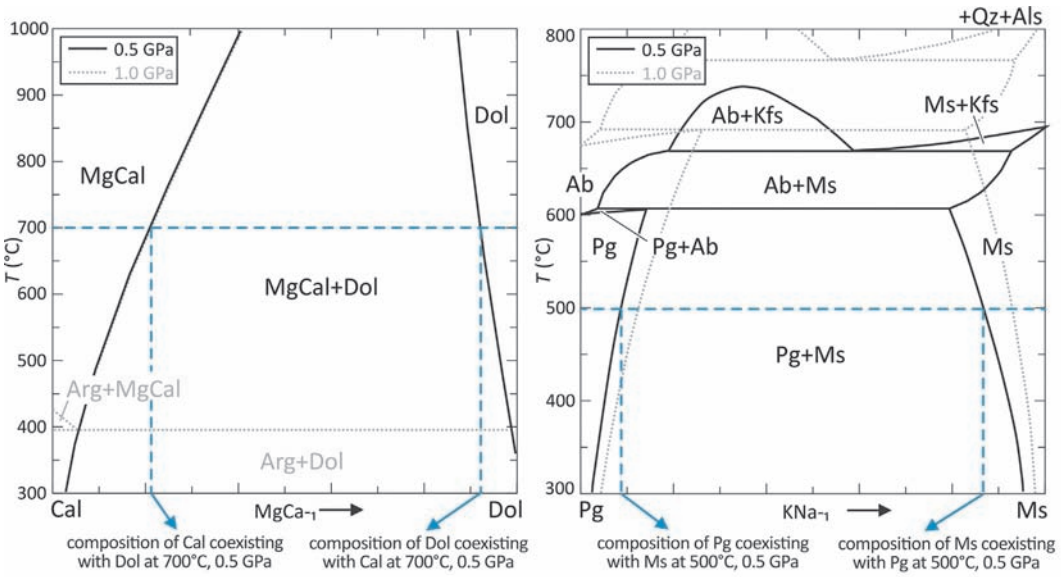

Fig. 8 Solvus relationships between calcite and dolomite (a) and paragonite and muscovite (b), calculated at 0.5 GPa (black lines) and 1.0 GPa (grey dotted lines), using Perple_X (version 6.9.1; Connolly, 1990, 2005, 2009), the Holland and Powell (2011) database (ds62) and the solution models of Anovitz and Essene (1987) and Chatterjee and Froese (1975) for carbonates and white micas, respectively. The compositions of coexisting calcite and dolomite (a) and paragonite and muscovite (b) can be used as geothermometers. Note that, while the calcite-dolomite solvus is not particularly influenced by pressure, the position of the paragonite-muscovite solvus significantly changes at increasing pressures.

required for most of them, because the shape and position of the miscibility gaps change with pressure (Fig. 8b). The sensitivity of the solvus thermometers is generally low at relatively low temperature, where the limbs of the solvus are steeper, and therefore a small error in the estimate of the mineral composition produces a large error in the inferred temperature.

Barometers based on net transfer reactions

Net transfer reactions involve different mineral phases among reactants and products. These reactions are pressure-sensitive because the volume change (ΔV) between products and reactants is significant, and therefore they have a shallow slope in the *PT* space (Fig. 9).

Given the general net transfer reaction: $aA^{y} + bB^{w} = cC^{z}$

where A, B and C are end-members of solid solutions α, β and γ, respectively, a, b, and c are the corresponding stoichiometric coefficients, and y, w and z are the number of sites (site multiplicities) over which the mixing takes place in the solid solutions α, β and γ, respectively, the equilibrium constant for the reaction is defined as (Eq. 3):

$$K = \frac{\left(a_{\mathrm{C}}^{\gamma}\right)^{\mathrm{c}}}{\left(a_{\mathrm{A}}^{\alpha}\right)^{\mathrm{a}} \cdot \left(a_{\mathrm{B}}^{\beta}\right)^{\mathrm{b}}}$$

Assuming an ideal behavior for all solutions (i.e., $a_{\mathrm{i}} = X_{\mathrm{i}}$) to simplify, the equation becomes:

$$K_{\mathrm{N}} = \frac{\left[\left(X_{\mathrm{C}}^{\gamma}\right)^{\mathrm{z}}\right]^{\mathrm{c}}}{\left[\left(X_{\mathrm{A}}^{\alpha}\right)^{\mathrm{y}}\right]^{\mathrm{a}} \cdot \left[\left(X_{\mathrm{B}}^{\alpha}\right)^{\mathrm{w}}\right]^{\mathrm{b}}}$$

with K_{N} defined as the equilibrium constant for a heterogeneous reaction (e.g., Thompson, 1984).

A list of the net transfer reactions most commonly used as barometers, with the relevant references, is provided in the majority of textbooks (e.g., Spear, 1993; Bucher and Grapes, 2011; Winter, 2010). Examples of assemblages that define net transfer reactions are: garnet-aluminosilicate-quartz-plagioclase (GASP), garnet-rutile-aluminosilicate-ilmenite-quartz (GRAIL), garnet-rutile-ilmenite-plagioclase-quartz (GRIPS), garnet-muscovite-plagioclase-biotite which can be applied to pelitic rocks, and clinopyroxene-quartz-plagioclase, garnet-hornblende-plagioclase-quartz, garnet-plagioclase-orthopyroxene-quartz, and garneplagioclase-clinopyroxene-quartz, which can be applied to mafic rocks.

Strengths and weaknesses of conventional thermobarometry

Conventional thermobarometry, which typically combines individual thermometers and barometers to obtain a *P–T* intersection, was the dominant approach for constraining the peak *P–T* conditions experienced by metamorphic rocks since the 1980s for about 20–25 years (Essene, 1982). Currently, this approach is less fashionable, although its basic principles still apply and provide an indispensable framework for other inverse modeling techniques (e.g., multi-equilibrium thermobarometry, see section

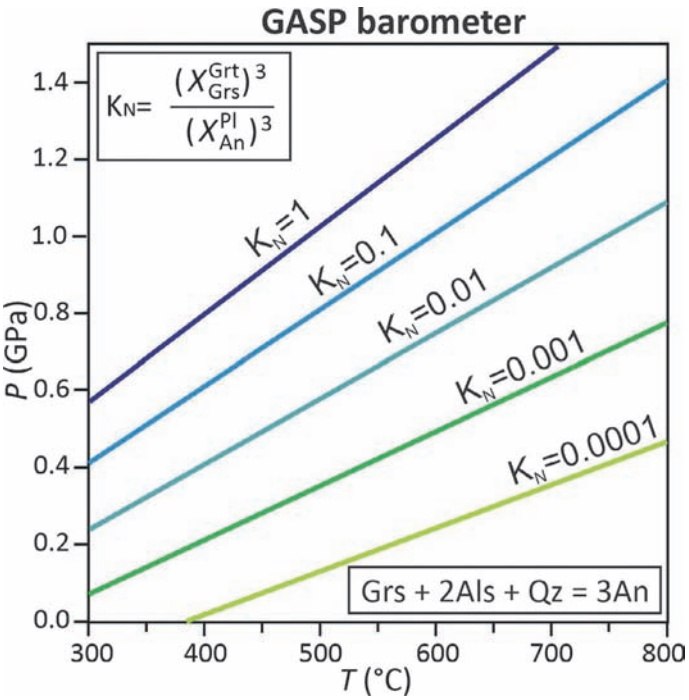

Fig. 9 Lines of constant K_{N} for the GASP barometer plotted in the *PT* space using the equation of Spear (1993). This geobarometer is based on the net transfer reaction Grs + 2Als + Qz = 3An, and has a shallow slope in the *PT* space. Assuming an ideal behavior for both garnet and plagioclase solutions (i.e., $a_{\mathrm{i}} = X_{\mathrm{i}}$), the K_{N} of the reaction is defined according to the equation reported in the inset. Note that $X_{\mathrm{Grs}}^{\mathrm{Grt}}$ is cubed because mixing of Ca in garnet occurs on three sites.

"Multi-equilibrium thermobarometry"). Calibrations of new thermobarometers have been indeed proposed in recent years, documenting a still lively interest on the topic (e.g., amphibole-plagioclase barometer: Molina et al., 2015; garnet-biotite-muscovite-plagioclase barometer: Wu, 2015; garnet-biotite-aluminosilicate-quartz barometer: Wu, 2017; garnet-clinopyroxene and garnet-orthopyroxene thermometers: Sudholz et al., 2022).

The major weaknesses of conventional thermobarometry are (see also Powell and Holland, 2008; Spear, 1993; Kohn, 2014a): (1) the choice of the mineral compositions relies on the experience of the user: two minerals that appear in equilibrium from a microstructural point of view, may not be so from a chemical point of view and, if their compositions are implemented in thermobarometry, they can produce erroneous results; (2) the existence of a plethora of different calibrations for the same equilibria, which confuse—rather than help—the users; (3) the lack of consistency between many thermometers and barometers (e.g., they do not use the same *a-X* models for the same minerals) which, if combined together, can produce erroneous results; (4) many thermometers and barometers have been calibrated at much higher *P–T* conditions with respect to the *P–T* range over which they are generally applied, thus requiring large extrapolations toward lower *P–T* conditions which can be source of errors; (5) retrograde exchange of Fe and Mg by diffusion may significantly modify mineral compositions, which can no longer be used to estimate peak conditions, although methods have been developed to recognize and correct for these problems (e.g., Kohn, 2014a; Kohn and Spear, 2000; Pattison et al., 2003; Spear, 1991; Spear and Florence, 1992); (6) the uncertainties on individual *P–T* estimates are generally large—many tens of degrees and up to tenths of a GPa (see Kohn and Spear, 1991 and Spear, 1993 for a detailed discussion about uncertainties in thermobarometry).

Nevertheless, the conventional thermobarometry approach has some indisputable advantages: (1) it is easy and quick to use, because the only information needed are the mineral compositions and the equations describing the dependence of *K* from *T* and/or *P*; (2) it has quantifiable uncertainties; (3) it allows a rapid comparison among samples characterized by similar assemblages (i.e., relative thermobarometry; Kohn and Spear, 1991; Powell and Holland, 2008; Spear, 1989; Worley and Powell, 2000) and, if used in this way, the uncertainties on the *P–T* differences among samples are much smaller than the absolute uncertainties for a single sample (e.g., Kohn, 2008; Kohn and Spear, 1991); (4) it is especially useful in those situations where the application of forward modeling approaches is problematic, such as the case of carbonate-bearing rocks, in which the composition of the fluid is difficult to constrain (e.g., Castelli et al., 2007).

Among the recent literature which used conventional thermobarometric methods to constrain peak *P–T* conditions of metamorphic terranes, the review by Kohn (2014b) is worth considering for the large number of samples (ca. 300) and for the application of different conventional thermometers and barometers (Grt-Bt, Grt-Hbl, Grt-Pl-Ms-Bt, Grt-Pl-Als-Qz, Grt-Pl-Hbl-Qz) with broadly consistent calibrations on different lithologies, which all together produce coherent and reliable results.

Single phase thermobarometry

Single phase thermobarometry is another type of inverse modeling approach based on measured mineral compositions; it differs from conventional thermobarometry because it depends on the distribution of a single element within a single phase, rather than the distribution of two or more elements among a mineral pair or a group of minerals. Elements involved in this group of thermobarometers are either major elements contained in major phases (e.g., Si-in-phengite, Ti-in-biotite), or elements contained in trace amounts in major or accessory phases (i.e., trace element thermometers, although these are technically net transfer and solvus reactions). For both groups, the crucial pre-requisite is that these thermobarometers can be applied only if the appropriate mineral assemblage to buffer the thermobarometer is present (e.g., rutile must be present in the reactive metamorphic assemblage for ensuring the TiO_2-saturated system necessary to apply the Ti-in-biotite, Ti-in-zircon and Ti-in-quartz thermometers). Alternatively, the activity of the relevant components must be somehow constrained (e.g., Chambers and Kohn, 2012; Ferry and Watson, 2007; Penniston-Dorland et al., 2018).

Single phase thermobarometry involving major elements

Two major single phase thermobarometers are potentially applicable to a wide range of metamorphic rocks: the Si-in-phengite barometer and the Ti-in-biotite thermometer.

The Si-in-phengite barometer is based on the widespread observation that phengite becomes progressively enriched in the celadonite component at increasing pressure, caused by the Tschermak's substitution $^{VI}(Mg + Fe^{2+})^{IV}Si–^{VI}Al^{IV}Al$. This enrichment is testified by the increase in Si content from 3.0 a.p.f.u. (pure muscovite) to almost 4.0 a.p.f.u. (pure celadonite) (Fig. 10a). The barometer has been experimentally calibrated by Massonne and Schreyer (1987) for the Phg + Bt + Kfs + Qz assemblage in the KMASH system, and then refined for other assemblages both in the KMASH and KFASH systems (Phg + Tlc + Ky + Qz/Coe: Massonne and Schreyer, 1989; Phg + Prp + Ky + Qz/Coe and Phg + Alm + Ky + Qz/Coe: Massonne and Szpurka, 1997; Fig. 10a). The Si-in-phengite is potentially a powerful barometer because Si isopleths have a small d*P*/d*T* slope and the Si content in phengite increases linearly with pressure (see also the calibration proposed by Caddick and Thompson, 2008); however, mineral assemblage and bulk rock composition have a strong influence on the absolute amounts of Si in phengite, which makes this barometer more suitable for relative barometry rather than for constraining absolute pressure values.

The Ti-in-biotite thermometer is based on the increase of Ti concentration in biotite with increasing temperature, due to the $^{VI}Ti^{IV}Al–^{VI}Al^{IV}Si$ exchange. The thermometer has been empirically calibrated by Henry et al. (2005) for biotite in peraluminous metapelite that contain rutile or ilmenite; the calculated Ti-saturation surface is curved such that for a given *X*Mg value, Ti concentration increases as a function of temperature in a nonlinear fashion, and for a given temperature Ti abundance decreases with an increase in *X*Mg (Fig. 10b). The Henry et al. (2005) thermometer has been revised by Wu and Chen (2015) with the

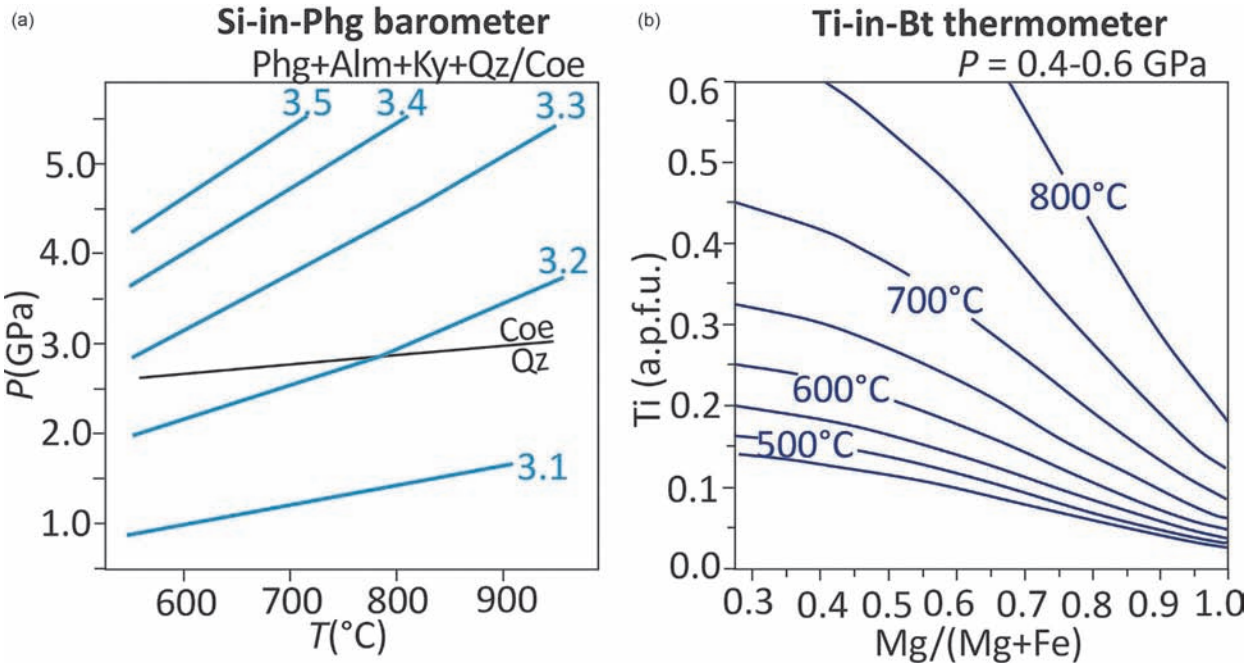

Fig. 10 (a) Si content (a.p.f.u.) of phengite coexisting with quartz/coesite, almandine and kyanite in the KFASH system as calibrated by Massonne and Szpurka (1997). (b) Temperature isotherms (°C) for the Ti-in-biotite thermometer as calibrated by Henry et al. (2005). Redrawn from Massonne HJ and Szpurka Z (1997) Thermodynamic properties of white micas on the basis of high-pressure experiments in the systems K_2O-MgO-Al_2O_3-SiO_2-H_2O and K_2O-FeO-Al_2O_3-SiO_2-H_2O. *Lithos* **41**: 229–250; Henry DJ, Guidotti CV and Thomson JA (2005) The Ti-saturation surface for low-to-mediumpressure metapelitic biotites: Implications for geothermometry and Ti-substitution mechanisms. *American Mineralogist* **90**: 316–328.

addition of a pressure-dependent term, but it remains devoid of thermodynamic bases (i.e., it is empirically calibrated). Although widely applied, the reliability of the Ti-in-biotite thermometer has been questioned (e.g., Chambers and Kohn, 2012) because of its strong dependence on rock composition.

Trace element thermometry

Experimental data demonstrate that the solubility of trace elements in major and accessory minerals is strongly *T*- and *X*-dependent; analysis of their concentration in individual minerals thus give tight constraints on the temperature at which the mineral was formed, provided that an appropriate calibration is available and that the right buffering assemblage is present. The development of trace element thermometry mostly resulted from the progressive advances in high spatial resolution techniques for analyzing trace elements concentrations, such as laser ablation inductively coupled plasma mass spectrometry (LA-ICP-MS) and secondary ion mass spectrometry (SIMS). Most of these thermometers have been calibrated since the 2000s and their widespread application followed the development of conventional thermometry by about 20–25 years. Examples of trace elements thermometry include Zr-in-rutile (Ferry and Watson, 2007; Hofmann et al., 2013; Kohn, 2020; Tomkins et al., 2007; Watson et al., 2006; Zack et al., 2004), Zr-in-titanite (Hayden et al., 2008), Ti-in-zircon (Ferry and Watson, 2007; Hofmann et al., 2013; Tomkins et al., 2007; Watson et al., 2006), Ti-in-quartz (Thomas et al., 2010; Wark and Watson, 2006), and Y-in-garnet (Pyle and Spear, 2000; Pyle et al., 2001). Details about the calibration and application of most of these single element thermometers in metamorphic rocks are presented in the recent review by Cruz-Uribe et al. (2018), see also Yakymchuk et al. (2017), Kohn (2017), Kohn and Penniston-Dorland (2017), Rubatto (2017) and Zack and Kooijman (2017).

For the Zr-in-rutile, Zr-in-titanite, Ti-in-zircon and Ti-in-quartz thermometers the concentration of the trace element (Zr, Ti) in the individual mineral phase (rutile, titanite, zircon and quartz) systematically increases with increasing temperature (Fig. 11); the pressure dependence is relatively low for Zr-in-rutile and Ti-in-zircon (Fig. 11a and c), whereas it is more pronounced for Ti-in-quartz and for Zr-in-titanite (Fig. 11b and d), for which an independent pressure estimate is usually required. These thermometers have been calibrated experimentally at relatively high temperatures and either extrapolated or empirically calibrated toward lower temperature; however, at $T < 500$–600 °C the concentration of Zr in titanite, and of Ti in zircon and quartz is generally lower than the detection limit of most analytical techniques, hampering the application of these thermometers to low-grade metamorphic rocks. Y-in-garnet thermometry differs because the solubility of Y in garnet (in the presence of xenotime) decreases with increasing temperature; this single element thermometer is therefore applicable to low- to medium-grade metamorphic rocks.

Strengths and weaknesses of single phase thermobarometry

The use of trace element thermometry is currently exponentially increasing thanks to: (1) the relative ease of the method (it requires the analysis of a single element in a single phase), (2) the common occurrence of quartz and garnet as major minerals, and of zircon, rutile and titanite as accessory phases in a large variety of lithologies, and (3) the possibility of using some of these thermometers

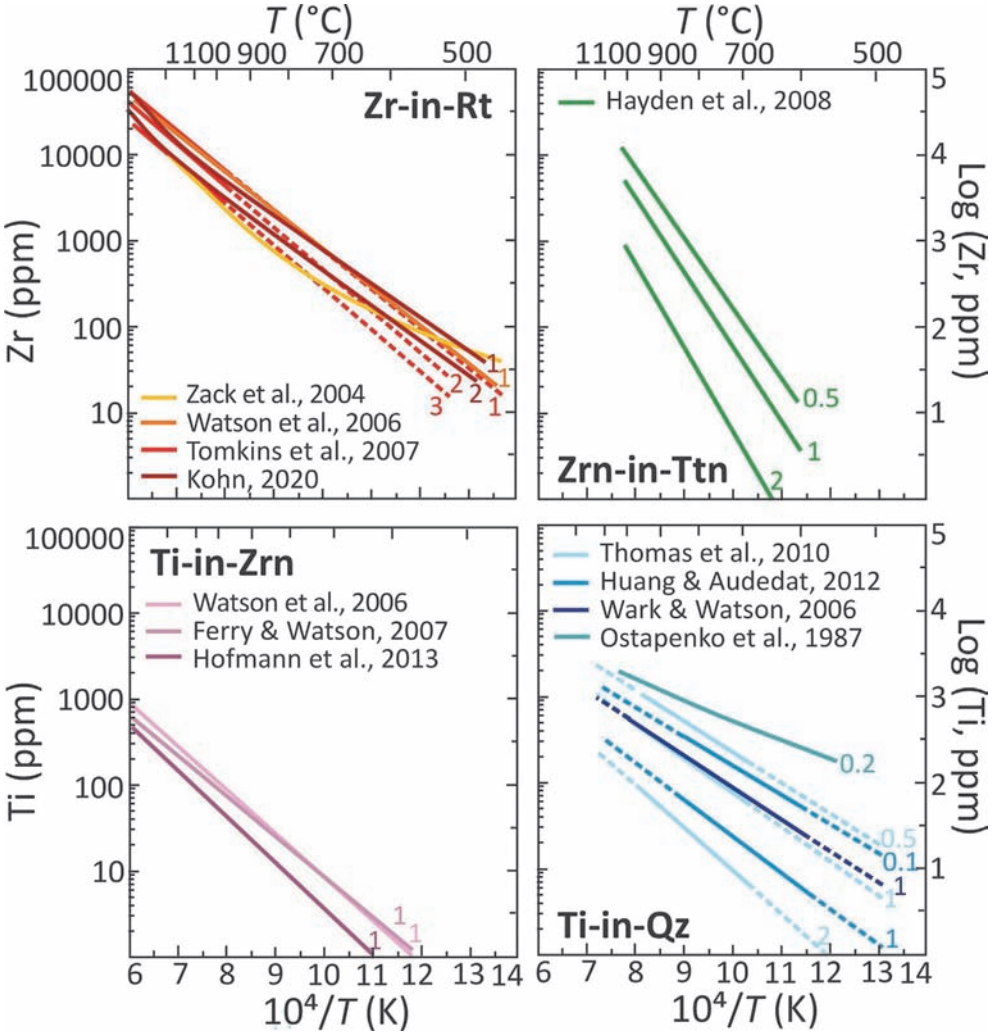

Fig. 11 Empirical and experimental calibration curves for (a) Zr-in-rutile (Tomkins et al., 2007; Watson et al., 2006; Zack et al., 2004), (b) Zr-in-titanite (Hayden et al., 2008), (c) Ti-in-zircon (Ferry and Watson, 2007; Hofmann et al., 2013; Watson et al., 2006;) and (d) Ti-in-quartz (Huang and Audétat, 2012; Thomas et al., 2010; Wark and Watson, 2006) thermometers, for a range of pressure (reported close to each curve, GPa). Temperature ranges over which the calibrations are experimentally constrained is indicated by the solid lines; dashed lines indicate extrapolation of the calibration over a wider temperature range. Modified from Cruz-Uribe AM, Feineman MD, Zack T, Jacob DE (2018) Assessing trace element (dis)equilibrium and the application of single element thermometers in metamorphic rocks. *Lithos* **314–315**: 1–15, their Figs. 1–4.

also as geochronometers (e.g., Kohn, 2016, 2017; Rubatto, 2017; Zack and Kooijman, 2017), thus simultaneously constraining the thermal history and the age (T–t) in a single micro-analytical spot (i.e., petrochronology: Engi et al., 2017). The main weaknesses of the method rely on: (1) the difficulty in resolving zoning, due to the relatively large spot size of the LA-ICP-MS technique, especially if compared to that of EPMA which is normally used for conventional thermometry, and (2) the difficulty in understanding to what extent accessory phase equilibrium and trace element equilibrium are attained in metamorphic rocks (e.g., Cruz-Uribe et al., 2018). Several studies have shown good internal consistency in the application of Zr-in-rutile both to moderate-grade metamorphic rocks (e.g., Kohn, 2020) and even in ultra-high temperature rocks (e.g., Qi et al., 2022); however, others suggest caution in the application of single element thermometry even in the case a buffering assemblage is present (e.g., quartz + rutile for Ti-in-quartz, or rutile + zircon for Zr-in-rutile: Kendrick and Indares, 2018).

Multi-equilibrium thermobarometry

TWEEQU and Average P–T

Multi-equilibrium thermobarometry is another type of inverse modeling approach, based on the idea that, rather than using selected individually calibrated reactions, P–T conditions can be estimated solving all possible equilibria (or an independent set of equilibria) that can be written between the end members of each phase in a specific assemblage (Berman, 1991), and finding the intersection among all these reactions in the PT space (Fig. 12). This method requires the use of an internally consistent thermodynamic database (Berman, 1991; Powell and Holland, 1988, 1994) and of appropriate a-X relations for the solution

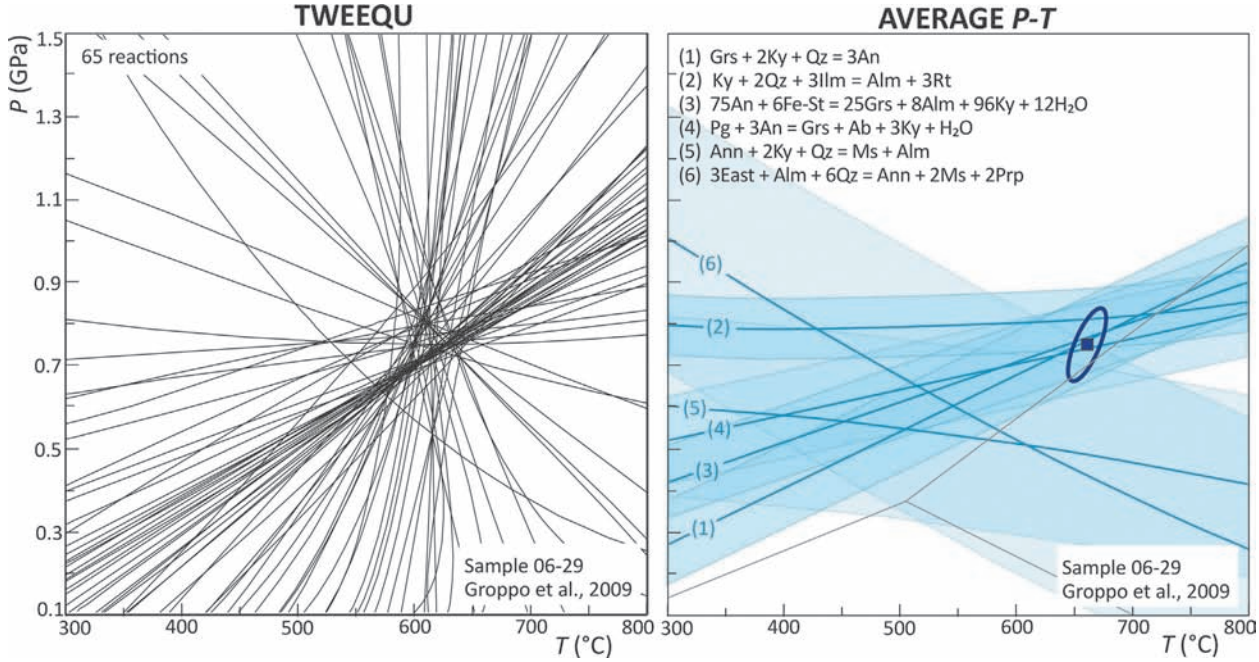

Fig. 12 Multi-equilibrium thermobarometry solution for a two-micas, garnet + staurolite + kyanite -bearing schist from the Greater Himalayan Sequence of eastern Nepal Himalaya (sample 06-29 in Groppo et al., 2009). The equilibrium assemblage consists of: quartz + white mica + biotite + garnet + plagioclase + staurolite + kyanite + ilmenite + rutile. Mineral compositions used for both diagrams (a) and (b) are reported in Groppo et al. (2009), their Tables 1–4 (analyzes with *). The phase diagram (a) is calculated using winTWQ (version 2.64f) of Berman (1991), the Berman and Aranovich (1996) database and the solution models of Fuhrman and Lindsley (1988) for plagioclase, Berman (2007) for garnet and biotite, and Chatterjee and Froese (1975) for white mica. The phase diagram (b) is calculated using Average *P–T* of THERMOCALC (version 3.40) (Powell and Holland, 1994) and the Holland and Powell (2011) dataset (ds62); activity-composition relationships are calculated using the software AX. The light blue fields refer to the 2σ uncertainties associated to each reaction; the blue square and the ellipse define the optimal *P–T* conditions (square) determined by Average *P-T*, with the correspondent uncertainty (ellipse). All reaction equations are written such that the high-*T* assemblage is on the right side.

phases involved. An efficient computer code able to perform the computation of the equilibrium conditions (i.e., to solve Eq. 1) for a large number of reactions is also required. Two main programs have been developed to perform multi-equilibrium calculations, TWEEQU (Berman, 1991) and Average *P–T* (Powell and Holland, 1994; Powell et al., 1998), which are reviewed in detail by Lanari and Duesterhoeft (2019).

Input data for both programs include the list of the phases present in the equilibrium assemblage, the measured mineral compositions, and the appropriate solution models. The two programs rely on different thermodynamic databases and associated solution models (i.e., TWEEQU: Berman, 1988; Berman and Aranovich, 1996; Average *P–T*: Powell and Holland, 1994, Holland and Powell, 2011). The main difference among them concerns the evaluation of the uncertainties. Basically, TWEEQU does not consider the uncertainties related to each equilibrium, i.e., it attributes the same importance to all the reactions, with no information on whether equilibria are more or less well constrained. By contrast, Average *P–T* (which is part of the THERMOCALC package; Powell and Holland, 1988) applies a weighted least squares scheme to a set of independent reactions to adjust the input data (mainly by varying the activities of the end-members of the minerals, in proportion to their uncertainties), such that the selected equilibria intersect at one "optimal" *P–T* point.

Strengths and weaknesses of multi-equilibrium thermobarometry

The major strength of multi-equilibrium thermobarometry is the possibility of solving a large number of equilibria in the context of an internally consistent thermodynamic database, which allows minimizing the errors of individual calibrations and overcoming the absence of consistency between independent calibrations (i.e., limitations of conventional thermobarometry; see section "Strengths and weaknesses of conventional thermobarometry"), as well as avoiding the uncertainties associated with bulk composition assumptions (i.e., limitations of the forward modeling approach; see section "Strengths and weaknesses of isochemical *P–T* phase diagrams"). An additional advantage of the Average *P–T* method is its ability to estimate the uncertainties associated to the *P–T* estimates (based on the Δ*H* of the dataset). Moreover, the method is fast and easy, thus explaining why it has been widely used since the 1990s, especially for relative thermobarometry, and often in association with the forward modeling approach.

The main weaknesses of the TWEEQU method are: (1) its inability of estimating the uncertainties related to each equilibria, with the consequence that the user cannot understand which is the real "weight" of the calculated reactions; this limit has been partially overcome in the last version of TWEEQU (winTWQ; Berman, 2007), which allows defining average *P–T* results using a selected set of independent equilibria that are considered more robust, although uncertainties remain undetermined; and (2) the fact that the

database and solution models on which it relies on do not include the thermodynamic properties for some relatively common end-members and solid solutions (e.g., chloritoid and phengite). On the other hand, the main weaknesses of Average *P–T* include: (1) the uncertainties are often large and depend on arbitrarily assigned errors in activities, (2) it commonly requires an estimate of aH_2O for assemblages with hydrous minerals, which can be difficult to be independently constrained, and (3) for high-variance assemblages (i.e., assemblages consisting of few phases) the number of calculated equilibria is often too low to converge to a result.

Among the recent literature, the paper by Goscombe et al. (2018) provides a valuable example of application of multi-equilibrium thermobarometry (Average *P–T*) on a huge number of samples (ca. 160) with similar features but slightly different bulk compositions. The possibility of applying this method in series is extremely advantageous in cases where the goal is to compare the *P–T* conditions of a very large sample dataset.

Spectroscopic thermobarometry

In the panorama of inverse modeling approaches, two methods (i.e., Raman Spectroscopy of Carbonaceous Material and elastic thermobarometry) differ from those described so far because they are virtually independent of a mineral's composition. Although less pertinent to the focus of this review, these methods are nevertheless worth mention, because they provide an alternative to, and are often combined with, other thermobarometric tools. Both methods rely on the structural modification of a phase (graphite for Raman Spectroscopy of Carbonaceous Material; any phase included in a host for elastic barometry, e.g., quartz included in garnet) in response to variations in temperature and/or pressure; these structural modifications can be detected using micro-Raman spectroscopy (giving rise to the term "thermoba-Raman-try"; Kohn, 2014c) or micro-XRD (e.g., Alvaro et al., 2020). These methods were reviewed recently by Korsakov et al. (2020) and Kohn et al. (2023).

RSCM thermometry and elastic barometry

The Raman Spectroscopy of Carbonaceous Material (RSCM) method is based on the observation that carbonaceous material in sedimentary protoliths is progressively transformed in graphite during prograde metamorphism, and that its degree of crystallization increases with increasing metamorphic grade. The graphitization process is irreversible, therefore the structure of carbonaceous material is not modified during retrograde metamorphism and basically reflects the maximum-*T* reached during metamorphism. A linear relationship between temperature and the structural state of carbonaceous material quantified through micro-Raman spectroscopy was found by Beyssac et al. (2002a, 2002b). Their calibration can be applied on both regional and contact metamorphic rocks, from very low temperatures (ca. 200 °C) and up to ca. 650 °C (Aoya et al., 2010; Beyssac et al., 2019; Lahfid et al., 2010).

Elastic barometry is based on the observation that minerals trapped as inclusions in a host mineral develop a non-lithostatic stress (i.e., residual pressure, either positive for compressive or negative for tensile) during both prograde and retrograde metamorphism, because of the differences between the thermo-elastic properties of the host and those of the inclusion (Angel et al., 2014, 2015; Enami et al., 2007; Kohn, 2014c; Rosenfeld and Chase, 1961). This residual pressure can be determined using micro-Raman spectroscopy; more specifically, micro-Raman spectroscopy provides an estimate of the strain on the inclusion, which can be used to calculate the residual pressure. Once the residual pressure of the inclusion is known, the application of a thermo-elastic model permits calculation of the entrapment pressure, provided that the temperature is independently constrained. Details for the calculation of strains from Raman shifts and residual pressure from strains are given by Angel et al. (2017, 2019), Gonzalez et al. (2019) and Gilio et al. (2021). This method, which is potentially applicable on any host-inclusion system, was first calibrated for the quartz-garnet pair (i.e., quartz-in-garnet barometer, QuiG; Rosenfeld and Chase, 1961).

Strengths and weaknesses of spectroscopic thermobarometry

Both methods are especially useful in those lithologies where conventional (i.e., chemical) thermobarometers cannot be used due to the lack of diagnostic mineral assemblages and/or the diffusional modification of equilibrium mineral compositions. They are also particularly suitable for systems that involve mixed-volatile fluids (e.g., carbonate-bearing rocks), for which the forward modeling approach is more difficult to be applied (see section "Constraining fluid evolution"). Since their first calibrations (Angel et al., 2014; Ashley et al., 2014; Beyssac et al., 2002a, 2002b; Kohn, 2014c), these methods have met great interest in the metamorphic petrology community and are currently quite in vogue.

Limitations of the RSCM method include: (1) the application to polymetamorphic rocks can be problematic (Beyssac et al., 2019), and (2) if graphite precipitated from a fluid rather than being the recrystallization product of sedimentary carbonaceous material, the RSCM temperatures are meaningless (e.g., Luque et al., 2009; Perraki et al., 2006). The main weaknesses of the elastic barometry are: (1) geometric features of the inclusion (size, shape and position of the inclusion) can significantly influence stress. Ideally, inclusions should be small and trapped in an effectively infinite host (Angel et al., 2017), and they should be located at a distance two to three times their radius beneath the polished surface; (2) application of the barometer to elastically anisotropic inclusions (e.g., quartz) requires corrections of the models (e.g., Campomenosi et al., 2018; Mazzucchelli et al., 2018, 2019); (3) many studies show data scatter that exceeds analytical error for reasons that are not altogether clear (Kohn et al., 2023); (4) at elevated temperature, viscous relaxation of residual stresses can occur (Moulas et al., 2019; Zhong et al., 2020) and inclusions can modify shape (Cesare et al., 2021).

Isochemical *P–T* phase diagrams

Calculation of isochemical phase diagrams (i.e., forward modeling) requires choosing: (i) appropriate thermodynamic data, (ii) an appropriate model system, and (iii) a representative bulk composition. The definition of all these factors is not trivial (e.g., Robinson, 1991); several practical aspects concerning these choices are reported in the following sections; for further information, the reader should refer to the specific papers suggested in each section.

Choice of the appropriate thermodynamic data

Forward thermodynamic modeling is based on the availability of: (i) an internally consistent thermodynamic dataset containing the thermodynamic properties of the end members components, and (ii) compatible activity-composition (*a-X*) models describing how these end members are combined to form the solution phases. An excellent review of the importance of internally consistent thermodynamic database, of the techniques used for creating such database and of the differences between them is provided by Lanari and Duesterhoeft (2019); the same paper also provides a complete treatment of simple and complex solution models and of the methods used for their calibration. Two groups of internally consistent dataset are widely used by the metamorphic petrology community, built on the original dataset of Berman (1988) and Holland and Powell (1985), respectively. The Berman (1988) dataset was updated 20 years later (Berman, 2007), and successively implemented/modified by Spear and Pyle (2010) and Pattison and DeBuhr (2015); it now includes properties of a hundred end-members (and employs simplified solution models; de Capitani and Petrakakis, 2010). The Holland and Powell (1985) dataset has been continuously updated over the years (e.g., Holland and Powell, 1988, 1990, 1998); its last version (ds62: Holland and Powell, 2011), which includes properties for more than 250 end members, is likely the most complete dataset currently available for modeling metamorphic systems.

Solution models are calibrated for a specific dataset, thus implying that the choice of *a-X* models to be used in the calculation cannot be random, but must be consistent with the chosen dataset (e.g., the White et al., 2014a, 2014b and the Green et al., 2016 solution models should be used in association with the Holland and Powell, 2011 dataset). A comparison among the behavior of the two groups of database and/or among different versions of the same database is provided by some recent papers including Guevara and Caddick (2016), Kendrick and Indares (2018), Waters (2019), and Nagurney et al. (2021).

Choice of the model system

Although the model system is always a simplification of the natural system, it should include all the components sufficient to represent the composition of all the phases of interest and to describe their compositional variations in *PT* space. Its definition is of crucial importance, because components that are not considered in the modeling may affect phases stability in nature in two ways (e.g., Zuluaga et al., 2005): (i) components that do not result in the growth of additional phases in the system, enter existing solid solutions and change their compositions, stability fields, and the variance of assemblages. An example is MnO, whose introduction in the KFMASH system stabilizes garnet at lower *P* and *T* (e.g., Mahar et al., 1997; Spear and Cheney, 1989; Tinkham et al., 2001); (ii) components that cause growth of additional minerals can change the proportions of the other components available to other phases, with consequences on their stability fields and compositions. An example is TiO_2, whose inclusion in the KFMASH system stabilizes ilmenite, which removes FeO to the system, making it less available for the other phases (e.g., White et al., 2000). Generally, the larger the model system, the better the approximation of the natural system.

Choice of the representative bulk composition

Two major strategies are commonly adopted to obtain the bulk composition: (i) the conventional whole-rock analyzes (e.g., XRF or ICP-MS), and (ii) a weighted calculation that combines mineral modes (obtained either by point counting methods or by processing major element mapping of the whole thin section) with mineral compositions. Advantages and disadvantages of both methods are discussed in detail by Palin et al. (2016). The measured bulk rock composition may not coincide with the so called "effective bulk composition" (Evans, 2004; Hickmott et al., 1987; Marmo et al., 2002; Robinson, 1991; Spear et al., 1990; Spear and Wolfe, 2018; Stüwe, 1997; Tinkham and Ghent, 2005; Tracy, 1982) or "reactive bulk composition" (Lanari and Engi, 2017; Smye et al., 2010), a term used to define the composition of the local chemical system available for the mineral reactions in the sample. Definition of the reactive bulk composition requires understanding the scale of equilibration in the sample. Lanari and Engi (2017) present a comprehensive discussion of this complex and debated issue, which is instead treated here in a simplified way, with emphasis on practical aspects. The reactive bulk composition differs from the measured bulk rock composition in three main situations: (a) when the investigated sample contains zoned crystals, especially garnet (but also plagioclase), (b) when the sample shows clear textural evidence of relict metastable minerals, derived either from the protolith or from an earlier metamorphic cycle (i.e., in the case of polymetamorphism), and (c) if the sample experienced anatexis and melt was partially or completely extracted from the system.

(a) Chemical fractionation of the bulk rock composition commonly occurs in the presence of zoned garnet porphyroblasts, due to the preferential sequestration of some elements (especially Mn) in the porphyroblasts' cores and the consequent progressive depletion of these elements in the surrounding matrix. The more abundant the porphyroblasts are and the greater is the difference in composition between the porphyroblasts and the matrix, the more evident are the fractionation effects (Marmo et al., 2002). Based on sensitivity tests, Lanari and Engi (2017) concluded that fractionation effects become significant as soon as garnet porphyroblasts represent >2 vol% in pelitic systems and >4 vol% in mafic systems. Different strategies can be adopted to consider the chemical fractionation effects due to the growth of zoned garnet porphyroblasts, including:

(i) simplified fractionation modeling based on the progressive subtraction of different garnet domains from the measured bulk composition (e.g., Caddick et al., 2007; Groppo et al., 2019; Manzotti et al., 2022; Marmo et al., 2002; Tinkham and Ghent, 20,005; Zuluaga et al., 2005;); (ii) a step-by-step modification of the bulk rock composition between a series of *P–T* increments, according to the predicted element incorporation in the fractionated phases (e.g., Konrad-Schmolke et al., 2008); (iii) a Rayleigh fractionation model based on MnO garnet zoning profiles (e.g., Evans, 2004; Gaidies et al., 2006; Groppo and Castelli, 2010): (iv) an automated fractional crystallization model (e.g., Gaidies et al., 2008; Lanari et al., 2017; Moynihan and Pattison, 2013; Vrijmoed and Hacker, 2014). Whatever the method used, chemical fractionation of the bulk composition requires calculating a number of separate MADs, each one using the effective bulk composition that was reactive during the growth of a specific garnet domain (e.g., core, mantle, rim) (Fig. 13). Each MAD must then be used for constraining the growth *P–T* conditions of the correspondent garnet domain.

(b) The preservation of relict metastable minerals implies that they have not been involved in the reactive bulk composition, and they should be therefore removed from the measured bulk composition. In such a case, methods based on minerals mode combined with mineral compositions are essential for estimating the reactive bulk rock composition (Lanari and Hermann, 2021; Palin et al., 2016).

(c) Strategies for retrieving the reactive bulk rock composition in the case of melt loss are based on the re-integration of melt back into the measured bulk rock composition and are discussed in detail in several papers, among which Bartoli (2017, and references therein), Diener et al. (2014), Groppo et al. (2012, 2013b), Indares et al. (2008), Johnson et al. (2021, and references therein), White et al. (2004, 2007), White and Powell (2002). This issue is not further discussed in this review.

Isopleth thermobarometry

Once that the input data are defined and the isochemical phase diagram is modeled, equilibrium *P–T* conditions can be further constrained by comparing the predicted mineral assemblages, modes and compositions with the observed ones. A first constraint is given by the modeled field which matches the observed mineral assemblage (Fig. 13); however, this preliminary information should be always refined (and cross-checked) by locating the modeled compositional isopleths (and isomodes) correspondent to the measured mineral compositions (and modes). If the observed mineral assemblage and composition reflect equilibrium conditions, the modeled isopleths (and isomodes) should intersect (or converge) in a single, narrow, *P–T* domain (Fig. 13). The method is called isopleth thermobarometry. Calculation of more than one isochemical phase diagram using different reactive bulk compositions, each one representative of the assemblage stable at a specific metamorphic stage, helps constrain different *P–T* points, and ultimately reconstructing the whole (or a part of the) *P–T* path (Figs. 13 and 14).

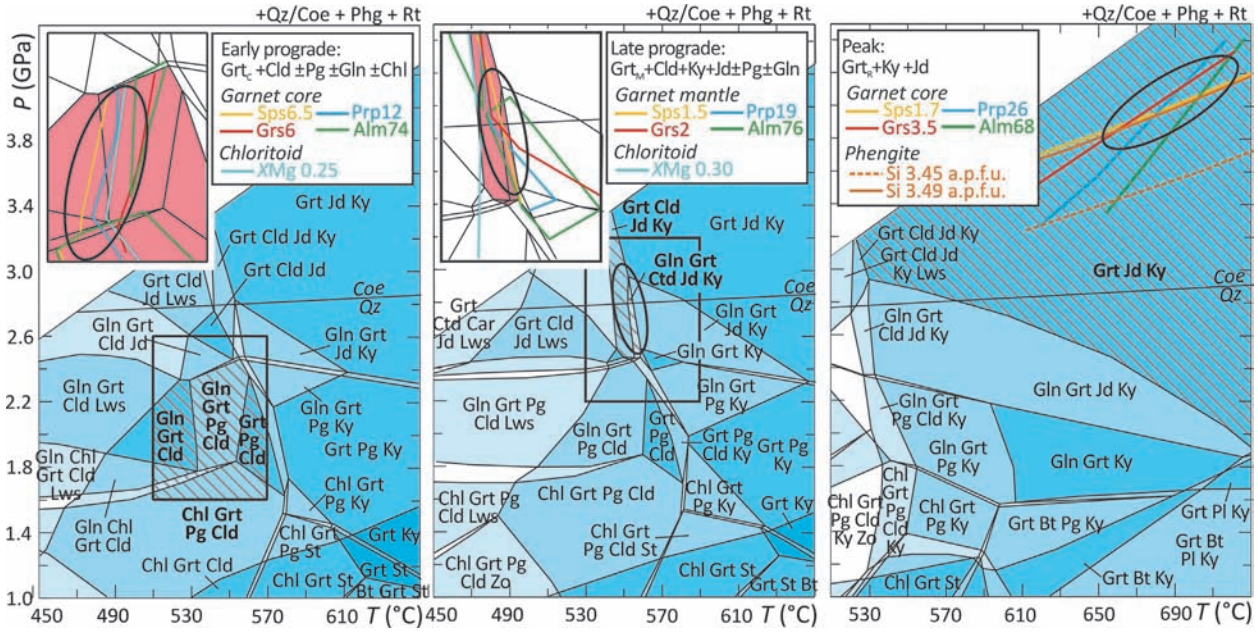

Fig. 13 *P–T* isochemical phase diagrams modeled for a garnet + kyanite + jadeite -bearing phengitic micaschist from the ultra-high pressure Brossasco-Isasca Unit of the Dora-Maira massif, western Alps (sample DM1281 in Groppo et al., 2019). The phase diagrams are calculated using Perple_X (version 6.9.1; Connolly, 1990, 2005, 2009), the Holland and Powell (2011) database (ds62), the solution models of White et al. (2014a, 2014b) and three different bulk compositions: the measured bulk-composition (a), and the reactive bulk compositions after fractionation of garnet core (b) and of garnet core + mantle (c). The three phase diagrams thus allow modeling the early prograde (a), late prograde (b) and peak (c) assemblages and compositions, defined in the top insets and highlighted by the dashed fields in each diagram (red fields in the zoomed insets in a and b). Black ellipses define early prograde, late prograde and peak *P–T* conditions, constrained using the modeled compositional isopleths for garnet, chloritoid and phengite (colored lines, zoomed in the a and b insets). Variance of the fields varies from 2 (white) to 6 (darker blue). Redrawn from Groppo C, Ferrando S, Gilio M, Botta S, Nosenzo F, Balestro G, Festa A, Rolfo F (2019) What's in the sandwich? New P–T constraints for the (U)HP nappe stack of southern Dora-Maira Massif (Western Alps). *European Journal of Mineralogy* **31**: 665–683.

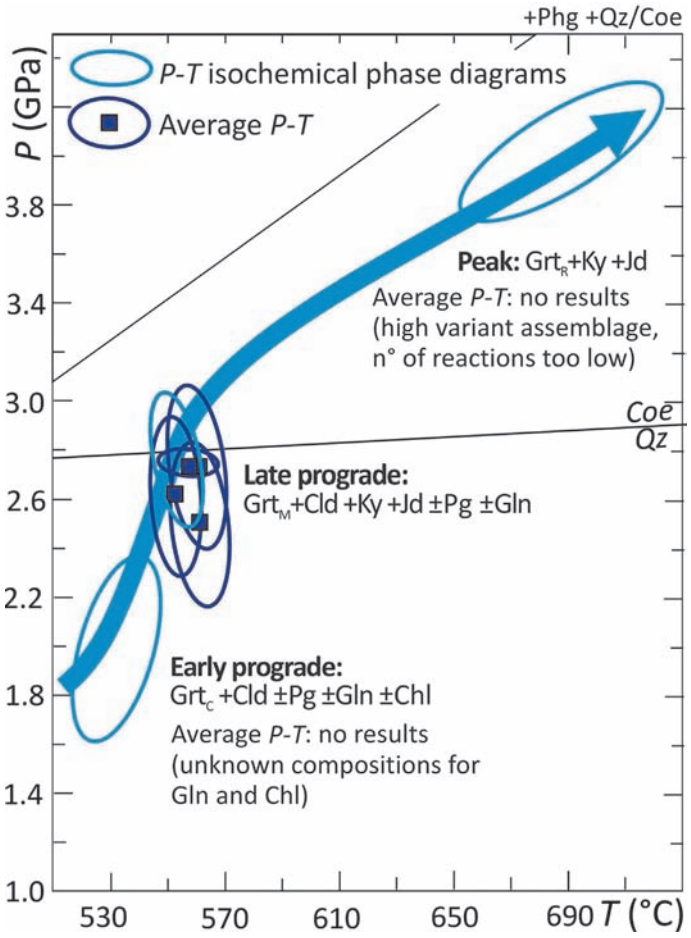

Fig. 14 Comparison between the results of inverse (multi-equilibrium thermobarometry: Average *P–T*) and forward modeling approaches applied on the same sample (sample DM1281 in Groppo et al., 2019) and using the same database and mineral compositions. Light blue ellipses represent the early prograde, late prograde and peak *P–T* conditions constrained by the *P–T* isochemical phase diagrams (see Fig. 13). The blue squares and ellipses define the optimal *P–T* conditions (squares) with the correspondent uncertainties (ellipses) determined by Average *P–T*, applied on four set of mineral compositions from the late prograde assemblage. The blue arrow represents the inferred *P–T* path for the studied sample. Note that Average *P–T* fails in defining early prograde and peak *P–T* conditions (and consequently the *P–T* path). Redrawn from Groppo C, Ferrando S, Gilio M, Botta S, Nosenzo F, Balestro G, Festa A, Rolfo F (2019) What's in the sandwich? New P–T constraints for the (U)HP nappe stack of southern Dora-Maira Massif (Western Alps). *European Journal of Mineralogy* **31**: 665–683.

Strengths and weaknesses of isochemical P–T *phase diagrams*

Isochemical phase diagram modeling is commonly considered as the most powerful thermobarometric strategy for constraining the *P–T* evolution of metamorphic rocks (Powell and Holland, 2008). This method started to be used in the early 2000s and exploded about 10 years later, replacing conventional thermobarometry as a routine thermobarometric tool. The popularity of the approach is testified by the overwhelming number of published papers that use this method, especially in the last 5–6 years.

The strengths of the method include: (1) a *P–T* isochemical phase diagram is modeled for a specific reactive bulk composition, and therefore provides thermobarometric information for that specific sample (opposite to *P–T* projections that show all the reactions compatible with a chosen model system); (2) the results do not strictly depend on the observed mineral compositions, thus overwhelming some of the main limits of conventional thermobarometry, i.e., the choice of mineral compositions to be used in the calculation, and the possibility that mineral compositions have been modified by diffusion (see section "Strengths and weaknesses of conventional thermobarometry"); this is particularly useful for high-temperature metamorphic rocks that have undergone retrograde exchange reactions, but have maintained the peak mineral assemblage (and modes); (3) it allows calculation of a wide range of physical and chemical parameters, in addition to isopleths and isomodes; (4) it provides information not only on the peak metamorphic conditions (i.e., a single state of frozen-in equilibrium recorded at a specific point along the *P–T* path), but also on the whole (or a part of the) *P–T* history, provided that an appropriate reactive bulk composition can be obtained; (5) it does not require that the mineral assemblages representative of the various metamorphic stages recorded along a *P–T* path are all preserved, because it can give information also on the stability fields of inferred assemblages (e.g., based on the presence of pseudomorphs).

However, "not all that glitters is gold", and even the forward modeling approach has some limitations. The main weaknesses of isochemical *P–T* phase diagrams include: (1) although phase diagrams are relatively easy to calculate, the underlying assumptions are complex and require experience to reproduce the observed mineral assemblages and compositions, and (moreover) not to misinterpret the results; (2) as a consequence of point (1), its application in series (i.e., for a large number of samples with similar features but slightly different bulk compositions) is not convenient; (3) choice of an appropriate reactive bulk composition (i.e., deciding which part of a rock equilibrated at any given stage) is crucial to the success of the approach, but it is not trivial, especially in the case of chemical fractionation of the bulk composition; (4) *P–T* isochemical phase diagrams generally do not allow a detailed investigation of univariant reactions, which can be a limit when we are interested in constraining the fluid evolution and/or specific metamorphic processes; and (5) errors are not rigorously quantified.

Inverse vs. forward modeling approaches: A comparison

Strengths and weaknesses of each thermobarometric method discussed in the previous sections highlight that there is no single approach that works for all situations; rather, a reasoned choice should always be made according to the targets to be achieved and the specificity of the samples to be modeled. In the ideal case of a perfectly equilibrated sample, all the approaches, either inverse modeling or forward modeling, should converge toward a similar result. However, two important points must be considered: (1) a quantitative comparison between different approaches is reliable only if these are based on the same thermodynamic data; for example, the results of multi-equilibrium thermobarometry can be directly compared with those of isochemical phase diagrams only if they use the same database and solution models; (2) it is not always possible to apply all the approaches on a single sample. For example, the use of inverse modeling methods is severely limited: (i) when the composition of one or more phase is unknown because its/their occurrence in a specific assemblage is inferred on the basis of pseudomorphs, and (ii) in the case of high variance assemblages, for which the number of independent reactions is often too low for a successful application of multi-equilibrium thermobarometry.

Groppo et al. (2019) provided a practical example of such situations. The prograde *P–T* path of an ultra-high pressure metapelite from the Dora-Maira Massif of the western Alps (sample DM1281) was reconstructed using the forward modeling approach and constraining three distinct metamorphic stages (early prograde, late prograde and peak stages), each one characterized by a specific assemblage (Figs. 13 and 14). The Average *P–T* inverse modeling approach was applied on the same assemblages and using the same database; however, it failed in constraining the *P–T* conditions for both the early prograde and the peak stages. In fact, although the early prograde assemblage (Qz + Phg + Grt + Cld ± Pg ± Gln ± Chl) has a relatively low variance, the composition of two minerals is unknown (i.e., glaucophane is not preserved and chlorite is preserved as rare inclusions in garnet core, but its composition was modified by diffusion). Conversely, the peak assemblage (Coe + Phg + Grt + Ky + Jd) is a high variance assemblage and, therefore, the number of independent reactions calculated by Average *P–T* is too small to converge on a result. Where applicable (late prograde stage; Qz/Coe + Phg + Grt + Cld + Ky ± Gln ± Pg assemblage), the two methods do converge (Fig. 14).

The application of two or more independent approaches to the same sample is often the best strategy for a successful thermobarometric study (e.g., conventional thermobarometry can be combined with spectroscopic thermobarometry and/or trace element thermometry; or the forward modeling approach can be combined with trace elements thermometry, multi-equilibrium thermobarometry and/or spectroscopic thermobarometry). This strategy takes advantage of the complementary nature of most approaches and reinforces the validity of the results (e.g., Dasgupta et al., 2009; Groppo et al., 2019; Manzotti et al., 2022). Alternatively, a single, robust thermobarometric approach should be applied on more than one sample from the same metamorphic unit; in this way, the method is validated if the *P–T* results are comparable for all the samples (e.g., Tamang et al., 2023), although samples from the same unit can record different portions of the same *P–T* trajectory.

Finally, two considerations are worth considering when comparing inverse and forward modeling approaches:

(1) it is impossible to demonstrate the achievement of chemical equilibrium using a purely inverse modeling approach: the convergence of reactions in a narrow *P–T–X* region, in fact, only shows that the selected mineral compositions are consistent with chemical equilibrium at these *P–T* conditions, but does not prove that chemical equilibrium was effectively achieved, i.e., that the total Gibbs free energy of the selected assemblage was minimal (Lanari and Duesterhoeft, 2019). This disadvantage is overwhelmed by the forward modeling approach, although the metastable persistence of mineral relics outside their stability fields can complicate the application of this approach and the interpretation of the results (see Lanari and Hermann, 2021 for an alternative approach, briefly mentioned in section "Concluding remarks and perspectives").
(2) On the other hand, most of the inverse thermobarometric methods have quantifiable uncertainties, whereas MAD models still do not.

Constraining fluid evolution

Why constrain fluid evolution?

Fluids are mostly released during prograde metamorphism and consumed during retrogression (e.g., Yardley, 1989); their composition typically evolves in response to mixed-volatile reactions that occur at increasing temperature and/or pressure

(Ague, 2014 and references therein; Penniston-Dorland, 2023). Understanding how fluids are produced and/or consumed in the deep crust, which is their composition and amount, and how they interact with the hosting rocks has important implications for our understanding of large-scale geochemical and geodynamic processes (Jamtveit and Austrheim, 2010; Manning, 2018; Manning and Frezzotti, 2020; Yardley, 2009; Yardley and Bodnar, 2014). The long-term (i.e., >1 Ma) global geochemical cycles (e.g., water and carbon cycles) are primarily controlled by the production of metamorphic fluids in different geodynamic settings and by their ability to migrate toward the surface (e.g., Berner et al., 1983; Groppo et al., 2022; Kerrick and Connolly, 2001b; Rüpke et al., 2004; Selverstone and Gutzler, 1993; Svensen et al., 2004; Svensen and Jamtveit, 2010). Fluids released during subduction are involved in the generation of arc-related magmas (e.g., Kerrick and Connolly, 2001a; Ulmer, 2001) and in the genesis of deep earthquakes (Hacker et al., 2003; Zhan, 2020). On the other hand, CO_2-bearing fluids are released during continent-continent collision and potentially represent major input to long-term atmospheric CO_2 (e.g., Becker et al., 2008; Gaillardet and Galy, 2008; Groppo et al., 2022; Kerrick and Caldeira, 1993; Selverstone and Gutzler, 1993); moreover, metamorphic fluids produced in orogenic settings also play a crucial role in the origin of ore deposits (e.g., Evans and Tomkins, 2020; Morissey and Tomkins, 2020; Tomkins, 2010; Yardley and Bodnar, 2014). Also, metamorphic devolatilization processes may affect the elastic properties of rocks (Boudier et al., 2010), with consequences for the interpretation of seismic data, and fluid-rock interactions during metamorphism can alter crustal rheology, ultimately influencing the development of collisional belts (Jackson et al., 2004).

Metamorphic fluids are relatively inaccessible, other than by study of fluid inclusions, these last providing the only direct information on fluids trapped during minerals' growth at different depths (e.g., Frezzotti and Ferrando, 2015; Yardley and Bodnar, 2014). Indirect approaches to investigate fluid evolution in metamorphic systems are mostly based on phase equilibrium modeling, which allows predicting the characteristics of fluids generated at variable pressure and temperature, as well as the processes that generate them. This section describes the main types of phase diagrams that can be used to characterize mixed-volatile fluids, and suggests a strategy for constraining fluid evolution in metamorphic systems, with emphasis on orogenic settings (i.e., medium- to high geothermal gradients). An internally buffered behavior is assumed, which implies that the fluid composition is controlled by the equilibrium mineral assemblage (i.e., it is not externally controlled). This assumption follows the approach of Greenwood (1975) and Baker et al. (1991) and is in agreement with extensive petrographic evidence (e.g., Connolly and Trommsdorff, 1991; Eberhard and Pettke, 2021; Groppo et al., 2017, 2021; Rapa et al., 2017). As a consequence of this assumption, the following discussion does not apply to open systems in which devolatilization reactions are driven by reactive fluid infiltration (e.g., Ague, 2000, 2003; Ague and Rye, 1999; Ferry, 1986, 1992; Ferry et al., 2013).

For the sake of simplicity, the following discussion is limited to the most common type of metamorphic COH fluids in orogenic settings (i.e., binary H_2O–CO_2 fluids), for which the X_{FLUID} variable can be defined in terms of molar fraction of CO_2 [$X(CO_2) = CO_2/(CO_2 + H_2O)$]. However, the same approach can be applied to investigate CH_4-bearing reductive fluids (e.g., in graphite-bearing metapelites): in this case, the X_{FLUID} variable is more conveniently described in terms of molar fraction of oxygen [$X(O) = O/(O + H)$] (Cesare, 1995; Connolly, 1995; Connolly and Cesare, 1993) (e.g., Chu and Ague, 2013), or in terms of C/H atomic ratio (e.g., Nabelek and Chen, 2014). Moreover, a classical molecular fluid model is considered in the following discussion, which is reliable at the medium- to high geothermal gradients typical of orogenic settings, but less reliable at low geothermal gradients typical of subduction settings (see section "Concluding remarks and perspectives").

Types of phase diagrams useful to investigate the fluid evolution

In metamorphic systems involving mixed-volatile fluids (e.g., COH fluids), the composition of the fluid (X_{FLUID}) is a further variable to be considered in addition to *P*, *T* and the composition of the system (X_{SYSTEM}) discussed in the previous section "Constraining the *P*–*T* conditions experienced by metamorphic rocks". Different types of phase diagrams can be used to investigate how the composition of the fluid changes as a function of the other variables (*P*, *T* and X_{SYSTEM}).

T–X_{FLUID} phase diagram sections

Isobaric *T*–$X(CO_2)$ phase diagram sections (and, less commonly, isothermal *P*–$X(CO_2)$ sections) have been applied since the pioneering works of Greenwood (1962, 1975), Hewitt (1973), Kerrick (1974) and Ferry (1976) for describing metamorphic systems characterized by mixed-volatile fluids; in this type of phase diagrams, the X_{FLUID} variable is made explicit on the horizontal axis, thus allowing a direct evaluation of the composition of the fluid along a specific equilibrium curve and at a given *T* (and *P*) condition. Generally, the influence of Fe-Mg substitution and the effects of minor system components on the stability of solid solutions is approximated by decreasing the end-members' activities in order to match the measured composition of the corresponding solid solutions. Calculation of *T*–$X(CO_2)$ phase diagram sections is relatively straightforward for chemically simple systems, such as the CMAS–H_2O–CO_2 (e.g., Castelli et al., 2007; Dey et al., 2019; Karmakar, 2021; Manzotti et al., 2021; Schmädicke et al., 2001), CFAS–H_2O–CO_2 (e.g., Dasgupta and Pal, 2005; Groppo et al., 2013a; Manzotti et al., 2021; Sengupta and Raith, 2002) and KCMAS–H_2O–CO_2 (e.g., Cartwright and Buick, 1995; Ferry, 1976; Hewitt, 1973; Kerrick, 1974) systems, but becomes quite complex as the number of thermodynamic components increases (e.g., NKCMAS–H_2O–CO_2 system: Groppo et al., 2017; NKCMAST–H_2O–CO_2 system: Rapa et al., 2017).

The main features of these phase diagrams (which are actually projections of a phase diagram section, as defined by Connolly and Trommsdorff, 1991) are univariant equilibria and invariant points (Fig. 15). As discussed in section "Projections," the composition of solution phases changes along univariant equilibria (e.g., garnet composition changes from $Grs_{<49}$ to $Grs_{>88}$ along the univariant reaction 11 in Fig. 15). This implies that the reaction coefficients of the phases involved in the univariant

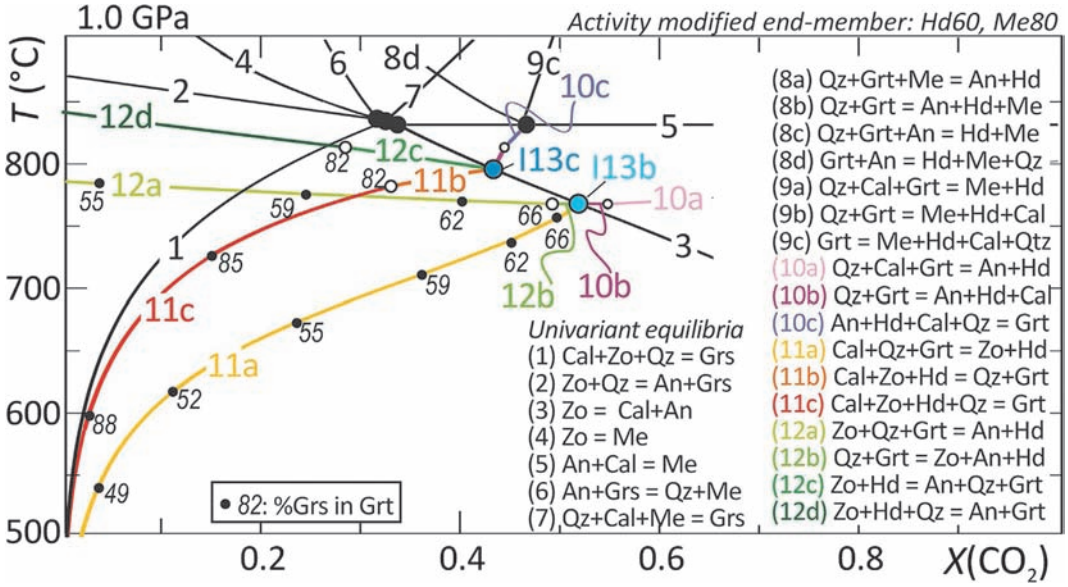

Fig. 15 Isobaric T–$X(CO_2)$ phase diagram section in the system CFAS–H_2O–CO_2 at 1.0 GPa, calculated for aHd = 0.6 and aMe = 0.8. Solid large points: invariant points; empty small points: singular points and singular compositions (% Grs, in italic); solid small points indicate the variation in garnet composition along the univariant curves (%Grs, in italic). Univariant reactions 1–7 are degenerate reactions in the CAS–H_2O–CO_2 system. Univariant reactions 8–12 have two or more singular points, and are therefore divided in three or more portions (colors help to recognize each of these portions). The invariant point I13 is duplicated (I13b and I13c); the two duplicated points I13b and I13c correspond to univariant equilibria in the correspondent mixed-volatile P–T projection of Fig. 16. All reaction equations are written such that the high-T assemblage is on the right side. Modified from Groppo C, Rolfo F, Castelli D, Connolly JAD (2013a) Metamorphic CO_2 production from calc-silicate rocks via garnet-forming reactions in the CFAS–H_2O–CO_2 system. *Contributions to Mineralogy and Petrology* **166**: 1655–1675, their Fig. 12.

reactions change continuously; it might be possible that, for certain solution compositions (i.e., singular compositions: Abart et al., 1992; Baker et al., 1991; Carmichael, 1991; Connolly and Trommsdorff, 1991; Robinson, 1991), the stoichiometric coefficient of one or more phase(s) vanishes, and that the sign of this coefficient changes on the two opposite sides of the reaction (e.g., reaction 11 in Fig. 15 has a singular point at Grs_{82}, at which the quartz coefficient becomes zero, so that quartz for $Grs_{<82}$ is a product of reaction 11b, whereas for $Grs_{>82}$ quartz is a reactant of reaction 11c). The occurrence of singular points is a peculiar feature of isobaric T–$X(CO_2)$ phase diagram sections involving one or more solid solutions (however, singularities also occur in systems involving a pure H_2O fluid; e.g., Worley and Powell, 1998). The consequence of this complexity is that at a specific P–T condition, the formation of a certain mineral may occur at the expense of a particular phase (e.g., garnet grows at the expense of quartz through reaction 11c in Fig. 15), while at another, it forms together with that phase (e.g., garnet grows together with quartz through reaction 11b in Fig. 15), resulting in two different microstructures (e.g., Groppo et al., 2013a; Robinson, 1991; Sengupta and Raith, 2002). Another peculiar feature of this type of diagrams is that the Clapeyron slopes of the reactions that involve solution phases significantly change as a function of P, T and $X(CO_2)$, so that they often have a loop (or horseshoe) shape (Fig. 15). This topological feature can duplicate invariant points at the two intersections of these loop-shaped univariant curves (e.g., invariant point I13 in Fig. 15, which results from the intersection of reaction 3 with the loop-shaped reactions 11 and 12, is duplicated as I13b and I13c).

Isobaric T–$X(CO_2)$ phase diagram sections have proven to be valuable for many geological applications, because they provide quantitative information on (1) the fluid composition at given P–T conditions, and on (2) the fluid producing processes, in terms of stoichiometrically balanced reactions. However, they also have some important limitations, summarized by Connolly and Trommsdorff (1991): (1) pressure (or temperature in P–$X(CO_2)$ diagrams) must be independently known, and (2) these diagrams only show fluid-saturated phase relations, but fluid may be absent at various stages of the metamorphic evolution. Moreover, although the activity-correction approach approximates to a certain extent the mineral compositions measured in a specific sample, (3) this type of phase diagram show phase relations for the general model system, rather than for a specific sample.

Mixed-volatile P–T *projections*

Mixed-volatile P–T projections are phase diagrams in which the fluid phase components are treated as true thermodynamic components (Connolly and Trommsdorff, 1991). The key features of mixed-volatile P–T projections are, once again, univariant curves and invariant points: differently from the T–$X(CO_2)$ grids, however, also the composition of the fluid (in addition to that of the solid solutions) continuously changes along the fluid-present univariant curves as a function of P and T (Fig. 16). Singular points, at which fluid attains a composition such that the stoichiometric coefficient of one phase vanishes (Abart et al., 1992; Baker et al., 1991; Carmichael, 1991; Connolly and Trommsdorff, 1991; Robinson, 1991), commonly occur along these univariant equilibria. The most striking feature of mixed-volatile P–T projections is that the variation in Clapeyron slopes, both along individual univariant curves and among different curves, is much stronger than in fixed fluid composition projections (Connolly and Trommsdorff, 1991) (Fig. 16). The projections are therefore useful as petrogenetic grids because the univariant curves dissect

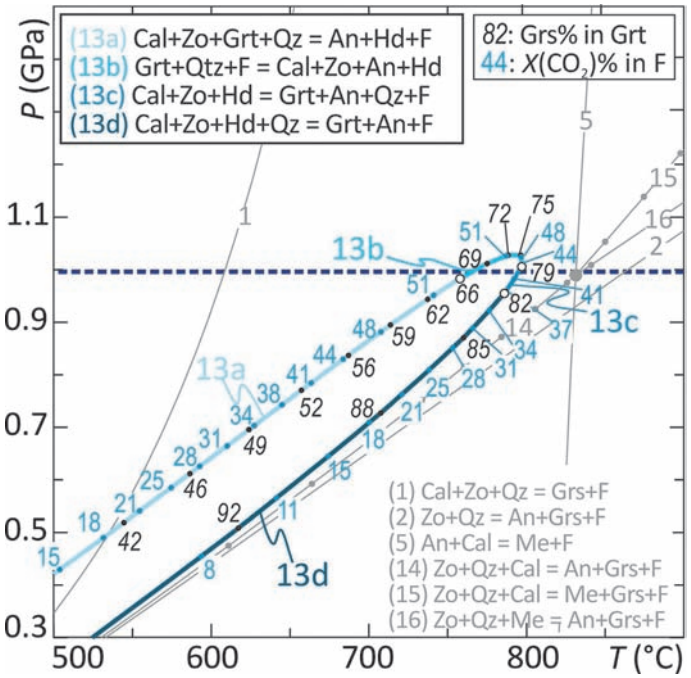

Fig. 16 Mixed-volatile *P–T* projection in the system CFAS–H_2O–CO_2 calculated for *a*Hed = 0.6 and *a*Me = 0.8. Grey lines: fluid-present degenerate CAS–H_2O–CO_2 univariant reactions. Reaction 13: fluid-present CFAS–H_2O–CO_2 univariant reaction with both fluid and garnet of variable compositions, corresponding to the duplicated invariant points I13b and I13c in Fig. 15. Solid large points: invariant points; empty small points: singular points; solid small points indicate the variation in garnet (black) and fluid (blue) compositions along the univariant curve. The univariant reaction 13 has three singular points, and is therefore divided in four portions (colors help to recognize each of these portions). The dashed blue line defines the pressure at which the isobaric *T–X*(CO_2) phase diagram section of Fig. 15 is calculated. All reaction equations are written such that the high-*T* assemblage is on the right side. Modified from Groppo C, Rolfo F, Castelli D, Connolly JAD (2013a) Metamorphic CO_2 production from calc-silicate rocks via garnet-forming reactions in the CFAS–H_2O–CO_2 system. *Contributions to Mineralogy and Petrology* **166**: 1655–1675, their Fig. 13.

the *P–T* space into relatively narrow regions (Castelli et al., 2007; Connolly and Trommsdorff, 1991; Groppo et al., 2007). Most of the compositional information shown in the *T–X*(CO_2) diagrams is retained in the mixed-volatile *P–T* projections. However, because in the *P–T* projections neither *P* nor *T* are fixed, the degrees of freedom (i.e., the variance) increase by one with respect to the *T–X*(CO_2) grids. This implies that fluid-present univariant curves in a mixed-volatile *P–T* projection coincide with invariant points in the correspondent isobaric *T–X*(CO_2) sections (or isothermal *P–X*(CO_2) sections) (Baker et al., 1991; Carmichael, 1991; Connolly and Trommsdorff, 1991).

Mixed-volatile *P–T* projections have been applied to investigate relatively simple chemical systems with fixed mineral compositions or involving few solid solutions, such as the CMS–H_2O–CO_2 (Baker et al., 1991; Skippen, 1971, 1974), CAS–H_2O–CO_2 (Bhowmik et al., 1995; Dasgupta, 1993; Fitzsimons and Harley, 1994; Harley and Buick, 1992; Mathavan and Fernando, 2001; Sengupta et al., 1997; Stephenson and Cook, 1997), CMAS–H_2O–CO_2 (Carmichael, 1991; Castelli et al., 2007; Connolly and Trommsdorff, 1991; Groppo et al., 2007; Schmädicke et al., 2001) and CFAS–H_2O–CO_2 (Groppo et al., 2013a) systems. Application of this approach to more complex systems which involve two or more solid solutions necessarily requires some simplifications to reduce the number of equilibria to be calculated to the most relevant ones (e.g., the effect of Mg-Fe substitution in mafic minerals is generally simulated using decreased activities for Mg- or Fe- end-members, matching the measured compositions). So far, systems with more than six components have been little investigated using the approach of mixed-volatile *P–T* projections (NCMAS–H_2O–CO_2 and KCMAS–H_2O–CO_2 systems: Omori et al., 1998; KCFMAS–H_2O–CO_2 system: Nabelek, 2002; NKCFMAST–H_2O–CO_2 system: Groppo et al., 2017; NKCFMAST–H_2O–CO_2 system: López Sánchez Vizcaíno et al., 1997; Rapa et al., 2017).

Being able to (1) predict the changes in both fluid and mineral compositions as a function of both *P* and *T* (for a closed system), and to (2) model both fluid-present and fluid-absent reactions, mixed-volatile *P–T* projections overcome most of the limitations of *T–X*(CO_2) phase diagram sections. The main limitations of mixed-volatile *P–T* projections are: (1) they are more complicated and difficult to interpret than *T–X*(CO_2) and *P–X*(CO_2) grids, and (2) their application to complex chemical systems is hampered by the overwhelming number of reaction curves projected on the *P–T* frame.

T–X_{FLUID} mineral assemblage diagrams

Isobaric *T–X*(CO_2) mineral assemblage diagrams allow modeling phase relations in fluid-saturated, mixed-volatile systems with a specific, fixed bulk composition. Pressure, or pressure as a function of temperature (i.e., a *P*/*T* gradient) can be alternatively used as y-axis variables, if the temperature or the prograde evolution of the investigated sample are independently known. As discussed in

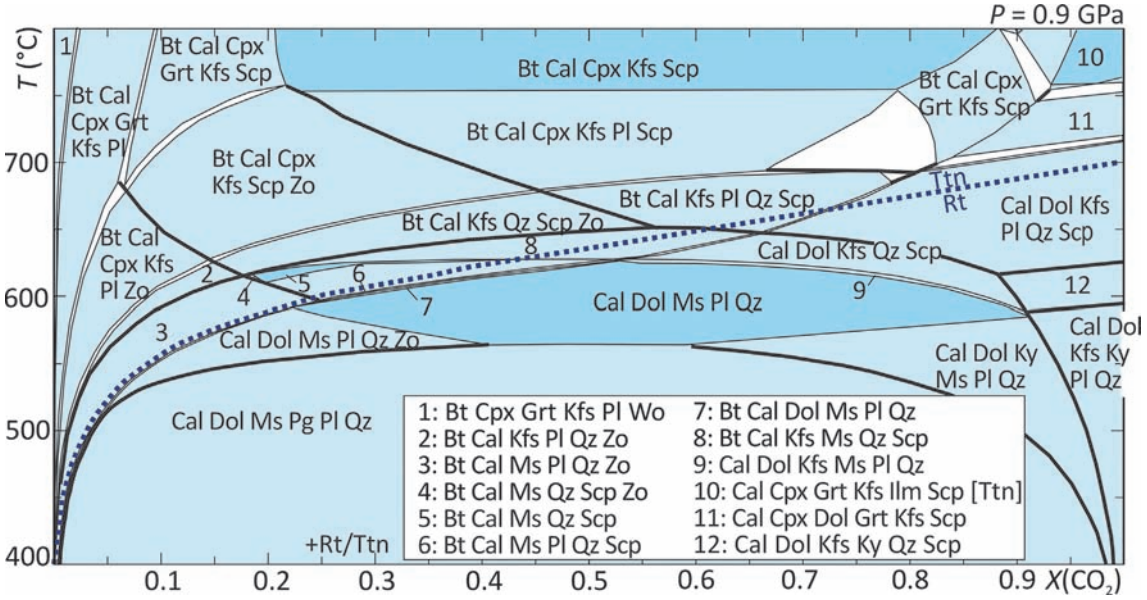

Fig. 17 *T–X*(CO_2) MAD calculated for a calc-silicate rock (sample 07-22, calcite-rich domain, in Groppo et al., 2017) in the system NKCMFAST–H_2O–CO_2 at a pressure of 0.9 GPa. White, light blue and dark blue fields are di-, tri- and quadrivalent fields, respectively; the thick black lines are univariant equilibria that do not involve femic minerals. The narrow, isobaric, divariant fields correspond to isobaric univariant reactions in the corresponding *T–X*(CO_2) phase diagram section calculated in the NKCMAST–H_2O–CO_2 system. Modified from Groppo C, Rolfo F, Castelli D, Mosca P (2017) Metamorphic CO_2 production in collisional orogens: Petrologic constraints from phase diagram modeling of Himalayan, scapolite-bearing, calc-silicate rocks in the NKC(F)MAS(T)-HC system. *Journal of Petrology* **58**: 53–84, their Fig. 8c.

section "Isochemical phase diagrams," key features of *T–X*(CO_2) isochemical phase diagrams are fields bounded by lines; each field represents a stable assemblage and the composition of the fluid in equilibrium with each assemblage can be directly read on the horizontal axis (Fig. 17).

T–X(CO_2) MADs and *T–X*(CO_2) grids are comparable to *P–T* isochemical phase diagrams and *P–T* projections (see section "Basic principles of forward thermodynamic modeling"), i.e., the isobaric *T–X*(CO_2) MAD allows recognition of which, among the equilibria predicted by the *T–X*(CO_2) grid, are effectively "seen" by the modeled sample for variable fluid compositions. Isobaric *T–X*(CO_2) isochemical phase diagrams can be easily calculated also for chemically complex systems, and thus permit a more reliable modeling of solution phases compared to activity-modified *T–X*(CO_2) grids. As a consequence of the increasing number of thermodynamic components considered in the calculation, *T–X*(CO_2) MADs are generally dominated by high-variance field assemblages, whereas narrow low-variance fields correspond to the univariant reactions in the correspondent *T–X*(CO_2) phase diagram sections (Fig. 17).

Examples of application of *T–X*(CO_2) or *P*/*T–X*(CO_2) isochemical phase diagrams for constraining the fluid evolution in carbonate-bearing systems are provided, among others, by Cottle et al. (2011), Kuhn et al. (2005), Groppo et al. (2017, 2021) and Rapa et al. (2017). Strengths and weaknesses of the *T–X*(CO_2) isochemical phase diagrams are similar to those discussed for the more common *P–T* MADs (see section "Isochemical phase diagrams"). When the main goal is the reconstruction of fluid evolution (e.g., for constraining mass balance models of volatiles), the main limitation of *T–X*(CO_2) MADs is their inability of characterizing in detail (e.g., stoichiometric balancing) the fluid-producing univariant reactions.

How to constrain fluid evolution

The different types of phase diagrams presented in the previous section "Types of phase diagrams useful to investigate the fluid evolution" provide the theoretical framework for investigating mixed-volatile systems. Using a single type of phase diagram is generally not sufficient to characterize fluid-producing reactions and to constrain its composition and amount; more often, all three types of diagrams are necessary, because each of them provide complementary information. Independent knowledge of the prograde evolution (or at least of the peak *P–T* conditions) experienced by the investigated sample is generally required: this can be best constrained based on associated lithologies in which the fluid phase can be approximated to pure H_2O. The best strategy for constraining fluid evolution in chemically complex systems should be based on: (1) a rigorous microstructural study, (2) a robust phase equilibrium modeling, and possibly (3) the validation of the results using one or more method(s) that do not rely on the assumption of chemical thermodynamics approach. This strategy is illustrated in the following using the case study presented by Rapa et al. (2017).

Interpretation of microstructures

A detailed microstructural study is the crucial starting point for any attempt to constrain the fluid evolution of a specific sample: it allows recognizing which minerals were consumed (i.e., the reactants) and which minerals were produced (i.e., the products) at different stages of the metamorphic evolution. The study of Rapa et al. (2017) focuses on a calcsilicate rock (sample 14-53c) from the Lower Greater Himalayan Sequence of central Nepal. The sample has a banded structure, with calcite-rich and calcite-poor domains defining a cm-thick layering. The mineral assemblage is the same in both domains (clinopyroxene + scapolite + K-feldspar + plagioclase + quartz ± calcite + titanite), but modal proportions are different, so that the two domains also have a different local bulk composition. The following key microstructures have been observed in both domains:

(a) Fine-grained polymineralic inclusions of amphibole + calcite + quartz ± biotite ± Na-rich plagioclase with corroded margins are preserved within coarse-grained clinopyroxene cores (Fig. 18a), suggesting that amphibole, calcite, quartz, biotite and Na-rich plagioclase all behaved as reactants during an early metamorphic stage, whereas clinopyroxene was a product. A Na-rich phase (e.g., scapolite) can be inferred among the products to accommodate Na released from plagioclase;
(b) monomineralic inclusions of quartz and scapolite with rounded margins are hosted within granoblastic K-feldspar and Ca-rich plagioclase in the matrix (Fig. 18b and c), and relict monomineralic inclusions of quartz, scapolite, calcite and biotite are preserved in clinopyroxene (Fig. 18d and e) and titanite (Fig. 18f). This implies that quartz, scapolite, calcite and biotite should have been the reactants of one or more reactions which produced the matrix assemblage consisting of K-feldspar, Ca-rich plagioclase, clinopyroxene and titanite.

Phase equilibrium modeling

Different types of phase diagrams have been used to interpret the observed microstructures and to constrain the P–T–X_{FLUID} evolution, each one useful to investigate different aspects of the fluid-producing history. Specifically: (a) P/T–$X(CO_2)$ isochemical phase diagrams calculated in the system NCKMFAST–H_2O–CO_2 allowed the recognition of which equilibria have been effectively "seen" by the studied sample; narrow divariant fields and short univariant lines modeled by the P/T–$X(CO_2)$ MADs, respectively correspond to univariant and invariant equilibria in the corresponding P/T–$X(CO_2)$ grids; (b) P/T–$X(CO_2)$ grids calculated in the system NCKMAST–H_2O–CO_2 (with activities of the Mg end-members decreased to match the measured compositions) allow to stoichiometrically balance the relevant fluid-producing univariant equilibria and to recognize the existence of singular points at which a reactant becomes a product or vice versa; (c) mixed-volatile P–T projections allow recognition of the crucial role of the invariant assemblages predicted by the P/T–$X(CO_2)$ grids.

Based on the results of phase equilibrium modeling, the following P–T–X_{FLUID} evolution was reconstructed (Fig. 19; see the original paper by Rapa et al., 2017 for all the details):

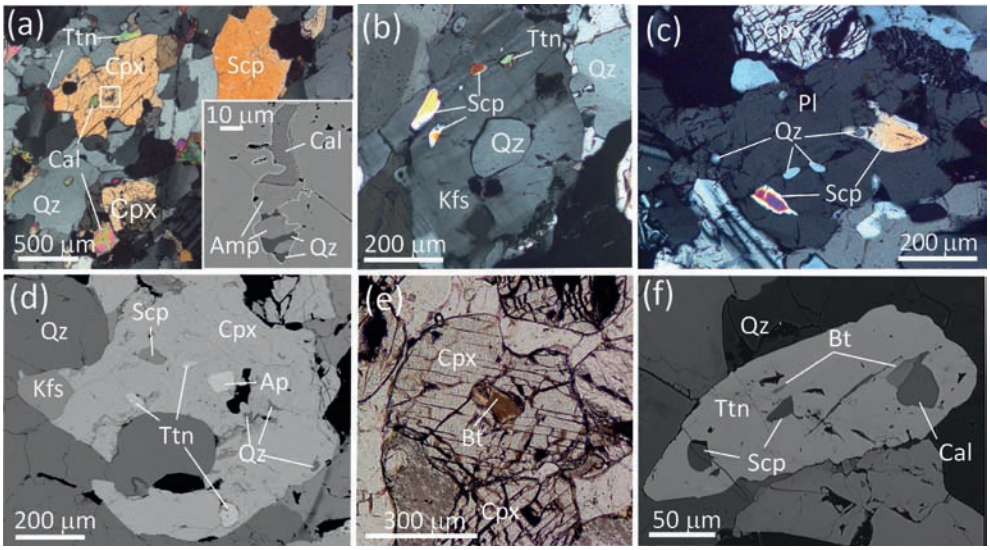

Fig. 18 Representative microstructures of sample 14-53c described in Rapa et al. (2017). (a) Clinopyroxene granoblast hosting in its core a polymineralic inclusion (amphibole + calcite + quartz) with corroded and lobated margins (XPL). (b) K-feldspar includes rounded quartz and scapolite crystals (XPL). (c) Plagioclase granoblast including monomineralic scapolite and quartz (XPL). (d) Clinopyroxene with monomineralic scapolite, titanite and quartz inclusions (BSE). (e) Rounded monomineralic biotite included in clinopyroxene (XPL). (f) Titanite includes scapolite, biotite and calcite (BSE). XPL: Crossed Polarized Light, BSE: Back Scattered Electron image. Modified from Rapa G, Groppo C, Rolfo F, Petrelli M, Mosca P, Perugini D (2017) Titanite-bearing calc-silicate rocks constrain timing, duration, and magnitude of metamorphic CO_2 degassing in the Himalayan belt. *Lithos* **292–293**: 364–378, their Figs. 3–5.

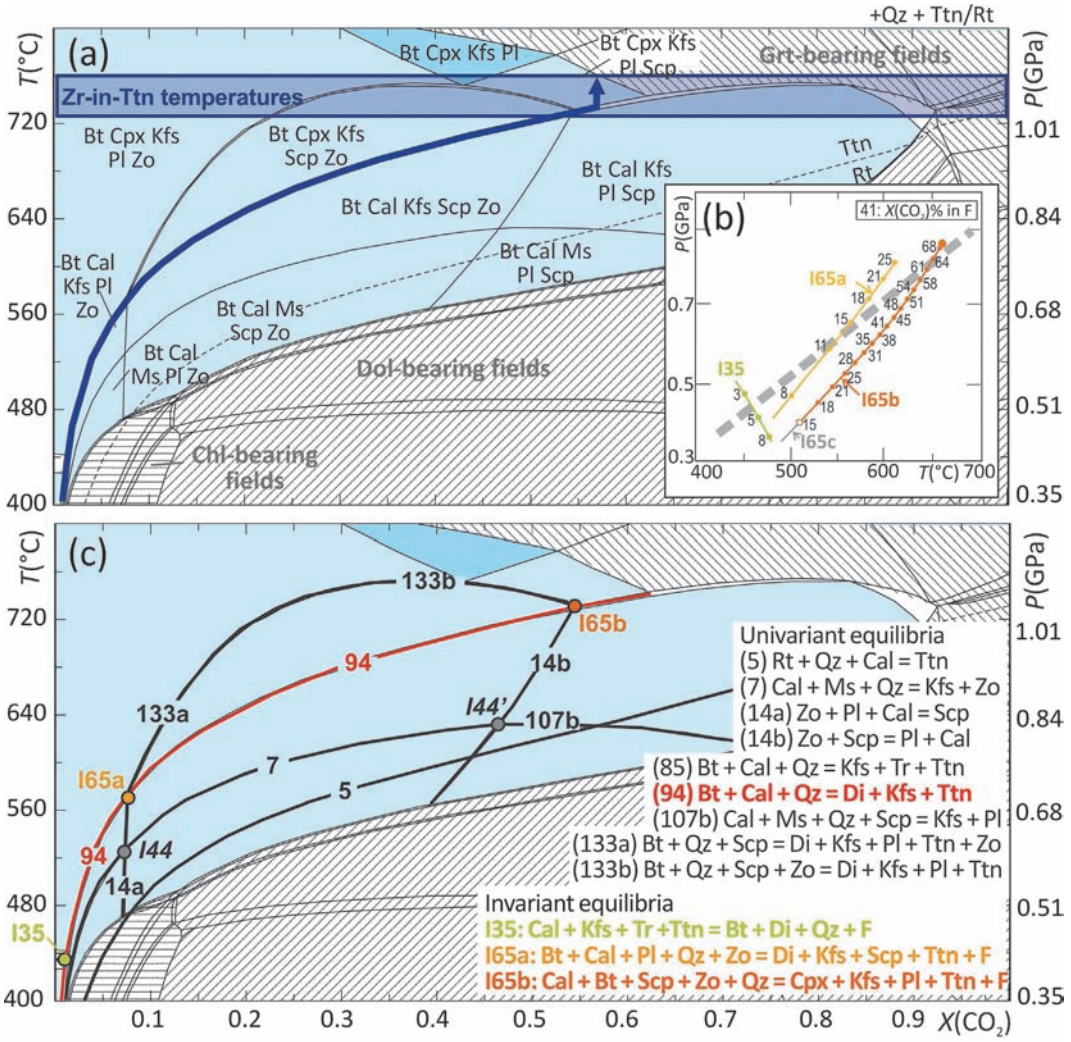

Fig. 19 (a) *P*/*T*–*X*(CO_2) MAD calculated for the Cal-poor domain of sample 14-53c (Rapa et al., 2017), in the system NCKMFAST–H_2O–CO_2 along a *P*/*T* gradient defined as *P*(bar) = 20.5 *T*(K)–10.294. White, light-blue and dark-blue fields are di-, tri- and quadri-variant fields, respectively; the narrow divariant fields correspond to the univariant reactions in the *P*/*T*–*X*(CO_2) phase diagram section. Dashed fields are dolomite, garnet-, and/or chlorite-bearing fields, not relevant for the studied sample. The thick blue arrow approximates the *P*/*T*–*X*(CO_2) internally buffered fluid evolution as constrained by the relevant microstructures. The blue box constrains the Zr-in-Ttn temperatures obtained from the analyzed titanite grains. (b) Mixed-volatile *P*–*T* projection in the system NCKMAST–H_2O–CO_2 calculated for *a*Tr = 0.7, *a*Di = 0.7, *a*Zo = 0.75, showing a selection of the univariant curves seen by the studied sample, corresponding to the isobaric/isothermal invariant points I35 and I65 (duplicated) in (c). Solid large points: invariant points; empty small points: singular points. The variations of fluid composition ($X(CO_2)$%) along each univariant curve is also reported (solid small points). The dashed thick grey line defines the *P*/*T* gradient along which the *P*/*T*–*X*(CO_2) MAD (a) is calculated. (c) Same *P*/*T*–*X*(CO_2) MAD as in (a): the univariant and invariant equilibria "seen" by the Cal-poor domain are outlined. The colored equilibria are discussed in the text. All reaction equations are written such that the high-*T* assemblage is on the right side. Note that the univariant curves and invariant points overlap the (narrow) divariant fields and (short) univariant lines of the MAD. Modified from Rapa G, Groppo C, Rolfo F, Petrelli M, Mosca P, Perugini D (2017) Titanite-bearing calc-silicate rocks constrain timing, duration, and magnitude of metamorphic CO_2 degassing in the Himalayan belt. *Lithos* **292–293**: 364–378.

- microstructures (a) are compatible with the univariant reaction 94 (Bt + Cal + Qz = Di + Kfs + Ttn + F) and the invariant equilibria I35 (Cal + Kfs + Tr + Ttn = Bt + Di + Qz + F; univariant reaction I35 in the mixed-volatile *P*–*T* projection) and I65a (Bt + Cal + Pl + Qz + Zo = Di + Kfs + Scp + Ttn + F; univariant reaction I65a in the mixed-volatile *P*–*T* projection);
- microstructures (b) suggest that the system reached the invariant point I65b (Cal + Bt + Scp + Zo + Qz = Cpx + Kfs + Pl + Ttn + F; univariant reaction I65b in the mixed-volatile *P*–*T* projection) evolving along the univariant equilibrium 94.

It has been demonstrated that, as long as a system remains internally buffered, sudden and volumetrically significant appearance of new phases and the simultaneous disappearance of previously abundant phases occur at the isobaric/isothermal invariant points, whereas modal changes are only minor along the univariant curves (e.g., Greenwood, 1975; Groppo et al., 2017). In contrast,

univariant reactions lead to volumetrically-significant appearance of new phases when the buffering ability of the system ceases due to the complete consumption of one or more reactants. The P–T–$X(CO_2)$ evolution predicted by Rapa et al. (2017) for the studied sample (blue arrow in Fig. 19a) suggests that the system remained internally buffered up to ca. 740 °C, i.e., up to temperatures slightly higher than the invariant point I65b. At $T > 740$ °C, the buffering ability of the system ceased due to the complete consumption of calcite. It follows that the most important episodes of mineral growth/consumption and of fluid production occurred at the invariant points I35 (early prograde stage), I65a (late prograde stage) and I65b (near-peak stage), and at $T > 740$ °C once that calcite was completely consumed (peak stage).

Thus, phase equilibrium modeling ultimately allowed: (1) understanding that fluid was mostly produced in pulses (i.e., through nearly discontinuous reactions operating in narrow P–T intervals), and (2) constraining the amounts of CO_2 released during these pulses, with implications for the estimate of the metamorphic CO_2 degassing from collisional orogens. It is worth noting that neither P/T–$X(CO_2)$ MADs nor P/T–$X(CO_2)$ grids alone can provide all the information (i.e., which are the univariant equilibria relevant for the studied sample, and the stoichiometric balancing of the CO_2-producing reactions) that are fundamental for a quantitative, rather than qualitative, study of fluid producing processes in mixed-volatile systems.

Validation of the results using an independent approach

The Zr-in-titanite trace element thermometer (see section "Trace element thermometry") was applied on 25 titanite grains from sample 14-53c, using the calibration of Hayden et al. (2008). Pressure was set to 1.00–1.05 GPa, basing on the results of the isochemical phase diagram modeling (Fig. 19a). An $a(\alpha\text{-Qz}) = 1$ was assumed because quartz is abundant in the sample. On the opposite, rutile is absent, therefore TiO_2 is under-saturated. $a(Rt) = 0.60$ and $a(Rt) = 0.55$ were estimated for the Cal-poor and Cal-rich domains respectively, following Ashley and Law (2015). The Zr content in the analyzed titanite grains is relatively high, spanning between 114 and 237 ppm, corresponding to Zr-in-Ttn temperatures of 729–764 °C (±15 °C). The frequency distribution of Zr-in-Ttn temperatures shows two main peaks at 731–735 °C and 741–750 °C, suggesting the existence of two different titanite populations crystallized at 730–740 °C and at 740–765 °C, respectively. These results are consistent with those of the phase equilibrium modeling, that predict growth of titanite at the near-peak and peak stages through equilibria I65b and 94, respectively. The lack of titanite grains preserving Zr-temperatures of ca. 570 °C (i.e., late prograde stage, equilibrium I65a) was interpreted by Rapa et al. (2017) as due to the complete re-equilibration/re-crystallization of the prograde generation of titanite during the near-peak and/or peak events.

Concluding remarks and perspectives

This review summarizes the different strategies commonly used for retrieving quantitative physical and chemical information from metamorphic rocks, which is crucial for our understanding of the geodynamic processes governing the Earth's evolution through time. Strengths and weaknesses outlined for each method show that there is not a panacea to solve all petrological problems. Rather, the best strategy is usually to combine two or more independent methods. Some methods are currently more fashionable than others, because they are faster, simpler, cheaper and/or more effective in providing reliable quantitative results. However, the metamorphosis of metamorphic petrology (Spear et al., 2016) is still in progress; further improvements of most of these methods are therefore expected, as well as the development of new strategies which are still poorly explored or even not conceived yet.

Promising challenges for future research in this field concern:

(1) Trace element thermometry—The popularity of trace element thermometry has progressively increased in the last 15 years (Cruz-Uribe et al., 2018), leading to its widespread application on natural samples from a large variety of geodynamic settings. On one hand, recent studies have demonstrated a great consistency between the results of trace element thermometry and those obtained from independent calculations (e.g., MAD modeling; Kohn, 2020). On the other hand, however, examples of applications returning P–T estimates that are not in agreement with other thermobarometric approaches have been reported (e.g., Kendrick and Indares, 2018). The causes of these discrepancies can be related to calibration issues and/or to the still incomplete knowledge of the trace elements solubility behavior. New experiments conducted over wider temperature and pressure ranges might be useful to improve the reliability of these geothermometers (e.g., Osborne et al., 2022). Also, further studies on complex natural systems will help clarifying to what extent accessory phase equilibrium and trace element equilibrium are attained in metamorphic rocks. In the future, it is likely that trace element thermometers currently calibrated for very specific systems (e.g., the REE-in-two-pyroxene thermometer; Liang et al., 2013) could be extended to a larger variety of metamorphic systems. It is even possible that new trace element thermometers will be calibrated, based on natural observations confirmed by experimental data (e.g., Ti-in-kyanite: Müller et al., 2016).

(2) Spectroscopic thermobarometry—Spectroscopic thermobarometry is now in its early stage of development and significant advances in its application are expected in the near future (see review of Kohn et al., 2023). Elastic thermobarometry can be especially extended to new host-inclusion systems, through the progressive improvements of our knowledge on the thermo-elastic properties of minerals, including those with anisotropic behavior (e.g., quartz-in-zircon; Gonzalez et al., 2021).

(3) Forward modeling involving accessory minerals—The forward modeling approach is constantly evolving through the continuous updating of thermodynamic databases and the progressive improvement of solid solution models, extended to increasingly complex systems. In this framework, an interesting challenge for the future is testing the reliability of thermodynamic

parameters and solid solution models for accessory minerals (e.g., zircon: Kelsey and Powell, 2011; Yakymchuk and Brown, 2014; monazite: Hoschek, 2016; Janots et al., 2007; Spear and Pyle, 2010; allanite: Spear, 2010; phosphates: Shrestha et al., 2019), including the possibility of reproducing their trace element compositions (e.g., Johnson et al., 2021; Spear and Pyle, 2010; Yakymchuk et al., 2018). As a very important consequence, this would allow linking the age data obtained from the accessory minerals directly to the *P–T* path constrained through forward modeling, making petrochronology more robust and reliable (e.g., Engi, 2017; Kohn and Kelly, 2018; Yakymchuk et al., 2017).

(4) Iterative thermodynamic modeling—A new generation of hybrid thermodynamic modeling has been recently developed which combines the advantages of both forward and inverse thermobarometry methods (Duesterhoeft and Lanari, 2020; Lanari and Duesterhoeft, 2019; Lanari and Hermann, 2021). This strategy allows defining optimal *P–T–*(*X*) conditions using an iterative method applied on local bulk rock compositions (i.e., composition of selected domains of a given sample). This method currently represents the cutting-edge of thermobarometric approaches and has the potential to become rapidly popular among the metamorphic petrology community.

(5) Interplay between equilibrium and kinetics—The reliability of thermobarometric methods based on equilibrium thermodynamics has been recently questioned by a number of studies validated by the results of spectroscopic thermobarometry, which demonstrate that garnet nucleation can be significantly influenced by kinetic factors, resulting in a delay of garnet appearance with respect to the equilibrium predictions (e.g., Carlson et al., 2015; Castro and Spear, 2016; Pattison et al., 2011; Pattison and Tinkham, 2009; Spear et al., 2014; Waters and Lovegrove, 2002). The degree of overstepping of garnet nucleation can be extremely variable and the factors controlling it are still unclear. Kinetics also controls the metastable persistence of mineral phases outside their equilibrium stability fields, with potential important consequences for the application of equilibrium-based thermobarometers (e.g., Lanari and Hermann, 2021). Further investigation of the complex interplay between equilibrium and kinetics and of its petrologic implications is a promising line of research for the near future (e.g., Nagurney et al., 2021; (Nerone et al., 2023)Spear and Wolfe, 2019; Tamang et al., 2023).

(6) Fluid saturated vs. fluid under-saturated conditions—The common assumption that prograde metamorphism occurs at fluid-saturated conditions was already questioned by Thompson (1983) nearly 40 years ago. Guiraud et al. (2001) provided the theoretical basis for understanding whether fluid under-saturated conditions have been attained along a portion of the *P–T* path and discussed the implications for the preservation of mineral assemblages. Natural evidence supports the idea that even highly hydrated prograde assemblages (e.g., lawsonite-bearing) can develop under H_2O-undersaturated conditions (e.g., Ballevre et al., 2003; Lopez-Carmona et al., 2013; Groppo et al., 2016). Fluid under-saturated conditions are likely to prevail during exhumation coupled with cooling (e.g., Manzotti et al., 2018), although the fluid saturation behavior can be more complex when decompression is associated with heating (e.g., Cruciani et al., 2012; Groppo et al., 2015). Moreover, recent studies suggest that H_2O under-saturated conditions can be transiently reached also in shear zones (Ceccato et al., 2020; Tursi et al., 2021; Tursi, 2022), typically considered as preferential pathways for fluids. A systematic investigation of the frequency with which fluid under-saturated conditions occur during metamorphism, however, is still missing. Further studies in this direction are therefore desirable, which should be strictly connected to the investigation of the interplay between equilibrium and kinetics, because the presence and abundance of the fluid phase represent critical factors that influence the kinetics of the reactions.

(7) Electrolytic fluid thermodynamics—Recent studies demonstrated that the classic molecular fluid model fails in reproducing the characteristic of the fluids generated by progressive rock dissolution during subduction (Ferrando et al., 2017); electrolytic fluid thermodynamics (Galvez et al., 2015) is instead required to model such solute-bearing aqueous fluids. The implementation of electrolytic fluid models in Gibbs energy minimization procedures (Connolly and Galvez, 2018; Maffeis et al., 2021) is still at an embryonic stage, and represents a promising step forward for future studies. In this framework, the production of internally consistent thermodynamic dataset for aqueous species in complex systems (e.g., Miron et al., 2016, 2017), and the incorporation of additional components, such as sulfur (e.g., Evans et al., 2010; Evans and Powell, 2015), represents a further challenge for a more reliable modeling of fluid-rock interaction processes in natural systems.

(8) Modeling fluid-rock interaction processes and implications for the formation of ore deposits—In the last decades, the search for supply of critical metals (e.g., Li, Sc, V, Cr, Co, Ni, Ga, Ge, Nb, REE, graphite) has become a major focus of most governments, due to the need of these materials for renewable energy technologies and high-tech applications. Critical metals ore deposits are typical examples of open systems (e.g., Yardley and Bodnar, 2014), whose formation is strictly related to fluid-rock interaction. Constraining the genetic mechanisms leading to the formation of critical metal enrichments in different geodynamic settings thus implies understanding: (i) the physico-chemical features of metamorphic fluids, and (ii) to what extent fluids interact with the host rocks at depth. While the strategy described in Section "Constraining fluid evolution" allows investigating the fluid production and evolution in metamorphic systems hosting ore deposits (e.g., Elmer et al., 2007, 2008; Phillips and Powell, 2010), fluid-rock interaction processes are more difficult to assess. In this framework, the recently developed PTLoop tool (Vho et al., 2020) provides an exciting promise for the investigation of fluid-rock interactions in open-systems. PTLoop combines equilibrium thermodynamics and oxygen isotope fractionation modeling (Vho et al., 2019) to predict the variation in mineral assemblages, bulk and mineral oxygen isotope compositions, as well as the amount and oxygen isotope composition of the fluid released along a specified *P–T* path. This approach allows estimation of the extent of fluid-rock interaction during metamorphism, and understanding of how fluids migrate at depth (i.e., porous vs. channeled fluid flow), with important implication for the modeling of metallogenic processes. A further application might concern the investigation of the feedback between fluid production/mobility within the crust and earthquake nucleation (Vho et al., 2020).

Acknowledgments

This contribution presents a personal view of the strengths and weaknesses of each method, which might not be fully accepted by others. I would like to thank my mentors, Roberto Compagnoni and Daniele Castelli, to whom I am in debt for all my knowledge about metamorphic petrology and phase equilibrium modeling. Special thanks are due to Matt Kohn for the invitation to contribute to this volume and for his insightful comments, and to Franco Rolfo, for having convinced me to accept this task and for having critically read a preliminary version of the chapter. Pierre Lanari and Chris Yakymchuk are warmly thanked for their inspiring reviews which have contributed to significantly improve this chapter.

References

Abart R, Connolly JAD, and Trommsdorff V (1992) Singular point analysis: Construction of Schreinemakers projections for systems with a binary solution. *American Journal of Science* 292: 778–805.

Ague JJ (2000) Release of CO_2 from carbonate rocks during regional metamorphism of lithologically heterogeneous crust. *Geology* 28: 1123–1126.

Ague JJ (2003) Fluid infiltration and transport of major, minor, and trace elements during regional metamorphism of carbonate rocks, Wepawaug schist, Connecticut, USA. *American Journal of Science* 303: 753–816.

Ague JJ (2014) Fluid flow in the deep crust. In: Turekian K and Holland H (eds.) *Treatise on Geochemistry*, 2nd edn, vol. 4, pp. 203–247.

Ague JJ and Rye DM (1999) Simple models of CO_2 release from metacarbonates with implications for interpretation of directions and magnitudes of fluid flow in the deep crust. *Journal of Petrology* 40: 1443–1462.

Alvaro M, Mazzucchelli ML, Angel RJ, Murri M, Campomenosi N, Scambelluri M, Nestola F, Korsakov A, Tomilenko AA, Marone F, and Morana M (2020) Fossil subduction recorded by quartz from the coesite stability field. *Geology* 48: 24–28.

Anderson GM (2005) *Thermodynamics of Natural Systems*. Cambridge: Cambridge University Press.

Angel RJ, Mazzucchelli ML, Alvaro M, Nimis P, and Nestola F (2014) Geobarometry from host-inclusion systems: The role of elastic relaxation. *American Mineralogist* 99: 2146–2149.

Angel RJ, Nimis P, Mazzucchelli ML, Alvaro M, and Nestola F (2015) How large are departures from lithostatic pressure? Constraints from host-inclusion elasticity. *Journal of Metamorphic Geology* 33: 801–813.

Angel RJ, Mazzucchelli ML, Alvaro M, and Nestola F (2017) EosFit-Pinc: A simple GUI for host-inclusion elastic thermobarometry. *American Mineralogist* 102: 1957–1960.

Angel RJ, Murri M, Mihailova B, and Alvaro M (2019) Stress, strain and Raman shifts. *Zeitschrift für Kristallographie – Crystalline Materials* 234: 129–140.

Anovitz LM and Essene EJ (1987) Phase equilibria in the system $CaCO_3$-$MgCO_3$-$FeCO_3$. *Journal of Petrology* 28: 389–415.

Aoya M, Kouketsu Y, Endo S, Shimizu H, Mizukami T, Nakamura D, and Wallis S (2010) Extending the applicability of the Raman carbonaceous-material geothermometer using data from contact metamorphic rocks. *Journal of Metamorphic Geology* 28: 895–914.

Ashley KT and Law RD (2015) Modeling prograde TiO_2 activity and its significance for Ti-in-quartz thermobarometry of pelitic metamorphic rocks. *Contributions to Mineralogy and Petrology* 169: 23.

Ashley KT, Caddick MJ, Steele-MacInnis MJ, Bodnar RJ, and Dragovic B (2014) Geothermobarometric history of subduction recorded by quartz inclusions in garnet. *Geochemistry, Geophysics, Geosystems* 15. https://doi.org/10.1002/2013GC005106.

Baker J, Holland TJB, and Powell R (1991) Isograds in internally buffered systems without solid solutions: Principles and examples. *Contributions to Mineralogy and Petrology* 106: 170–182.

Ballevre M, Pitra P, and Bohn M (2003) Lawsonite growth in the epidote blueschists from the Ile de Groix (Armorican Massif, France): A potential geobarometer. *Journal of Metamorphic Geology* 21: 723–735.

Bartoli O (2017) Phase equilibria modelling of residual migmatites and granulites: An evaluation of the melt-reintegration approach. *Journal of Metamorphic Geology* 35: 919–942.

Becker JA, Bickle MJ, Galy A, and Holland TJB (2008) Himalayanmetamorphic CO_2 fluxes: Quantitative constraints from hydrothermal springs. *Earth and Planetary Science Letters* 265: 616–629.

Berman RG (1988) Internally consistent thermodynamic data for minerals in the system Na_2O–K_2O–CaO–MgO–FeO–Fe_2O_3–Al_2O_3–SiO_2–TiO_2–H_2O–CO_2. *Journal of Petrology* 29: 445–522.

Berman RG (1991) Thermobarometry using multiequilibrium calculations: A new technique, with petrological applications. *The Canadian Mineralogist* 29: 833–855.

Berman RG (2007) *winTWQ (version 2.3): A software package for performing internally-consistent thermobarometric calculations*. Geological Survey of Canada, Open file Report 5462, pp. 41.

Berman RG and Aranovich LY (1996) Optimized standard state and mixing properties of minerals: I. Model calibration for olivine, orthopyroxene, cordierite, garnet, and ilmenite in the system FeO–MgO–CaO–Al_2O_3–SiO_2–TiO_2. *Contributions to Mineralogy and Petrology* 126: 1–24.

Berman RG, Engi M, Greenwood HJ, and Brown TH (1986) Derivation of internally-consistent thermodynamic data by the technique of mathematical programming: A review with application to the system MgO–SiO_2–H_2O. *Journal of Petrology* 27: 1331–1364.

Berner RA, Lasaga AC, and Garrels RM (1983) The carbonate-silicate geochemical cycle and its effect on atmospheric carbon dioxide over the past 100 million years. *American Journal of Science* 283: 641–683.

Beyssac O, Goffe B, Chopin C, and Rouzaud JN (2002a) Raman spectra of carbonaceous material in metasediments: A new geothermometer. *Journal of Metamorphic Geology* 20: 859–871.

Beyssac O, Rouzaud JN, Goffé B, Brunet F, and Chopin C (2002b) Graphitization in a high-pressure, low-temperature metamorphic gradient: A Raman microspectroscopy and HRTEM study. *Contributions to Mineralogy and Petrology* 143: 19–31.

Beyssac O, Pattison DR, and Bourdelle F (2019) Contrasting degrees of recrystallization of carbonaceous material in the Nelson aureole, British Columbia and Ballachulish aureole, Scotland, with implications for thermometry based on Raman spectroscopy of carbonaceous material. *Journal of Metamorphic Geology* 37: 71–95.

Bhowmik SK, Dasgupta S, Hoernes S, and Bhattacharya PK (1995) Extremely high-temperature calcareous granulites from the Eastern Ghats, India: Evidence for isobaric cooling, fluid buffering, and terminal channelized fluid flow. *European Journal of Mineralogy* 7: 689–703.

Boudier F, Baronnet A, and Mainprice D (2010) Serpentine mineral replacements of natural olivine and their seismic implications: Oceanic lizardite versus subduction-related antigorite. *Journal of Petrology* 51: 495–512.

Bucher K and Grapes R (2011) *Petrogenesis of Metamorphic Rocks*, 8th edn. Berlin, Heidelberg: Springer-Verlag.

Caddick MJ and Thompson AB (2008) Quantifying the tectono-metamorphic evolution of politic rocks from a wide range of tectonic settings: Mineral compositions in equilibrium. *Contributions to Mineralogy and Petrology* 156: 177–195.

Caddick MJ, Bickle MJ, Harris NBW, Holland TJB, Horstwood MSA, Parrish RR, and Ahmad T (2007) Burial and exhumation history of a Lesser Himalayan schist: Recording the formation of an inverted metamorphic sequence in NW India. *Earth and Planetary Science Letters* 264: 375–390.

Campomenosi N, Mazzucchelli ML, Mihailova B, Scambelluri M, Angel RJ, Nestola F, Reali A, and Alvaro M (2018) How geometry and anisotropy affect residual strain in host inclusion system: Coupling experimental and numerical approaches. *American Mineralogist* 103: 2032–2035.

Carlson WD (2002) Scales of disequilibrium and rates of equilibration during metamorphism. *American Mineralogist* 87: 185–204.
Carlson WD, Pattison DRM, and Caddick MJ (2015) Beyond the equilibrium paradigm: How consideration of kinetics enhances metamorphic interpretation. *American Mineralogist* 100: 1659–1667.
Carmichael DM (1991) Univariant mixed-volatile reactions: Pressure–temperature phase diagrams and reaction isograds. *The Canadian Mineralogist* 29: 741–754.
Cartwright I and Buick IS (1995) Formation of wollastonite bearing marbles during late-regional metamorphic channeled fluid flow in the Upper Calc-silicate Unit, Reynolds Range Group, central Australia. *Journal of Metamorphic Geology* 13: 397–418.
Castelli D, Rolfo F, Groppo C, and Compagnoni R (2007) Impure marbles from the UHP Brossasco–Isasca Unit (Dora–Maira Massif, western Alps): Evidence for Alpine equilibration in the diamond stability field and evaluation of the X(CO_2) fluid evolution. *Journal of Metamorphic Geology* 25: 587–603.
Castro AE and Spear FS (2016) Reaction overstepping and re-evaluation of peak P-T conditions of the blueschist unit Sifnos, Greece: Implications for the Cyclades subduction zone. *International Geology Review* 59: 548–562.
Ceccato A, Goncalves P, and Pennacchioni G (2020) Temperature, fluid content and rheology of localized ductile shear zones in subsolidus cooling plutons. *Journal of Metamorphic Geology* 38: 881–903.
Cesare B (1995) Graphite precipitation in C–O–H fluid inclusions: Closed system compositional and density changes, and thermobarometric implications. *Contributions to Mineralogy and Petrology* 122: 25–33.
Cesare B, Parisatto M, Mancini L, Peruzzo L, Franceschi M, Tacchetto T, Reddy S, Spiess R, Nestola F, and Marone F (2021) Mineral inclusions are not immutable: Evidence of post-entrapment thermally-induced shape change of quartz in garnet. *Earth and Planetary Science Letters* 555: 116708.
Chacko T, Cole DR, and Horita J (2001) Equilibrium oxygen, hydrogen and carbon isotope fractionation factors applicable to geologic systems. In: Valley JW and Cole DR (eds.) *Stable Isotope Geochemistry: Reviews in Mineralogy. Mineralogical Society of America*, vol. 43, pp. 1–81. Washington, DC.
Chambers JA and Kohn MJ (2012) Titanium in muscovite, biotite, and hornblende: Modeling, thermometry, and rutile activities of metapelites and amphibolites. *American Mineralogist* 97: 543–555.
Chatterjee ND and Froese E (1975) A thermodynamic study of the pseudobinary join muscovite-paragonite in the system $KAlSi_3O_8$-$NaAlSi_3O_8$-Al_2O_3-SiO_2-H_2O. *American Mineralogist* 60: 985–993.
Chu X and Ague JJ (2013) Phase equilibria for graphitic metapelite including solution of CO_2 in melt and cordierite: Implications for dehydration, partial melting and graphite precipitation. *Journal of Metamorphic Geology* 31: 843–862.
Clayton RN and Kieffer SW (1991) Oxygen isotopic thermometer calibrations. In: Taylor HP, O'Neil JR, and Kaplan IR (eds.) *Stable Isotope Geochemistry: A Tribute to Samuel Epstein. Geochemical Society Special Publications 3*, pp. 3–10.
Connolly JAD (1990) Multivariate phase diagrams: An algorithm based on generalized thermodynamics. *American Journal of Science* 290: 666–718.
Connolly JAD (1995) Phase diagram methods for graphitic rocks and application to the system C–O–H–FeO–TiO_2–SiO_2. *Contributions to Mineralogy and Petrology* 119: 94–116.
Connolly JAD (2005) Computation of phase equilibria by linear programming: A tool for geodynamic modeling and its application to subduction zone decarbonation. *Earth and Planetary Science Letters* 236: 524–541.
Connolly JAD (2009) The geodynamic equation of state: What and how. *Geochemistry, Geophysics, Geosystems* 10: 1–19.
Connolly JAD and Cesare B (1993) C–O–H–S fluid compositions and oxygen fugacity in graphitic metapelites. *Journal of Metamorphic Geology* 11: 379–388.
Connolly JA and Galvez ME (2018) Electrolytic fluid speciation by Gibbs energy minimisation and implications for subduction zone mass transfer. *Earth and Planetary Science Letters* 501: 90–102.
Connolly JAD and Kerrick DM (1987) An algorithm and computer program for calculating composition phase diagrams. *Calphad* 11: 1–55.
Connolly JAD and Trommsdorff V (1991) Petrogenetic grids for metacarbonate rocks: Pressure–temperature phase diagrams for mixed-volatile systems. *Contributions to Mineralogy and Petrology* 108: 93–105.
Cottle JM, Waters DJ, Riley D, Beyssac O, and Jessup MJ (2011) Metamorphic history of the South Tibetan Detachment System, Mt. Everest region, revealed by RSCM thermometry and phase equilibria modelling. *Journal of Metamorphic Geology* 29: 561–582.
Cruciani G, Franceschelli M, Groppo C, and Spano ME (2012) Metamorphic evolution of non-equilibrated granulitized eclogite from Punta de li Tulchi (Variscan Sardinia) determined through texturally controlled thermodynamic modeling. *Journal of Metamorphic Geology* 30: 667–685.
Cruz-Uribe AM, Feineman MD, Zack T, and Jacob DE (2018) Assessing trace element (dis)equilibrium and the application of single element thermometers in metamorphic rocks. *Lithos* 314–315: 1–15.
Dasgupta D (1993) Contrasting mineral parageneses in high temperature calc-silicate granulites: Example from the Eastern Ghats, India. *Journal of Metamorphic Geology* 11: 193–202.
Dasgupta S and Pal S (2005) Origin of grandite garnet in calc-silicate granulites: Mineral–fluid equilibria and petrogenetic grids. *Journal of Petrology* 46: 1045–1076.
Dasgupta S, Chakraborty S, and Neogi S (2009) Petrology of an inverted barrovian sequence of metapelites in Sikkim Himalaya, India: Constraints on the tectonics of inversion. *American Journal of Science* 309: 43–84.
de Capitani C and Brown TH (1987) The computation of chemical equilibrium in complex systems containing non-ideal solutions. *Geochimica et Cosmochimica Acta* 51: 2639–2652.
de Capitani C and Petrakakis K (2010) The computation of equilibrium assemblage diagrams with Theriak/Domino software. *American Mineralogist* 95: 1006–1016.
Dey A, Choudhury SR, Mukherjee S, Sanyal S, and Sengupta P (2019) Origin of vesuvianite-garnet veins in calc-silicate rocks from part of the Chotanagpur Granite Gneiss Complex, East Indian Shield: The quantitative P-T-XCO_2 topology in parts of the system CaO-MgO-Al_2O_3-SiO_2-H_2O-CO_2 (+Fe_2O_3,F). *American Mineralogist* 104: 744–760.
Diener JFA, White RW, and Hudson TJM (2014) Melt production, redistribution and accumulation in mid-crustal source rocks, with implications for crustal-scale melt transfer. *Lithos* 200–201: 212–225.
Duesterhoeft E and Lanari P (2020) Iterative thermodynamic modelling—Part 1: A theoretical scoring technique and a computer program (Bingo-Antidote). *Journal of Metamorphic Geology* 38: 527–551.
Eberhard L and Pettke T (2021) Antigorite dehydration fluids boost carbonate mobilization and crustal CO_2 outgassing in collisional orogens. *Geochimica et Cosmochimica Acta* 300: 192–214.
Eiler JM, Baumgartner LP, and Valley JW (1992) Intercrystalline stable isotope diffusion: A fast grain boundary model. *Contributions to Mineralogy and Petrology* 112: 543–557.
Elmer FL, Powell R, White RW, and Phillips GN (2007) Timing of gold mineralization relative to the peak of metamorphism at Bronzewing, Western Australia. *Economic Geology* 102: 379–392.
Elmer FL, Dugdale AL, and Wilson CJL (2008) Application of mineral equilibria modeling to constrain *T* and *X*CO_2 conditions during the evolution of the Magdala gold deposit, Stawell, Victoria, Australia. *Mineralium Deposita* 43: 759–776.
Enami M, Nishiyama T, and Mouri T (2007) Laser Raman microspectrometry of metamorphic quartz: A simple method for comparison of metamorphic pressures. *American Mineralogist* 92: 1303–1315.
Engi M (2017) Petrochronology based on REE-minerals: Monazite, allanite, xenotime, apatite. In: Kohn MJ, Engi M, and Lanari P (eds.) *Petrochronology: Methods and Applications. Reviews in Mineralogy and Geochemistry*, vol. 83, pp. 365–418. Washington, DC: Mineralogical Society of America.
Engi M, Lanari P, and Kohn MJ (2017) Significant ages. An introduction to petrochronology. In: Kohn MJ, Engi M, and Lanari P (eds.) *Petrochronology: Methods and Applications. Reviews in Mineralogy and Geochemistry*, vol. 83, pp. 1–12. Washington, DC: Mineralogical Society of America.
Eskola P (1915) On the relations between the chemical and mineralogical composition in the metamorphic rocks of the Orijarvi region. *Bulletin de la Commission géologique de Finlande* 44: 109–143.
Essene EJ (1982) Geologic thermometry and barometry. In: Ferry JM (ed.) *Characterization of Metamorphism Through Mineral Equilibria. Mineralogical Society of America*, vol. 10, pp. 153–206. Washington, DC.

Evans TP (2004) A method for calculating effective bulk composition modification due to crystal fractionation in garnet-bearing schist; implications for isopleth thermobarometry. *Journal of Metamorphic Geology* 22: 547–557.
Evans KA and Powell R (2015) The effect of subduction on the sulphur, carbon and redox budget of lithospheric mantle. *Journal of Metamorphic Geology* 33: 649–670.
Evans KA and Tomkins AG (2020) Metamorphic fluids in orogenic settings. *Elements* 16: 381–388.
Evans KA, Powell R, and Holland TJB (2010) Internally consistent data for sulphur-bearing phases and application to the construction of pseudosections for mafic greenschist facies rocks in Na_2O–CaO–K_2O–FeO–MgO–Al_2O_3–SiO_2–CO_2–O–S–H_2O. *Journal of Metamorphic Geology* 28: 667–687.
Evans KA, Powell R, and Frost BR (2013) Using equilibrium thermodynamics in the study of metasomatic alteration, illustrated by an application to serpentinites. *Lithos* 168–169: 67–84.
Ferrando S, Groppo C, Frezzotti ML, Castelli D, and Proyer A (2017) Dissolving dolomite in a stable UHP mineral assemblage: Evidence from Cal-Dol marbles of the Dora-Maira Massif (Italian Western Alps). *American Mineralogist* 102: 42–60.
Ferry JM (1976) Metamorphism of calcareous sediments in the Waterville–Vassalboro area, south–central Maine: Mineral reactions and graphical analysis. *American Journal of Science* 276: 841–882.
Ferry JM (1986) Reaction progress: A monitor of fluid-rock interaction during metamorphic and hydrothermal events. In: Walther JV and Wood BJ (eds.) *Fluid-Rock Interactions During Metamorphism*, pp. 60–88. New York: Springer Verlag.
Ferry JM (1992) Regional metamorphism of the Waits River Formation, eastern Vermont: Delineation of a new type of giant metamorphic hydrothermal system. *Journal of Petrology* 33: 45–94.
Ferry JM and Spear FS (1978) Experimental calibration of the partitioning of Fe and Mg between biotite and garnet. *Contributions to Mineralogy and Petrology* 66: 113–117.
Ferry J and Watson E (2007) New thermodynamic models and revised calibrations for the Ti-in-zircon and Zr-in-rutile thermometers. *Contributions to Mineralogy and Petrology* 154: 429–437.
Ferry JM, Winslow NW, and Penniston-Dorland SC (2013) Re-evaluation of infiltration-driven regional metamorphism in northern New England: New transport models with solid solution and cross-layer equilibration of fluid composition. *Journal of Petrology* 54: 2455–2485.
Fitzsimons ICW and Harley SL (1994) The influence of retrograde cation exchange on granulite P-T estimates and a convergence technique for the recovery of peak metamorphic conditions. *Journal of Petrology* 35: 543–576.
Foster CT (1986) Thermodynamic models of reactions involving garnet in a sillimanite/staurolite schist. *Mineralogical Magazine* 50: 427–439.
Foster CT (1999) Forward modeling of metamorphic textures. *The Canadian Mineralogist* 37: 415–429.
Frezzotti ML and Ferrando S (2015) The chemical behavior of fluids released during deep subduction based on fluid inclusions. *American Mineralogist* 100: 352–377.
Fuhrman ML and Lindsley DH (1988) Ternary feldspar modeling and thermometry. *American Mineralogist* 73: 201–215.
Gaidies F, Abart R, de Capitani C, Schuster R, Connolly JAD, and Reusser E (2006) Characterization of polymetamorphism in the Austroalpine basement east of the Tauern Window using garnet isopleth thermobarometry. *Journal of Metamorphic Geology* 24: 451–475.
Gaidies F, de Capitani C, and Abart R (2008) THERIA_G: A software program to numerically model prograde garnet growth. *Contributions to Mineralogy and Petrology* 155: 657–667.
Gaillardet J and Galy A (2008) Himalaya-carbon sink or source? *Science* 320: 1727–1728.
Galvez ME, Manning CE, Connolly JAD, and Rumble D (2015) The solubility of rocks in metamorphic fluids: A model for rock-dominated conditions to upper mantle pressure and temperature. *Earth and Planetary Science Letters* 430: 486–498.
Giletti BJ (1986) Diffusion effects on oxygen isotope temperature of slowly cooled igneous and metamorphic rocks. *Earth and Planetary Science Letters* 77: 218–228.
Gilio M, Angel RJ, and Alvaro M (2021) Elastic geobarometry: How to work with residual inclusion strains and pressures. *American Mineralogist* 106: 1530–1533.
Gonzalez JP, Thomas JB, Baldwin SL, and Alvaro M (2019) Quartz-in-garnet and Ti-in-quartz thermobarometry: Methodology and first application to a quartzofeldspathic gneiss from eastern Papua New Guinea. *Journal of Metamorphic Geology* 37: 1193–1208.
Gonzalez JP, Mazzucchelli ML, Angel RJ, and Alvaro M (2021) Elastic geobarometry for anisotropic inclusions in anisotropic host minerals: Quartz-in-zircon. *Journal of Geophysical Research - Solid Earth* 126. e2021JB022080.
Goscombe B, Gray D, and Foster DA (2018) Metamorphic response to collision in the Central Himalayan Orogen. *Gondwana Research* 57: 191–265.
Green ECR, White RW, Diener JFA, Powell R, Holland TJB, and Palin RM (2016) Activity–composition relations for the calculation of partial melting equilibria in metabasic rocks. *Journal of Metamorphic Geology* 34: 845–869.
Greenwood HJ (1962) Metamorphic reactions involving two volatile components. *Year Book*, vol. 61, pp. 82–85. Carnegie Institution of Washington.
Greenwood HJ (1975) Buffering of pore fluids by metamorphic reactions. *American Journal of Science* 275: 573–593.
Groppo C and Castelli D (2010) Prograde P-T evolution of a lawsonite eclogite from the Monviso meta-ophiolite (Western Alps): Dehydration and redox reactions during subduction of oceanic FeTi-oxide gabbro. *Journal of Petrology* 51: 2489–2514.
Groppo C, Rolfo F, and Castelli D (2007) Pre-Alpine HT mineral relics in impure marbles from the UHP Brossasco–Isasca Unit (Dora–Maira Massif, western Alps). *Periodico di Mineralogia* 76: 155–168.
Groppo C, Rolfo F, and Lombardo B (2009) P–T evolution across the Main Central Thrust Zone (Eastern Nepal): Hidden discontinuities revealed by petrology. *Journal of Petrology* 50: 1149–1180.
Groppo C, Rolfo F, and Indares A (2012) Partial melting in the Higher Himalayan Crystallines of Eastern Nepal: The effect of decompression and implications for the 'Channel Flow' model. *Journal of Petrology* 53: 1057–1088.
Groppo C, Rolfo F, Castelli D, and Connolly JAD (2013a) Metamorphic CO_2 production from calc-silicate rocks via garnet-forming reactions in the CFAS–H_2O–CO_2 system. *Contributions to Mineralogy and Petrology* 166: 1655–1675.
Groppo C, Rolfo F, and Mosca P (2013b) The cordierite-bearing anatectic rocks of the Higher Himalayan Crystallines (eastern Nepal): Low-pressure anatexis, melt-productivity, melt loss and the preservation of cordierite. *Journal of Metamorphic Geology* 31: 187–204.
Groppo C, Rolfo F, Liu YC, Deng LP, and Wang AD (2015) P-T evolution of elusive UHP eclogites from the Luotian dome (north Dabie zone, China): How far can the thermodynamic modeling lead us? *Lithos* 226: 183–200.
Groppo C, Rolfo F, Sachan HK, and Rai SK (2016) Petrology of blueschist from the western Himalaya (Ladakh, NW India): Exploring the complex behaviour of a lawsonite-bearing system in a palaeo-accretionary setting. *Lithos* 252–253: 41–56.
Groppo C, Rolfo F, Castelli D, and Mosca P (2017) Metamorphic CO_2 production in collisional orogens: Petrologic constraints from phase diagram modeling of Himalayan, scapolite-bearing, calc-silicate rocks in the NKC(F)MAS(T)-HC system. *Journal of Petrology* 58: 53–84.
Groppo C, Ferrando S, Gilio M, Botta S, Nosenzo F, Balestro G, Festa A, and Rolfo F (2019) What's in the sandwich? New P–T constraints for the (U)HP nappe stack of southern Dora-Maira Massif (Western Alps). *European Journal of Mineralogy* 31: 665–683.
Groppo C, Rapa G, Frezzotti ML, and Rolfo F (2021) The fate of calcareous pelites in collisional orogens. *Journal of Metamorphic Geology* 39: 181–207.
Groppo C, Rolfo F, and Frezzotti ML (2022) CO_2 outgassing during collisional orogeny is facilitated by the generation of immiscible fluids. *Communications Earth & Environment* 3: 13.
Guevara VE and Caddick MJ (2016) Shooting at a moving target: Phase equilibria modelling of high-temperature metamorphism. *Journal of Metamorphic Geology* 34: 209–235.
Guiraud M, Powell R, and Rebay G (2001) H_2O in metamorphism and the preservation of metamorphic mineral assemblages. *Journal of Metamorphic Geology* 19: 445–454.
Hacker BR, Peacock SM, Abers GA, and Holloway SD (2003) Subduction factory 2. Are intermediate-depth earthquakes in subducting slabs linked to metamorphic dehydration reactions? *Journal of Geophysical Research - Solid Earth* 108. https://doi.org/10.1029/2001JB001129.
Harley SL and Buick IS (1992) Wollastonite–scapolite assemblages as indicators of granulite pressure–temperature–fluid history: The Rauer Group, East Antarctica. *Journal of Petrology* 33: 693–728.
Hayden LA, Watson EB, and Wark DA (2008) A thermobarometer for sphene (titanite). *Contributions to Mineralogy and Petrology* 155: 529–540.

Henry DJ, Guidotti CV, and Thomson JA (2005) The Ti-saturation surface for low-to-mediumpressure metapelitic biotites: Implications for geothermometry and Ti-substitution mechanisms. *American Mineralogist* 90: 316–328.
Hewitt DA (1973) The metamorphism of micaceous limestones from South–Central Connecticut. *American Journal of Science* 273A: 444–469.
Hickmott DD, Shimizu N, Spear FS, and Selverstone J (1987) Trace-element zoning in a metamorphic garnet. *Geology* 15: 573–576.
Hofmann AE, Baker MB, and Eiler JM (2013) An experimental study of Ti and Zr partitioning among zircon, rutile, and granitic melt. *Contributions to Mineralogy and Petrology* 166: 235–253.
Holland TJB and Powell R (1985) An internally consistent thermodynamic dataset with uncertainties and correlations: 2. Data and results. *Journal of Metamorphic Geology* 3: 343–370.
Holland TJB and Powell R (1988) An internally consistent thermodynamic data set for phases of petrological interest. *Journal of Metamorphic Geology* 8: 89–124.
Holland TJB and Powell R (1990) An enlarged and updated internally consistent thermodynamic dataset with uncertains and correlations: The system K_2O–Na_2O–CaO–MgO–MnO–FeO–Fe_2O_3–Al_2O_3–TiO_2–SiO_2–C–H_2–O_2. *Journal of Metamorphic Geology* 8: 89–124.
Holland TJB and Powell R (1998) An internally consistent thermodynamic data set for phases of petrological interest. *Journal of Metamorphic Geology* 16: 309–343.
Holland TJB and Powell R (2011) An improved and extended internally consistent thermodynamic dataset for phases of petrological interest, involving a new equation of state for solids. *Journal of Metamorphic Geology* 29: 333–383.
Hoschek G (2016) Phase relations of the REE minerals florencite, allanite and monazite in quartzitic garnet–kyanite schist of the Eclogite Zone, Tauern Window, Austria. *European Journal of Mineralogy* 28: 735–750.
Huang R and Audétat A (2012) The titanium-in-quartz (TitaniQ) thermobarometer: A critical examination and re-calibration. *Geochimica et Cosmochimica Acta* 84: 75–89.
Indares A, White RW, and Powell R (2008) Phase equilibria modelling of kyanite-bearing anatectic paragneisses from the central Grenville Province. *Journal of Metamorphic Geology* 26: 815–836.
Jackson JA, Austrheim H, McKenzie D, and Priestley K (2004) Metastability, mechanical strength, and the support of mountain belts. *Geology* 32: 625–628.
Jamtveit B and Austrheim H (2010) Metamorphism: The role of fluids. *Elements* 6: 153–158.
Janots E, Brunet F, Goffé B, Poinssot C, Burchard M, and Cemič L (2007) Thermochemistry of monazite-(La) and dissakisite-(La): Implications for monazite and allanite stability in metapelites. *Contributions to Mineralogy and Petrology* 154: 1–14.
Jenkin GRT, Farrow CM, Fallick AE, and Higgins D (1994) Oxygen isotope exchange and closure temperatures in cooling rocks. *Journal of Metamorphic Geology* 12: 221–235.
Johnson T, Yakymchuk C, and Brown M (2021) Crustal melting and supra-solidus phase equilibria: From first principles to the state-of-the-art. *Earth-Science Reviews* 221: 103778.
Karmakar S (2021) Formation of clinohumite ± spinel in dolomitic marbles from the Makrohar Granulite Belt, Central India: Evidence for Ti mobility during regional metamorphism. *American Mineralogist* 106: 1818–1827.
Kelsey DE and Powell R (2011) Progress in linking accessory mineral growth and breakdown to major mineral evolution in metamorphic rocks: A thermodynamic approach in the Na_2O–CaO–K_2O–FeO–MgO–Al_2O_3–SiO_2–H_2O–TiO_2–ZrO_2 system. *Journal of Metamorphic Geology* 29: 151–166.
Kendrick J and Indares A (2018) The reaction history of kyanite in high-P aluminous granulites. *Journal of Metamorphic Geology* 36: 125–146.
Kerrick DM (1974) Review of mixed-volatile (H_2O–CO_2) equilibria. *American Mineralogist* 59: 729–762.
Kerrick DM and Caldeira K (1993) Paleoatmospheric consequences of CO_2 released during early Cenozoic regional metamorphism in the Tethyan orogen. *Chemical Geology* 108: 201–230.
Kerrick DM and Connolly JAD (2001a) Metamorphic devolatilization of subducted oceanic metabasalts: Implications for seismicity, arc magmatism and volatile recycling. *Earth and Planetary Science Letters* 189: 19–29.
Kerrick DM and Connolly JAD (2001b) Metamorphic devolatilization of subducted marine sediments and the transport of volatiles into the Earth's mantle. *Nature* 411: 293–296.
Kohn MJ (2008) PTt data from central Nepal support critical taper and repudiate large scale channel flow of the Greater Himalayan Sequence. *Geological Society of America Bulletin* 120: 259–273.
Kohn MJ (2014a) Geochemical zoning in metamorphic minerals. In: Turekian K and Holland H (eds.) *Treatise on Geochemistry*, 2nd edn, vol. 4, pp. 249–280.
Kohn MJ (2014b) Himalayan metamorphism and its tectonic implications. *Annual Review of Earth and Planetary Sciences* 42: 381–419.
Kohn MJ (2014c) "Thermoba-Raman-try": Calibration of spectroscopic barometers and thermometers for mineral inclusions. *Earth and Planetary Science Letters* 388: 187–196.
Kohn MJ (2016) Metamorphic chronology—A tool for all ages: Past achievements and future prospects. *American Mineralogist* 101: 25–42.
Kohn MJ (2017) Titanite petrochronology. In: Kohn MJ, Engi M, and Lanari P (eds.) *Petrochronology: Methods and Applications. Reviews in Mineralogy and Geochemistry*, vol. 83, pp. 419–440. Washington, DC: Mineralogical Society of America.
Kohn MJ (2020) A refined zirconium-in-rutile thermometer. *American Mineralogist* 105: 963–971.
Kohn MJ and Kelly NM (2018) Petrology and geochronology of metamorphic zircon. In: Moser DE, Corfu F, Darling JR, Reddy SM, and Tait K (eds.) *Microstructural Geochronology: Planetary Records Down to Atom Scale. Geophysical Monograph Series*, pp. 35–61. American Geophysical Union.
Kohn MJ and Penniston-Dorland SC (2017) Diffusion: Obstacles and opportunities in petrochronology. In: Kohn MJ, Engi M, and Lanari P (eds.) *Petrochronology: Methods and Applications. Reviews in Mineralogy and Geochemistry*, vol. 83, pp. 103–152. Washington, DC: Mineralogical Society of America.
Kohn MJ and Spear FS (1991) Error propagation for barometers: 2. Application to rocks. *American Mineralogist* 76: 138–147.
Kohn MJ and Spear FS (2000) Retrograde net transfer reaction insurance for pressure–temperature estimates. *Geology* 28: 1127–1130.
Kohn MJ, et al. (2023) *Annual Review of Earth and Planetary Sciences*. (in press) – to be updated.
Konrad-Schmolke M, O'Brien PJ, de Capitani C, and Carswell DA (2008) Garnet growth at high- and ultra-high pressure conditions and the effect of element fractionation on mineral modes and composition. *Lithos* 103: 309–332.
Korsakov AV, Kohn MJ, and Perraki M (2020) Applications of Raman spectroscopy in metamorphic petrology and tectonics. *Elements* 16: 105–110.
Kuhn BK, Reusser E, and Powell R (2005) Metamorphic evolution of calc-schists in the Central Alps, Switzerland. *Schweizerische Mineralogische und Petrographische Mitteilungen* 85: 175–190.
Lahfid A, Beyssac O, Deville E, Negro F, Chopin C, and Goffé B (2010) Evolution of the Raman spectrum of carbonaceous material in low-grade metasediments of the Glarus Alps (Switzerland). *Terra Nova* 22: 354–360.
Lanari P and Duesterhoeft E (2019) Modeling metamorphic rocks using equilibrium thermodynamics and internally consistent databases: Past achievements, problems and perspectives. *Journal of Petrology* 60: 19–56.
Lanari P and Engi M (2017) Local bulk composition effects on mineral assemblages. In: Kohn MJ, Engi M, and Lanari P (eds.) *Petrochronology: Methods and Applications. Reviews in Mineralogy and Geochemistry*, vol. 83, pp. 55–102. Washington, DC: Mineralogical Society of America.
Lanari P and Hermann J (2021) Iterative thermodynamic modelling—Part 2: Tracing equilibrium relationships between minerals in metamorphic rocks. *Journal of Metamorphic Geology* 39: 651–674.
Lanari P, Giuntoli F, Loury C, Burn M, and Engi M (2017) An inverse modeling approach to obtain P–T conditions of metamorphic stages involving garnet growth and resorption. *European Journal of Mineralogy* 29: 181–199.
Liang Y, Sun C, and Yao L (2013) A REE-in-two-pyroxene thermometer for mafic and ultramafic rocks. *Geochimica et Cosmochimica Acta* 102: 246–260.
López Sánchez Vizcaíno V, Connolly JAD, and Gómez-Pugnaire MT (1997) Metamorphism and phase relations in carbonate rocks from the Nevado-Filá bride Complex (Cordilleras Béticas, Spain): Application of the Ttn+Rt+Cal+Qtz+Gr buffer. *Contributions to Mineralogy and Petrology* 126: 292–302.
Lopez-Carmona A, Pitra P, and Abati J (2013) Blueschist-facies metapelites from the Malpica-Tui Unit (NW Iberian Massif): Phase equilibria modelling and H_2O and Fe_2O_3 influence in high-pressure assemblages. *Journal of Metamorphic Geology* 31: 263–280.

Luque FJ, Ortega L, Barrenechea JF, Millward D, Beyssac O, and Huizenga JM (2009) Deposition of highly crystalline graphite from moderate-temperature fluids. *Geology* 37: 275–278.
Maffeis A, Ferrando S, Connolly JAD, Groppo C, Frezzotti ML, and Castelli D (2021) Thermodynamic analysis of HP-UHP fluid inclusions: The solute load and chemistry of metamorphic fluids. *Geochimica et Cosmochimica Acta* 15: 207–229.
Mahar EM, Baker JM, Powell R, Holland TJB, and Howell N (1997) The effect of Mn on mineral stability in metapelites. *Journal of Metamorphic Geology* 15: 223–238.
Manning CE (2018) Fluids of the lower crust: Deep is different. *Annual Review of Earth and Planetary Sciences* 46: 67–97.
Manning CE and Frezzotti ML (2020) Subduction-zone fluids. *Elements* 16: 395–400.
Manzotti P, Bosse V, Pitra P, Robyr M, Schiavi F, and Ballèvre M (2018) Exhumation rates in the Gran Paradiso Massif (Western Alps) constrained by in situ U-Th-Pb dating of accessory phases (monazite, allanite and xenotime). *Contributions to Mineralogy and Petrology* 173: 24.
Manzotti P, Ballèvre M, Pitra P, and Schiavi F (2021) Missing lawsonite and aragonite found: P-T and fluid composition in meta-marls from the Combin Zone (Western Alps). *Contributions to Mineralogy and Petrology* 176: 60.
Manzotti P, Schiavi F, Nosenzo F, Pitra P, and Ballèvre M (2022) A journey towards the forbidden zone: A new, cold, UHP unit in the Dora-Maira Massif (Western Alps). *Contributions to Mineralogy and Petrology* 177: 59.
Marmo BA, Clarke GL, and Powell R (2002) Fractionation of bulk rock composition due to porphyroblast growth: Effects on eclogite facies mineral equilibria, Pam Peninsula, New Caledonia. *Journal of Metamorphic Geology* 20: 151–165.
Massonne HJ and Schreyer W (1987) Phengite geobarometry based on the limiting assemblage with K-feldspar, phlogopite and quartz. *Contributions to Mineralogy and Petrology* 96: 212–224.
Massonne HJ and Schreyer W (1989) Stability field of the high pressure assemblage talc+phengite and two new phengite barometers. *European Journal of Mineralogy* 1: 391–410.
Massonne HJ and Szpurka Z (1997) Thermodynamic properties of white micas on the basis of high-pressure experiments in the systems K_2O-MgO-Al_2O_3-SiO_2-H_2O and K_2O-FeO-Al_2O_3-SiO_2-H_2O. *Lithos* 41: 229–250.
Mathavan V and Fernando GWAR (2001) Reactions and textures in grossular–wollastonite–scapolite calc-silicate granulites from Maligawila, Sri Lanka: Evidence for high temperature isobaric cooling in the meta-sediments of the Highland Complex. *Lithos* 59: 217–232.
Mazzucchelli ML, Burnley P, Angel RJ, Morganti S, Domeneghetti MC, Nestola F, and Alvaro M (2018) Elastic geothermobarometry: Corrections for the geometry of the host-inclusion system. *Geology* 46: 231–234.
Mazzucchelli ML, Reali A, Morganti S, Angel RJ, and Alvaro M (2019) Elastic geobarometry for anisotropic inclusions in cubic hosts. *Lithos* 350–351: 105218.
Miron GD, Wagner T, Kulik DA, and Heinrich CA (2016) Internally consistent thermodynamic data for aqueous species in the system Na-K-Al-Si-O-H-Cl. *Geochimica et Cosmochimica Acta* 187: 41–78.
Miron GD, Wagner T, Kulik DA, and Lothenbach B (2017) An internally consistent thermodynamic dataset for aqueous species in the system Ca-Mg-Na-K-Al-Si-O-H-C-Cl to 800°C and 5 kbar. *American Journal of Science* 317: 755–806.
Molina JF, Moreno JA, Castro A, Rodrígrez C, and Fershater GB (2015) Calcic amphibole thermobarometry in metamorphic and igneous rocks: New calibrations based on plagioclase/amphibole Al-Si partitioning and amphibole/liquid Mg partitioning. *Lithos* 232: 286–305.
Morissey LJ and Tomkins AG (2020) Evaporite-bearing orogenic belts produce ligand-rich and diverse metamorphic fluids. *Geochimica et Cosmochimica Acta* 275: 163–187.
Moulas E, Kostopoulo D, Podladchikov Y, Chatzitheodoridi E, Schenker FL, Zingerman KM, Pomonis P, and Tajčmanová L (2019) Calculating pressure with elastic geobarometry: A comparison of different elastic solutions with application to a calc-silicate gneiss from the Rhodope Metamorphic Province. *Lithos* 378–379: 105803.
Moynihan DP and Pattison DRM (2013) An automated method for the calculation of P–T paths from garnet zoning, with application to metapelitic schist from the Kootenay Arc, British Columbia, Canada. *Journal of Metamorphic Geology* 31: 525–548.
Müller A, van der Kerkhof AM, Selbekk RS, and Broekmans MATM (2016) Trace element composition and cathodoluminescence of kyanite and its petrogenetic implications. *Contributions to Mineralogy and Petrology* 171: 70.
Nabelek PI (2002) Calc-silicate reactions and bedding controlled isotopic exchange in the Notch Peak aureole, Utah: Implications for differential fluid fluxes with metamorphic grade. *Journal of Metamorphic Geology* 20: 429–440.
Nabelek PI and Chen Y (2014) The initial garnet-in reaction involving siderite–rhodochrosite, garnet re-equilibration and P-T–t paths of graphitic schists in the Black Hills orogen, South Dakota, USA. *Journal of Metamorphic Geology* 32: 133–150.
Nagurney AB, Caddick MJ, Dragovic B, and Busse K (2021) The (chemical) potential for understanding overstepped garnet nucleation and growth. *American Mineralogist* 106: 812–829.
Nerone S, Groppo C, and Rolfo F (2023) Equilibrium and kinetic approaches to understand the occurrence of the uncommon chloritoid+biotite assemblage. *European Journal of Mineralogy* 35: 305–320.
Omori S, Liou JG, Zhang RY, and Ogasawara Y (1998) Petrogenesis of impure dolomitic marble from the Dabie Mountains, central China. *Island Arc* 7: 98–114.
Osborne ZB, Thomas JB, Nachlas WO, and Angel RJ (2022) TitaniQ revisited: Expanded and improved Ti-in-quartz solubility model for thermobarometry. *Contributions to Mineralogy and Petrology* 177: 31.
Palin RM, Weller OM, Waters DJ, and Dyck B (2016) Quantifying geological uncertainty in metamorphic phase equilibria modelling; a Monte Carlo assessment and implications for tectonic interpretations. *Geoscience Frontiers* 7: 591–607.
Pattison DRM and DeBuhr CL (2015) Petrology of metapelites in the Bugaboo aureole, British Columbia, Canada. *Journal of Metamorphic Geology* 33: 437–462.
Pattison DRM and Spear FS (2018) Kinetic control of staurolite–Al_2SiO_5 mineral assemblages: Implications for Barrovian and Buchan metamorphism. *Journal of Metamorphic Geology* 36: 667–690.
Pattison DRM and Tinkham DK (2009) Interplay between equilibrium and kinetics in prograde metamorphism of pelites: An example from the Nelson aureole, British Columbia. *Journal of Metamorphic Geology* 27: 249–279.
Pattison DRM, Chacko T, Farquhar J, and McFarlane CRM (2003) Temperatures of granulite-facies metamorphism: Constraints from experimental phase equilibria and thermobarometry corrected for retrograde exchange. *Journal of Petrology* 44: 867–900.
Pattison DRM, de Capitani C, and Gaidies F (2011) Petrological consequences of variations in metamorphic reaction affinity. *Journal of Metamorphic Geology* 29: 953–977.
Penniston-Dorland SC (2023) Review on Fluids. To be completed.
Penniston-Dorland SC, Kohn MJ, and Piccoli PM (2018) A mélange of subduction temperatures: Evidence from Zr-in-rutile thermometry for strengthening of the subduction interface. *Earth and Planetary Science Letters* 482: 525–535.
Perraki M, Proyer A, Mposkos E, Kaindl R, and Hoinkes G (2006) Raman microspectroscopy on diamond, graphite and other carbon polymorphs from the ultrahigh-pressure metamorphic Kimi Complex of the Rhodope Metamorphic Province, NE Greece. *Earth and Planetary Science Letters* 241: 672–685.
Phillips GN and Powell R (2010) Formation of gold deposits: A metamorphic devolatilization model. *Journal of Metamorphic Geology* 28: 689–718.
Powell R (1978) *Equilibrium Thermodynamics in Petrology*. London: Harper & Row.
Powell R and Holland TJB (1988) An internally consistent dataset with uncertainties and correlations: 3. Applications to geobarometry, worked examples and a computer program. *Journal of Metamorphic Geology* 6: 173–204.
Powell R and Holland TJB (1994) Optimal geothermometry and geobarometry. *American Mineralogist* 79: 120–133.
Powell R and Holland TJB (2008) On thermobarometry. *Journal of Metamorphic Geology* 26: 155–179.
Powell R and Holland T (2010) Using equilibrium thermodynamics to understand metamorphism and metamorphic rocks. *Elements* 6: 309–314.
Powell R, Holland T, and Worley B (1998) Calculating phase diagrams involving solid solutions via non-linear equations, with examples using THERMOCALC. *Journal of Metamorphic Geology* 16: 577–588.

Powell R, Guiraud M, and White RW (2005) Truth and beauty in metamorphic phase-equilibria: Conjugate variables and phase diagrams. *The Canadian Mineralogist* 43: 21–33.
Pyle JM and Spear FS (2000) An empirical garnet (YAG)-xenotime thermometer. *Contributions to Mineralogy and Petrology* 138: 51–58.
Pyle JM, Spear FS, Rudnick RL, and McDonough WF (2001) Monazite xenotime-garnet equilibrium in metapelites and a new monazite-garnet thermometer. *Journal of Petrology* 42: 2083–2107.
Qi Y, Kohn MJ, Huang G, Zheng Y, Jiao S, and Guo J (2022) Thermal regime of the lower crust in the eastern Khondalite Belt, North China Craton, constrained by Zr-in-rutile thermometry mapping. *Precambrian Research* 377: 106720.
Rapa G, Groppo C, Rolfo F, Petrelli M, Mosca P, and Perugini D (2017) Titanite-bearing calc-silicate rocks constrain timing, duration, and magnitude of metamorphic CO_2 degassing in the Himalayan belt. *Lithos* 292–293: 364–378.
Riel N, Kaus BJP, Green ECR, and Berlie N (2022) MAGEMin, an efficient Gibbs energy minimizer: Application to igneous systems. *Geochemistry, Geophysics, Geosystems* 23. e2022GC010427.
Robinson P (1991) Eye of the petrographer, mind of the petrologist. *American Mineralogist* 76: 1781–1810.
Rosenfeld JL and Chase AB (1961) Pressure and temperature of crystallization from elastic effects around solid inclusions in minerals? *American Journal of Science* 259: 519–541.
Rubatto D (2017) Zircon: The metamorphic mineral. In: Kohn MJ, Engi M, and Lanari P (eds.) *Petrochronology: Methods and Applications. Reviews in Mineralogy and Geochemistry*, vol. 83, pp. 261–295. Washington, DC: Mineralogical Society of America.
Rüpke LH, Phipps Morgan J, Hort M, and Connolly JAD (2004) Serpentine and the subduction zone water cycle. *Earth and Planetary Science Letters* 223: 17–34.
Schmädicke E, Okrusch M, Schubert W, Elwart B, and Görke U (2001) Phase relations of calc-silicate assemblages in the Auerbach marble, Odenwald Crystalline Complex, Germany. *Mineralogy and Petrology* 72: 77–111.
Selverstone J and Gutzler DS (1993) Post-125 Ma carbon storage associated with continent–continent collision. *Geology* 21: 885–888.
Sengupta P and Raith MM (2002) Garnet stoichiometry as petrogenetic indicator: An example from the marble–calcsilicate interface from Kondapalle, Eastern Ghats Belt. *American Journal of Science* 302: 686–725.
Sengupta P, Sanyal S, Dasgupta S, Fukuoka M, and Ehl J (1997) Controls of mineral reactions in high-grade garnet–wollastonite–scapolite-bearing calcsilicate rocks: An example from Anakapalle, Eastern Ghats, India. *Journal of Metamorphic Geology* 15: 551–564.
Shrestha S, Larson KP, Duesterhoeft E, Soret M, and Cottle JM (2019) Thermodynamic modelling of phosphate minerals and its implications for the development of P-T-t histories: A case study in garnet—Monazite bearing metapelites. *Lithos* 334–335: 141–160.
Skippen GB (1971) Experimental data for reactions in siliceous marbles. *Journal of Geology* 79: 457–481.
Skippen GB (1974) An experimental model for low pressure metamorphism of siliceous dolomitic marble. *American Journal of Science* 274: 487–509.
Smye AJ, Greenwood LV, and Holland TJB (2010) Garnet–chloritoid–kyanite assemblages: Eclogite facies indicators of subduction constraints in orogenic belts. *Journal of Metamorphic Geology* 28: 753–768.
Spear FS (1988) The Gibbs method and Duhem's theorem: The quantitative relationships among P, T, chemical potential, phase composition and reaction progress in igneous and metamorphic systems. *Contributions to Mineralogy and Petrology* 99: 249–256.
Spear FS (1989) Relative thermobarometry and metamorphic P–T paths. In: Daly JS, Cliff RA, and Yardley BWD (eds.) *Evolution of Metamorphic Belts*, pp. 63–81. London: Geological Society. Special Publications 43.
Spear FS (1991) On the interpretation of peak metamorphic temperatures in light of garnet diffusion during cooling. *Journal of Metamorphic Geology* 9: 379–388.
Spear FS (1993) *Metamorphic Phase Equilibria and Pressure-Temperature-Time Paths*. Washington, DC: Mineralogical Society of America.
Spear FS (2010) Monazite–allanite phase relations in metapelites. *Chemical Geology* 279: 55–62.
Spear FS and Cheney JT (1989) A petrogenetic grid for pelitic schists in the system SiO_2-Al_2O_3-FeO-MgO-K_2O-H_2O. *Contributions to Mineralogy and Petrology* 101: 149–164.
Spear FS and Florence FP (1992) Thermobarometry in granulites: Pitfalls and new approaches. *Precambrian Research* 55: 209–241.
Spear FS and Menard T (1989) Program GIBBS: A generalized Gibbs method algorithm. *American Mineralogist* 74: 942–943.
Spear FS and Pattison DRM (2017) The implications of overstepping for metamorphic assemblage diagrams (MADs). *Chemical Geology* 457: 38–46.
Spear FS and Pyle JM (2010) Theoretical modeling of monazite growth in a low-Ca metapelite. *Chemical Geology* 273: 111–119.
Spear FS and Wolfe OM (2018) Evaluation of the effective bulk composition (EBC) during growth of garnet. *Chemical Geology* 491: 39–47.
Spear FS and Wolfe OM (2019) Implications of overstepping of garnet nucleation for geothermometry, geobarometry and P-T path calculations. *Chemical Geology* 530: 119323.
Spear FS, Ferry JM, and Rumble D III (1982) Analytical formulation of phase equilibria: The Gibbs' method. *Reviews in Mineralogy* 10: 105–152.
Spear FS, Selverstone J, Hickmott D, Crowley P, and Hodges KV (1984) P-T paths from garnet zoning: A new technique for deciphering tectonic processes in crystalline terranes. *Geology* 12: 87–90.
Spear FS, Kohn MJ, Florence FP, and Menard T (1990) A model for garnet and plagioclase growth in politic schists: Implications for thermobarometry and P–T path determinations. *Journal of Metamorphic Geology* 8: 683–696.
Spear FS, Thomas JB, and Hallett BW (2014) Overstepping the garnet isograd: A comparison of QuiG barometry and thermodynamic modeling. *Contributions to Mineralogy and Petrology* 168: 1059.
Spear FS, Pattison DRM, and Cheney JT (2016) The metamorphosis of metamorphic petrology. In: Bickford ME (ed.) *The Web of Geological Sciences: Advances, Impacts, and Interactions II. Geological Society of America Special Papers 523*, pp. 31–74.
Stephenson NCN and Cook NDJ (1997) Metamorphic evolution of calcsilicate granulites near Battye Glacier, northern Prince Charles Mountains, East Antarctica. *Journal of Metamorphic Geology* 15: 361–378.
Stüwe K (1997) Effective bulk composition changes due to cooling: A model predicting complexities in retrograde reaction textures. *Contributions to Mineralogy and Petrology* 129: 43–52.
Sudholz Z, Green DH, Yaxley GM, and Jacques AL (2022) Mantle geothermometry: Experimental evaluation and recalibration of Fe–Mg geothermometers for garnet-clinopyroxene and garnet-orthopyroxene in peridotite, pyroxenite and eclogite systems. *Contributions to Mineralogy and Petrology* 177: 77.
Svensen H and Jamtveit B (2010) Metamorphic fluids and global environmental changes. *Elements* 6: 179–182.
Svensen H, Planke S, Malthe-Sørenssen A, Jamtveit B, Myklebust R, Rasmussen Eidem T, and Rey S (2004) Release of methane from a volcanic basin as a mechanism for initial Eocene global warming. *Nature* 429: 542–545.
Tamang S, Groppo C, Girault F, and Rolfo F (2023) Implications of garnet nucleation overstepping for the P-T evolution of the Lesser Himalayan Sequence of central Nepal. *Journal of Metamorphic Geology* 41: 271–297.
Thomas J, Watson EB, and Spear F (2010) TitaniQ under pressure: The effect of pressure and temperature on the solubility of Ti in quartz. *Contributions to Mineralogy and Petrology* 160: 743–759.
Thompson AB (1983) Fluid-absent metamorphism. *Journal of the Geological Society of London* 140: 533–547.
Thompson AB (1984) Mineral reactions and mineral equilibria and their use in geothermometry, geobarometry and geohygrometry. In: Lagache M (ed.) *Thermométrie et Barométrie Géologiques*, pp. 179–199. Paris: Société Francaise de Minéralogie et de Cristallographie.
Thompson JB Jr (1959) Local equilibrium in metasomatic processes. In: Eugster HP (ed.) *Researches in Geochemistry*, pp. 427–457. New York: John Wiley and Sons.
Tinkham DK and Ghent ED (2005) Estimating P–T conditions of garnet growth with isochemical phase-diagram sections and the problem of effective bulk-composition. *The Canadian Mineralogist* 43: 35–50.
Tinkham DK, Zuluaga CA, and Stowell HH (2001) Metapelite phase equilibria modeling in MnNCKFMASH: The effect of variable Al_2O_3 and MgO/(MgO + FeO) on mineral stability. *Geological Materials Research* 3: 1–42.
Tomkins AG (2010) Windows of metamorphic sulfur liberation in the crust: Implications for gold deposit genesis. *Geochimica et Cosmochimica Acta* 74: 3246–3259.

Tomkins AG, Pattison DRM, and Frost BR (2007) On the initiation of metamorphic sulfide anatexis. *Journal of Petrology* 48: 511–535.
Tracy RJ (1982) Compositional zoning and inclusions in metamorphic minerals. *Reviews in Mineralogy and Geochemistry* 10: 355–397.
Tursi F (2022) The key role of μH_2O gradients in deciphering microstructures and mineral assemblages of mylonites: Examples from the Calabria polymetamorphic terrane. *Mineralogy and Petrology* 116: 1–14.
Tursi F, Acquafredda P, Festa V, Fornelli AM, Langone A, Micheletti F, and Spiess R (2021) What can high-P sheared orthogneisses tell us? An example from the Curinga-Girifalco Line (Calabria, southern Italy). *Journal of Metamorphic Geology* 39: 919–944.
Ulmer P (2001) Partial melting in the mantle wedge: The role of H_2O in the genesis of mantle-derived 'arc-related' magmas. *Physics of the Earth and Planetary Interiors* 127: 215–232.
Valley JW (1986) Stable isotope geochemistry of metamorphic rocks. In: Valley JW, Taylor JP, and O'Neil JR (eds.) *Stable Isotopes in High Temperature Geological Processes. Reviews in Mineralogy*, vol. 16, pp. 445–490. Washington, DC: Mineralogical Society of America.
Valley JW (2001) Stable isotope thermometry at high temperatures. In: Valley JW and Cole DR (eds.) *Stable Isotope Geochemistry. Reviews in Mineralogy and Geochemistry*, vol. 43, pp. 365–414. Washington, DC: Mineralogical Society of America.
Vernon RH and Clarke GL (2008) *Principles of Metamorphic Petrology*. Cambridge: Cambridge University Press.
Vho A, Lanari P, and Rubatto D (2019) An internally-consistent database for oxygen isotope fractionation between minerals. *Journal of Petrology* 60: 2101–2130.
Vho A, Lanari P, Rubatto D, and Hermann J (2020) Tracing fluid transfers in subduction zones: An integrated thermodynamic and $\delta^{18}O$ fractionation modelling approach. *Solid Earth* 11: 307–328.
Vrijmoed JC and Hacker BR (2014) Determining P–T paths from garnet zoning using a brute-force computational method. *Contributions to Mineralogy and Petrology* 167: 1–13.
Wark DA and Watson EB (2006) TitaniQ: A titanium-in-quartz geothermometer. *Contributions to Mineralogy and Petrology* 152: 743–754.
Warr LN (2021) IMA–CNMNC approved mineral symbols. *Mineralogical Magazine* 85: 291–320.
Waters DJ (2019) Metamorphic constraints on the tectonic evolution of the High Himalaya in Nepal: The art of the possible. In: Treloar PJ and Searle MP (eds.) *Himalayan Tectonics: A Modern Synthesis*, pp. 325–375. Geological Society of London. Special Publication 483.
Waters DJ and Lovegrove DP (2002) Assessing the extent of disequilibrium and overstepping of prograde metamorphic reactions in metapelites from the Bushveld Complex aureole, South Africa. *Journal of Metamorphic Geology* 20: 135–149.
Watson EB, Wark DA, and Thomas JB (2006) Crystallization thermometers for zircon and rutile. *Contributions to Mineralogy and Petrology* 151: 413–433.
White RW and Powell R (2002) Melt loss and the preservation of granulite facies mineral assemblages. *Journal of Metamorphic Geology* 20: 621–632.
White RW, Powell R, Holland TJB, and Worley BA (2000) The effect of TiO_2 and Fe_2O_3 on metapelitic assemblages at greenschist and amphibolite facies conditions: Mineral equilibria calculations in the system K_2O-FeO-MgO-Al_2O_3-SiO_2-H_2O-TiO_2-Fe_2O_3. *Journal of Metamorphic Geology* 18: 497–512.
White RW, Powell R, and Halpin JA (2004) Spatially-focussed melt formation in aluminous metapelites from Broken Hill, Australia. *Journal of Metamorphic Geology* 22: 825–845.
White RW, Powell R, and Holland TJB (2007) Progress relating to calculation of partial melting equilibria for metapelites. *Journal of Metamorphic Geology* 25: 511–527.
White RW, Powell R, Holland TJB, Johnson TE, and Green ECR (2014a) New mineral activity–composition relations for thermodynamic calculations in metapelitic systems. *Journal of Metamorphic Geology* 32: 261–286.
White RW, Powell R, and Johnson TE (2014b) The effect of Mn on mineral stability in metapelites revisited: New *a*–X relations for manganese-bearing minerals. *Journal of Metamorphic Geology* 32: 809–828.
Will TM (1998) Phase Equilibria in Metamorphic Rocks. *Thermodynamic Background and Petrological Applications*. Berlin: Springer-Verlag.
Winter JD (2010) *Principles of Igneous and Metamorphic Petrology*, 2nd edn. Prentice Hall.
Wolfe OM and Spear FS (2018) Determining the amount of overstepping required to nucleate garnet during Barrovian regional metamorphism, Connecticut Valley Synclinorium. *Journal of Metamorphic Geology* 36: 79–94.
Wood BJ and Fraser DG (1976) *Elementary Thermodynamics for Geologists*. Oxford: Oxford University Press.
Worley B and Powell R (1998) Singularities in NCKFMASH (Na_2O-CaO-K_2O-FeO-MgO-Al_2O_3-SiO_2-H_2O). *Journal of Metamorphic Geology* 16: 169–188.
Worley B and Powell R (2000) High-precision relative thermobarometry: Theory and a worked example. *Journal of Metamorphic Geology* 18: 91–101.
Wu C-M (2015) Revised empirical garnet–biotite–muscovite–plagioclase geobarometer in metapelites. *Journal of Metamorphic Geology* 33: 167–176.
Wu C-M (2017) Calibration of the garnet–biotite–Al_2SiO_5–Quartz geobarometer for metapelites. *Journal of Metamorphic Geology* 35: 983–998.
Wu C-M and Chen H-X (2015) Revised Ti-in-biotite geothermometer for ilmenite or rutile-bearing crustal metapelites. *Scientific Bulletin* 60: 116–121.
Xiang H and Connolly JAD (2021) GeoPS: An interactive visual computing tool for thermodynamic modelling of phase equilibria. *Journal of Metamorphic Geology* 40: 243–255.
Yakymchuk C (2017) Applying phase equilibria modelling to metamorphic and geological processes: Recent developments and future potential. *Geoscience Canada* 44: 27–45.
Yakymchuk C and Brown M (2014) Behaviour of zircon and monazite during crustal melting. *Journal of the Geological Society* 171: 465–479.
Yakymchuk C, Clark C, and White RW (2017) Phase relations, reaction sequences and petrochronology. In: Kohn MJ, Engi M, and Lanari P (eds.) *Petrochronology: Methods and Applications. Reviews in Mineralogy and Geochemistry*, vol. 83, pp. 13–54. Washington, DC: Mineralogical Society of America.
Yakymchuk C, Kirkland CL, and Clark C (2018) Th/U ratios in metamorphic zircon. *Journal of Metamorphic Geology* 36: 715–737.
Yardley BWD (1989) *An Introduction to Metamorphic Petrology*, p. 248. Edinburgh: Longman.
Yardley BWD (2009) The role of water in the evolution of the continental crust. *Journal of the Geological Society of London* 166: 585–600.
Yardley BWD and Bodnar RJ (2014) Fluids in the continental crust. *Geochemical Perspectives* 3: 1–127.
Zack T and Kooijman E (2017) Petrology and geochronology of rutile. In: Kohn MJ, Engi M, and Lanari P (eds.) *Petrochronology: Methods and Applications. Reviews in Mineralogy and Geochemistry*, vol. 83, pp. 443–467. Washington, DC: Mineralogical Society of America.
Zack T, Moraes R, and Kronz A (2004) Temperature dependence of Zr in rutile: Empirical calibration of a rutile thermometer. *Contributions to Mineralogy and Petrology* 148: 471–488.
Zhan Z (2020) Mechanisms and implications of deep earthquakes. *Annual Review of Earth and Planetary Sciences* 48: 147–174.
Zhong X, Moulas E, and Tajčmanová L (2020) Post-entrapment modification of residual inclusion pressure and its implications for Raman elastic thermobarometry. *Solid Earth* 11: 223–240.
Zuluaga CA, Stowell HH, and Tinkham DK (2005) The effect of zoned garnet on metapelite pseudosection topology and calculated metamorphic P–T paths. *American Mineralogist* 90: 1619–1628.